Large scale numerical wave propagation in a randomly-fluctuating continuum model of ballasted railway tracks

Lúcio de Abreu Corrêa

université PARIS-SACLAY

CentraleSupélec

NNT : 2019SACLC018

Large scale numerical wave propagation in a randomly-fluctuating continuum model of ballasted railway tracks

Thèse de doctorat de l'Université Paris-Saclay
préparée à CentraleSupélec

École doctorale n°579 : sciences mécaniques et énergétiques, matériaux et géosciences (SMEMAG)
Spécialité de doctorat: mécanique des solides

Thèse présentée et soutenue à Gif-sur-Yvette, le 28/02/2018, par

Lúcio de Abreu Corrêa

Composition du Jury :

Etienne Balmès Professeur, Arts & Métiers ParisTech	Rapporteur
Didier Clouteau Professeur, CentraleSupélec	Examinateur
Régis Cottereau Chargé de Recherche, CNRS, CentraleSupélec	Directeur de thèse
Geert Degrande Professeur, KU Leuven (Belgium)	Rapporteur
Baldrik Faure Ingénieur, SNCF Innovation & Recherche	Invité
Karam Sab Professeur, École des Ponts ParisTech	Président

Thèse de doctorat

université PARIS-SACLAY
ÉCOLE DOCTORALE
Sciences mécaniques et énergétiques, matériaux et géosciences (SMEMAG)

Titre : Simulation numérique à large échelle de la propagation d'onde dans un modèle de continuum à fluctuations aléatoires de voies ferrées ballastées

Mots clés : Voie ferrée ballastée, méthode des éléments spectraux, modèle stochastique, propagation des ondes, milieux granulaires.

Résumé : Une forte concurrence avec d'autres moyens de transport a poussé l'industrie ferroviaire à se réinventer et rechercher des performances toujours plus élevées. De nos jours, l'obtention de vitesses chaque fois plus élevées exige le développement de modèles numériques précis pour concevoir et prédire le comportement des voies ferrées sous les contraintes mécaniques imposées par le passage du convoi. Dans cette thèse, nous avons concentré l'étude sur la couche de ballast. Ce composant présente un comportement mécanique complexe, lié à la nature granulaire de ses composants, il peut être solide, liquide ou gazeux. Ce comportement dépend de l'état de contrainte et de l'historique de déformation du milieu.

Deux classes de modèles numériques sont couramment utilisées pour prédire le comportement de ces systèmes : (1) les approches discrètes et (2) les approches continues. Pour ces premières, chaque grain du ballast est représenté par un corps rigide et interagit avec ses voisins par le biais de forces de contact non linéaires en utilisant, par exemple, la méthode de dynamique non régulière des contacts. En raison des limites de calcul, ce type de méthode ne peut résoudre que quelques mètres de longueur de ballast. Le couplage avec le sol sous la couche de ballast et avec les traverses reste également un problème non résolu dans la littérature. Pour les approches continues, le ballast est remplacé par un milieu continu homogénéisé, de façon à permettre l'utilisation de la méthode par éléments finis classique (EF). Cependant, ces modèles sont normalement utilisés avec des paramètres mécaniques homogènes, de sorte qu'ils ne représentent pas complètement l'hétérogénéité des déformations et des contraintes dans la couche de ballast.

Nous étudions dans cette thèse une approche alternative, utilisant un modèle de continuum hétérogène stochastique, qui peut être résolu avec une méthode par éléments finis tout en conservant dans une large mesure l'hétérogénéité des champs de contrainte et de déformation. L'objectif de ce modèle continu est de représenter statistiquement l'hétérogénéité du champ de contraintes dans un modèle de milieu continu ainsi que dans un modèle granulaire discret. Pour ce faire, les propriétés mécaniques sont représentées à l'aide de champs aléatoires. La présente thèse est divisée en trois parties: (1) la construction du modèle et l'identification des paramètres du matériau continuum (densité marginale de premier ordre, moyenne, variance, modèle de corrélation) ; (2) la propagation des ondes dans une voie ferrée ballastée et (3) l'exploration préliminaire de deux ensembles de données expérimentales. La première partie définit le modèle du continuum à fluctuations aléatoires et identifie les paramètres de notre modèle de continuum sur de petits échantillons cylindriques de ballast discret. Des modèles continus équivalents aux échantillons discrets sont générés et résolus en utilisant la méthode EF, et le champ stochastique utilisé pour fournir les propriétés mécaniques. Un processus d'optimisation est utilisé pour trouver une variance normalisée pour le matériau hétérogène stochastique. La deuxième partie de ce travail se concentre sur la résolution des équations dynamiques sur un modèle à grande échelle d'une voie ferrée ballastée utilisant la méthode des éléments spectraux. L'influence de l'hétérogénéité est mise en évidence et étudiée. En conséquence, des courbes de dispersion sont obtenues. Enfin, la troisième partie présente deux jeux de données distincts de mesures expérimentales sur le matériau de ballast : (1) une boîte de ballast ; (2) un passage de train dans un segment de voie ferrée ballastée. Les courbes de mobilité ont été extraites de l'expérience sur les ballasts. Un problème inverse a été résolu afin d'estimer la vitesse de l'onde homogénéisée et la vitesse de l'onde locale dans le milieu. Les passages de trains enregistrés pour l'analyse de la vibration à moyenne fréquences.

Université Paris-Saclay
Espace Technologique / Immeuble Discovery
Route de l'Orme aux Merisiers RD 128 / 91190 Saint-Aubin, France

université PARIS-SACLAY
ÉCOLE DOCTORALE
Sciences mécaniques et énergétiques, matériaux et géosciences (SMEMAG)

Title: Large scale numerical wave propagation in a randomly-fluctuating continuum model of ballasted railway tracks

Keywords : Ballasted railway track, spectral element method, stochastic model, wave propagation, granular media.

Abstract : The stronger competition with other means of transportation has increased the demand for performance in the railway industry. One way to achieve higher performance is using accurate numerical models to design/predict railways tracks behaviour.

Two classes of numerical models are commonly used to predict the behaviour of these systems: (i) discrete approaches and (ii) continuum approaches. In the former, each grain of the ballast is represented by a rigid body and interacts with its neighbours through nonlinear contact forces using, for example, the non-smooth contact dynamics method. Due to computational limits, this kind of method can only solve a few meters-length of ballast. The coupling with the soil under the ballast layer and with the sleepers also remains an open problem. In continuum approaches, the ballast is replaced by a homogenized continuum and the classical Finite Element (FE) Method (or similar) is used. However, they are normally used with homogeneous mechanical parameters, so that they do not represent fully the heterogeneity of the strains and stresses within the ballast layer.

We investigate in this thesis an alternative approach using a stochastic heterogeneous continuum model, that can be solved with a FE-like method while retaining to a large degree the heterogeneity of the stress and strain fields. The objective of this continuous model is to represent statistically the heterogeneity of the stress field in a continuum model as well as in a discrete granular model. To do this, the mechanical properties are represented using random fields.

The present thesis is divided into three parts: (1) the construction of the model and the identification of the parameters of the continuum material (first-order marginal density, mean, variance, correlation model, and correlation length); (2) wave propagation in a ballasted railway track. (3) preliminary exploration of two experimental datasets. The first part sets the randomly-fluctuating continuum model and identifies the parameters of our continuum model on small cylindrical samples of discrete ballast. Continuum models equivalent to the discrete samples are generated and solved using the FE method, and the stochastic field used as mechanical properties. An optimization process is used to find a normalized variance for the stochastic heterogeneous material. The second part of this work concentrates on the solution of the dynamical equations on a large-scale model of a ballasted railway track using the Spectral Element Method. The influence of the heterogeneity is highlighted and studied. As a result, dispersion curves are obtained. Finally, the third part presents two distinct datasets of experimental measurements on ballast material: (1) a ballast box; (2) a train passage in a segment of ballasted railway track. Mobility curves were extracted from the ballast box experiment. An inverse problem was solved in order to estimate the homogenized wave velocity and local wave velocity in the medium. The trains pass-by recorded for the analysis of the vibration at medium frequencies.

Université Paris-Saclay
Espace Technologique / Immeuble Discovery
Route de l'Orme aux Merisiers RD 128 / 91190 Saint-Aubin, France

Contents

Chapter 1

Introduction

Ballasted railway tracks (Fig. 1.1) are the most common type of surface railway tracks in the world, laid on an order of magnitude of 1 million kilometers [267]. The main component of these ballasted railway tracks is the ballast, a thin layer of coarse crushed stone, efficiently transferring the loads from the passing trains to the underlying soil.

The noise and vibration impact of trains on these tracks can be important for all types of trains: heavy freight coaches, whose impact is far reaching due to its low frequency, high-speed trains (HST), that generate high amplitude excitations; and even tramways (although more rarely on ballasted layers), which stand very close to surrounding buildings. With the increasing installation of railway/tramway track infrastructures in cities and the general increase of number and velocity of HST, this noise and vibration impact is more strictly monitored by society and regulations alike. This may force the train companies to engage in improvement operations. For instance, Switzerland's national railway company (SBB) spent around 1200M€ to fix problems related to excessive vibration levels [241]. Additionally, the geometry of the track is enforced very strictly for HST, and deformed by the settlement of the ballast layer. This again may entice the railway companies to locally limit the velocity or perform costly maintenance operations for the comfort and security of the passengers.

In France, the national railway company (Société Nationale des Chemins de Fer - SNCF) started a large program of renewal and rehabilitation of its ballasted railway tracks in 2009 [12]. One of the goals of the program is a better understanding of the behaviour of the ballasted railway track. In particular, the granular nature of the ballast layer makes prediction of the dynamical behaviour of the track extremely complex and called for special treatment. The investment of research effort into such a task is justified by the cost of maintenance operations on ballasted railway tracks, estimated at 19k€/km per year on average [54]. This is the context within which this research project was born.

1.1 Components of a ballasted railway track

The components of the track can be divided into two main groups: superstructure, and substructure. The superstructure classically refers to rails, rail pads, sleepers and rail fastening system, while the substructure is composed of the geotechnical components (ballast, sub-ballast and subgrade). Fig. 1.1 presents a schematic view of a classical ballasted railway track. The information in this section was assembled from [223, 80, 125, 116].

1.1.1 General description of the track

The rails are the elements that guide and support the train wheels. They transfer the concentrated wheel loads from the train to the supporting sleepers. The concentrated loads produce a high stress level inside the rails. This process may lead to the fatigue failure of the component [179].

(a) French high-speed train in a ballasted railway track [248]

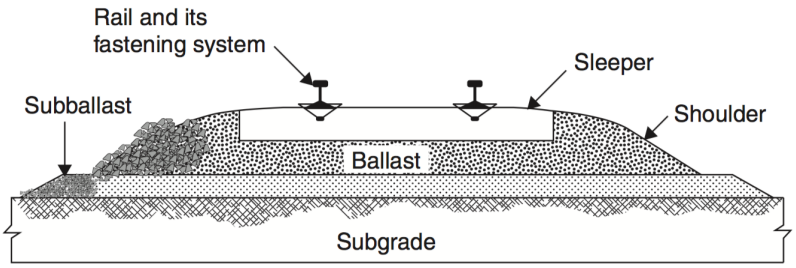

(b) Schematic view of a classic ballasted railway track, extracted from Indraratna [116]

FIGURE 1.1: Ballasted railway track.

The fastening system connects the sleepers to the rail through the rail pad. This pad absorbs the impacts on the rail and helps to reduce the fretting fatigue in the sleepers, specially in the concrete one. Fasteners are used to ensure no relative displacement between sleepers and rail. They keep the geometry of the track within acceptable tolerance.

The sleepers allow to transfer the lateral, longitudinal, and vertical loads from the rail/rail pad system to the ballast/concrete layer over a wider area. The sleepers' strength and stiffness must be sufficient to maintain a steady shape and smooth track configuration as well as to resist the vehicle forces. The assembly rail-fastening system-sleeper maintains the rail gauge, which is 1435 mm in France. Until World War II wooden sleepers were used in almost all countries [114]. In the last decades, they were replaced by pre-stressed reinforced concrete sleepers, with better nominal life.

The ballast is a granular layer that supports the sleepers and transfers the forces from the rail and sleepers to the sub-ballast and soil. It is made of coarse crushed stone with a grain size distribution in the range of 25-50 mm. More details are provided in the following section. On high-speed lines (HSL), an extra layer is added to the track, called sub-ballast. It protects the ballast from rain run-off and water flow, as well as from frost growth.

The subgrade is the ground over which the railway track is built. It should have proper stiffness and bearing capacity to resist traffic loads. It is composed of geomaterials whose response may be nonlinear and influenced by the initial state, stress history, plastic deformation rate, water content, and other variables [12]. Two different kinds of geomaterials can be used: i) natural ground, and ii) placed soil (fill). The latter is used on French HSL.

1.1.2 The ballast layer

The origin of the term "ballast" comes from the stones used to give stability to the ships [239]. On railway tracks the ballast provides geometrical stability to the sleepers against vertical, longitudinal and lateral forces generated by the passing of the trains, exactly like it does in boats. The ballast transmits large load distribution at the sleeper/ballast surface to the ballast/subgrade surface at a lower stress level. It provides sufficient permeability for drainage (standing water can rapidly damage the track) and inhibits weed growth by reducing fouling.

At the beginning of the railway era, the ballast was composed of soil and loose stones. Cinders dumped from the locomotive fireboxes were used during the 19th century. Today, crushed stone is the most common material used for the construction of ballasted tracks. The size and type of stones used for each track depends on the nature of the track and on availability. The main advantage of crushed stones and gravels is the capability of self-locking of the particles, reducing drastically the track movement [239]. The ballast gradation can change from region to region. In France, the admissible granulometry for the ballast grains follows the norm EN 13450, presented in Fig. 1.2(a). In Australia, the standard AS 2758.7, presented in Fig. 1.2(b), dictates the ballast gradation. Although clearly influential [17, 205, 25], the shape of the grains is not controlled.

The thickness of a ballast layer depends mainly on the size and spacing of the sleepers, on the amount of traffic, and on the type of line. Insufficiently deep ballast may yield overloading, with subsequent sinking of the track. Thin ballast layers may also lead to unacceptable vibration levels because they do not provide sufficient resiliency, strength and energy absorption [28, Section 4.2]. On conventional lines, the thickness of the ballast is approximately 150 mm, while it stands around 500 mm on HSL [239]. The ballast shoulder should be at least 150 mm wide to limit the lateral movements of the track.

The most traditional method for maintenance of the ballast layer is tamping [116]. This operation consists of lifting the track (rail, fastening system, and sleepers) and replacing fouled ballast by fresh grains one, before setting the track back at its place. However, this process damages the ballast by loosening the ballast bed and reducing track resistance to

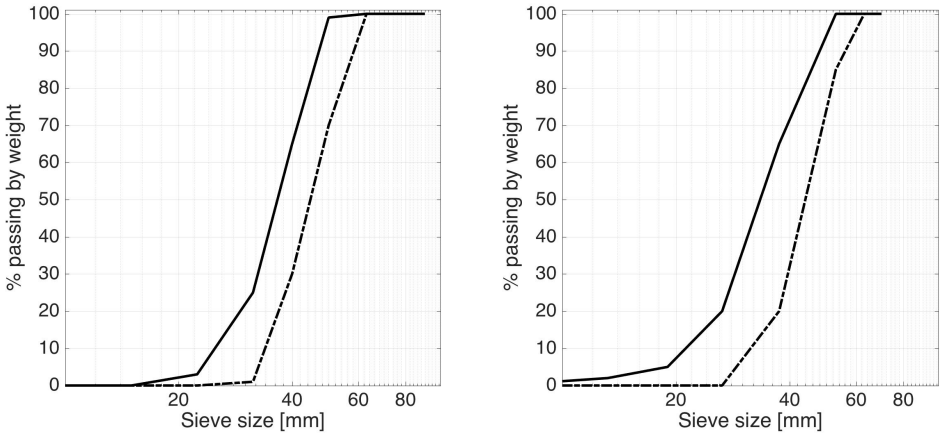

(a) Ballast gradation proposed by EN 13450 (b) Ballast gradation proposed by AS 2758.7

FIGURE 1.2: Ballast gradation proposed for railway ballast. The solid line represents the maximum limit, and the dashed line the minimum limit.

lateral displacement and buckling. The process also produces fines which impair drainage. Therefore, tamping is usually followed by a dynamical stabilization process. The latter consists in vibrating the track laterally, while a vertical load is applied. Under this loading, the ballast rearranges itself without impact and performs better for lateral stability. Stoneblowing or pneumatic ballast injection is an alternative method which aims at reducing the creation of fines during tamping [116]. It consists in lifting the track and filling the voids with small single size stones, thereby creating a two layer granular foundation for each sleeper. When the concentration of fines yields a threshold value the ballast must be cleaned or replaced by fresh ballast [116].

The modelling of the ballast aims at improving the understanding of the mechanical behaviour of the track system and providing clues to mitigating the issues listed above [106, 63]. It represents a challenging task because granular materials exhibit various distinct and complex behaviours. To illustrate this, some experimental observations on granular samples are reported in the next section, not necessarily limited to the ballast.

1.2 Dynamical behavior of granular materials

A granular material is a biphasic medium where one of the phases is solid and the other is fluid. The main distinction between this medium and other multiphase medium is the discrete nature of the solid phase. This characteristic turns into a high dependency of the mechanical behaviour on the contact chains between grains at the instant analyzed. The contacts between the grains are the key aspect of the granular medium, and the mechanism that transfers the loads inside a granular medium is called chain of forces. These chain of forces produce a highly non-linear and dissipative behaviour due to the rearrangements of the grains and the contact friction.

The distribution of these contact forces can be broadly analyzed into two groups. Lower-than-average contact forces have a nearly uniform distribution while larger-than-average forces present an exponential falloff [144, 83, 192, 164]. The strong network of forces holds almost all the shear strength of the granular medium [192, 191], producing very localized load transfer paths [91]. On the other hand, the weak forces are mostly perpendicular to the strong force chains and help to stabilize the latter. These weak forces contribute considerably

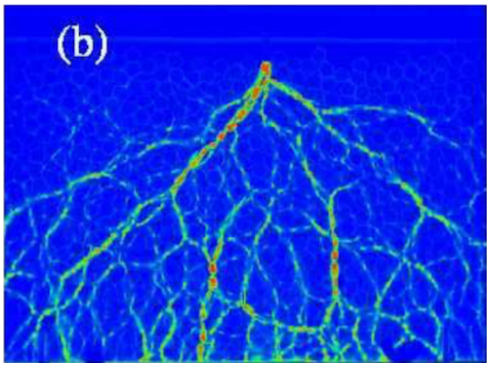

FIGURE 1.3: Photoelastic experiment in granular medium subjected to a point load and gravity, extracted from Geng *et al.* [91]. The color scale represent the amplitude of the load from high loads (red) to lower loads (blue).

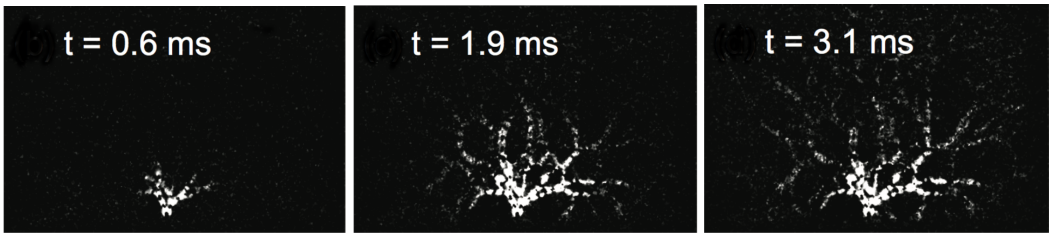

FIGURE 1.4: Wave propagation in granular medium capture by photoelastic measurement, extracted from Owens and Daniels [177]

to the anisotropy of the medium, and they are sensitive to the packing state resulting from the deformation history [192, 191, 16, 237]. From an experimental point of view, granular materials are therefore extremely heterogeneous and anisotropic. These properties were verified with photoelastic experiments in 2D arrangements under shearing and gravity at the microscale [231, 91, 150, 268]. Fig. 1.3 displays force chains as observed by photoelasticity in an assembly of monodisperse pentagonal grains submitted to their own weight and a vertical point load localized on one grain at the top of the sample [91].

Wave propagation can be captured with similar photoelastic experimental setups. For instance, Fig. 1.4 presents an experiment on a polydisperse arrangement of disks [177], where a voice coil affixed to the bottom wall of the system sinusoidally drives a flat platform. The figures display snapshots at different times, showing the propagation of the wave in the medium, and illustrating the heterogeneous behaviour of the phenomenon (the video of this experiment is available[1]). These chains are inherently fragile and susceptible to reorganization [143]. Three-dimensional configurations [103] and stress fields [264] were studied in more recent years using x-ray tomography and neutron diffraction.

Liu and Nagel [143] performed an experiment on a square box with a side length of 28 cm with a depth of 8 cm to 15 cm filled with 5 mm glass spheres. A speaker attached to a plate buried in the granular material produced compression waves, which were measured at accelerometers embedded at distances from 2 to 10 cm from the source. Through time delay, the mean velocity was measured at 280 m/s, which is much lower than the wave propagation velocity in glass (around 4000 m/s). One of the explanations for this observation is that the stress waves are carried by the force chains, so that they do not travel along straight lines. The waves are carried grain by grain, through the contacts between grains, making the path relatively longer and reducing the effective velocity of the wave.

[1] http://nile.physics.ncsu.edu/pub/movies/gransound/

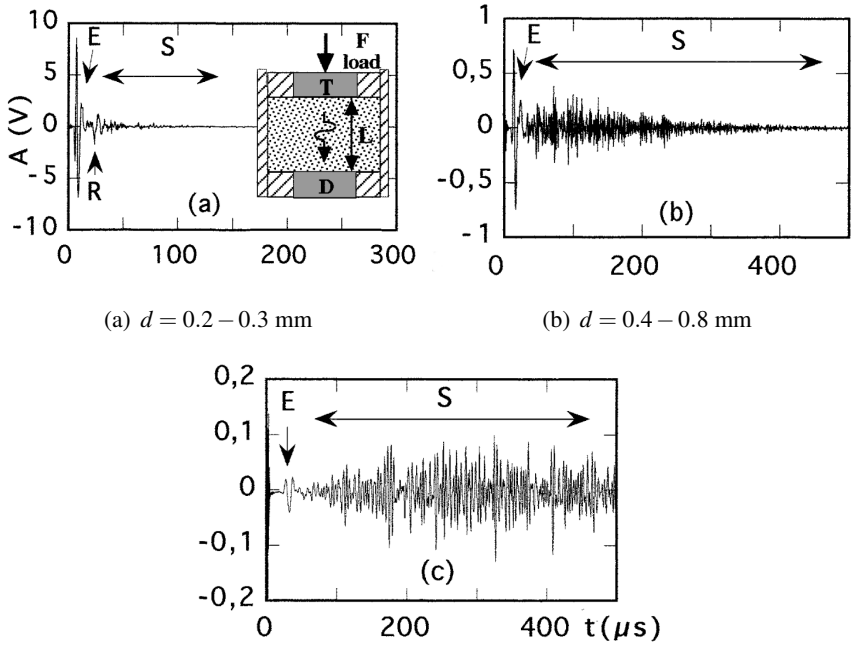

(a) $d = 0.2 - 0.3$ mm

(b) $d = 0.4 - 0.8$ mm

(c) $d = 1.5 \pm 0.15$ mm

FIGURE 1.5: Ultrasonic signals measured in a glass bead packings of different sizes under external normal stress $P = 0.75$ MPa, extracted from Jia *et al.* [123].

Another influence of the heterogeneity of the medium on wave propagation was studied by Jia *et al.* in a prestressed cylindrical sample filled with polydisperse glass beads [123]. An ultrasonic wave pulse was generated by an ultrasonic transducer and measured by an ultrasonic detector after propagation inside the medium (see the schematic view of the apparatus in Fig. 1.5). As shown on Fig. 1.5, two important phases were observed in the measured response, with different relative amplitude depending on the diameters of the grains (relative to the wavelength). The first phase (E) corresponds to a coherent pulse, propagating at an average velocity and with apparent damping. The second phase (S) corresponds to an incoherent pulse (the so-called coda in seismic engineering), generated by the scattering of impulse waves at each contact between grains. Fig 1.6 shows that the low-frequency range of the excitation propagates mostly coherently while the high-frequency range is preferentially diffracted. On the same experimental setup, the authors also checked the influence of contact pressure between grains P on the propagation velocity v of the coherent pulse. The later is shown to scale as $v \propto P^{1/6}$ for the higher pressures and $v \propto P^{1/4}$ for the lower pressures, as predicted by the effective medium theory [97].

Very similar results were obtained by Gilles and Coste [96] in an hexagonal lattice of spherical steel beads under isotropic stress, using beads with different diameters to create a disordered lattice of particle contacts (see Fig. 1.7 for schematic view of the setup). The velocity scales as $v \propto P^{1/4}$ for confinement pressures below a certain threshold, and as $v \propto P^{1/6}$ above. They also reported on the reversibility of the wave propagation phenomenon, by measuring velocity in the compression and decompression phases (see Fig. 1.8) and showing they are almost equal.

We finally report on some experimental observations more directly related to ballasted railway tracks. After increasing the commercial velocity from 270 km/h to 300 km/h on the Paris-Lyon HSL (in 2001), measurements showed that the permanent deformations in the track were larger than predicted. Al Shaer *et al.* [9] prepared a reduced scale laboratory test

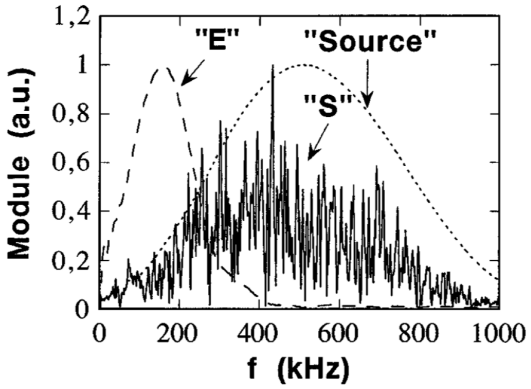

FIGURE 1.6: Spectra of the E and S signals windowed from the total temporal response for $d = 0.4 - 0.8$ mm, and the source spectrum source, extracted from Jia *et al.* [123].

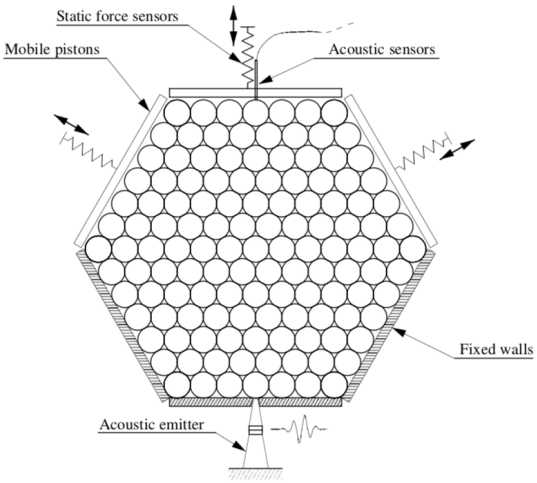

FIGURE 1.7: Experimental setup for the isotropic confinement stress, extracted from Gilles and Coste [96].

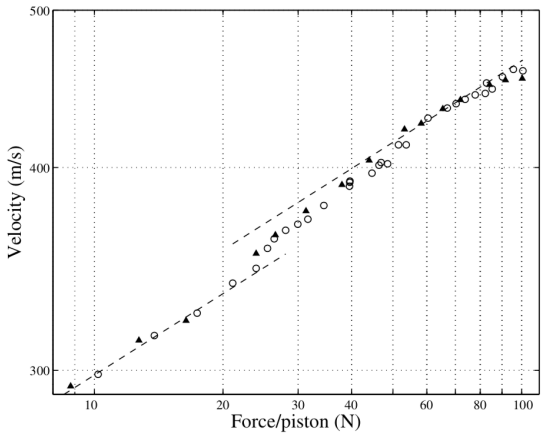

FIGURE 1.8: Velocity vs force plotted in log-log scale. The filled triangles represent the measurement made during the decompression, while the circles were measured during the compression phase. Extracted from Gilles and Coste [96].

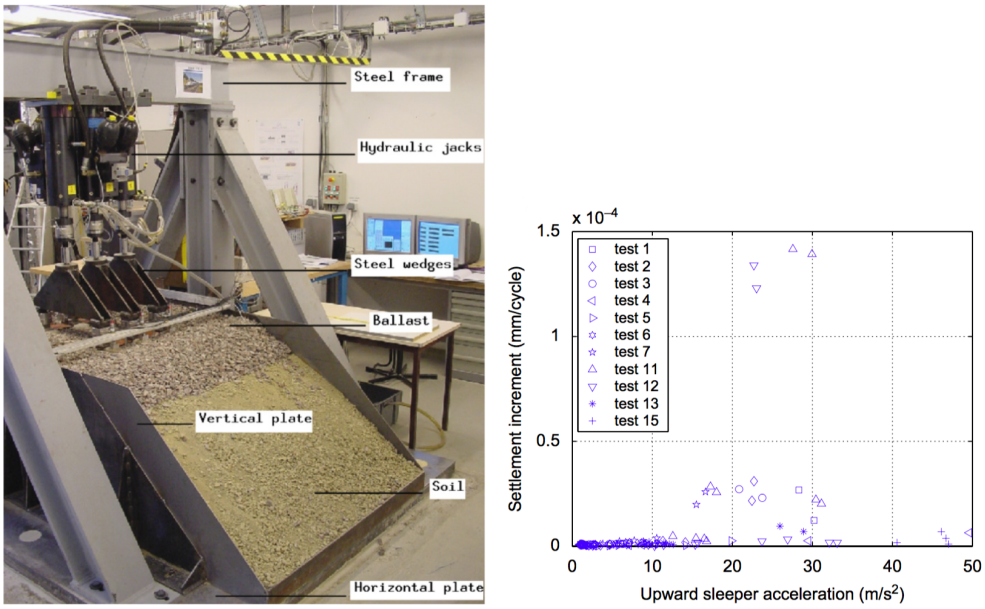

(a) Experimental setup used in the test

(b) Settlement of the sleeper versus the acceleration of the sleeper

FIGURE 1.9: Laboratory setup experiment and settlement of the sleeper, extracted from Al Shaer *et al.* [9].

to show the influence of the train speed on the ballast response. A portion of ballasted railway track was built with three sleepers in a steel frame. The passage of a train at different velocities was reproduced through the use of hydraulic pistons. Fig. 1.9 shows the experimental setup and the settlement of the sleeper versus the acceleration of the sleeper, which is directly related to the train velocity. When the settlement is analysed in terms of the acceleration of the sleepers, a threshold value, around 20 m/s^2, clearly arises. Above that threshold, the ballast layer suffers an important additional settlement per load cycle, with larger variability for large accelerations. In quasi-static or low-dynamic conditions (low-speed train) the settlement seems to follow the Bodin settlement law [219]. Above the threshold, the observation is coherent with those of the Paris-Lyon HSL, but the phenomenon is not yet fully understood.

1.3 Modelling of ballasted railway tracks

Granular materials, and among them the ballast, therefore present complex dynamical behaviors that are sometimes counterintuitive. This section introduces some of the models that have been proposed in the literature to reproduce these behaviours, with an emphasis on the phenomena each model is able to reproduce, as well as a list of their limitations. Two classes of models are considered: (1) discrete models; and (2) continuum models.

1.3.1 Discrete models of the ballast layer

The relative displacements between two grains in the ballast layer are in general much larger than the strains within one grain. Models can then be build [142] where each grain of the ballast is a rigid body with a complex shape [148, 8]. These models have given rise to various numerical implementations, among which the DEM [66] and the Non-Smooth Contact Dynamics method (NSCD) [163]. In the DEM, the non-interpenetration condition at the interface between two grains is relaxed through a stiff non-linear repulsion law. This gives rise to an explicit scheme in time. This kind of numerical integration requires very small time

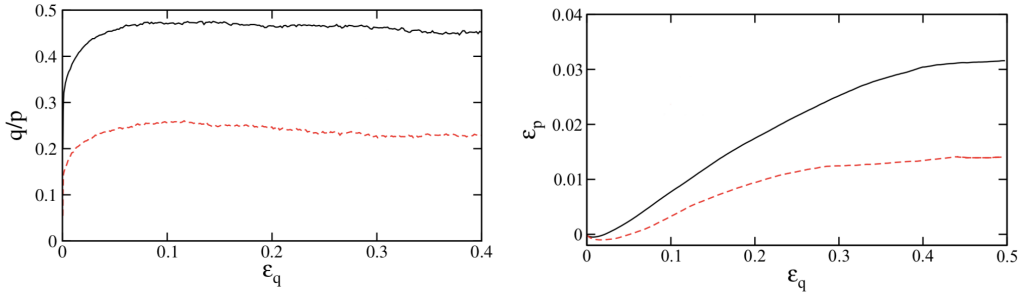

(a) Strength parameter, q/p (b) Volumetric strain

FIGURE 1.10: Complex behavior of granular media as a function of shear strain ε_q, with irregular ballast grains (black line) and spheres (red line) under quasistatic shearing, extracted from Azéma *et al.* [25].

steps and needs to handle the changes in the topology. The NSCD method can deal with multiple contacts and velocity changes within a single time step and reformulates the non-interpenetration condition as a quadratic optimization problem. It yields an implicit scheme, which remains stable for larger time steps.

The results obtained with these granular approaches are able to reproduce the solid to liquid transition and the inelastic deformations of the ballast [83, 192, 25] as well as the seemingly random patterns of contact forces [144, 31] that can be observed experimentally at that scale [74]. Because of the numerical issues mentioned above, however, these models cannot reproduce dynamical phenomena involving the passage of a train over a large portion of a track. Also, the requirement of inputting a precise geometry [228] and an initial position of the seemingly random assembly of grains is straining for most industrial applications, even though large databases of digitized ballast grains have been created [25]. The NSCD method was largely applied to the modeling of the ballast [210, 213, 61, 212]. Tests like penetrometer test [187], analysis of the stability [189], settlement [188, 215], compaction [211, 86] and degradation [70] were reproduced. The dynamic behaviour of a confined granular medium and the tamping process were also modeled [27, 24, 26, 214].

To illustrate the kind of behavior that these discrete models can reproduce, we report on one particular example. A sample of digitized ballast grains was submitted to a compression test, reproducing a classical laboratory setup for granular materials. Fig 1.10(a) and 1.10(b) reproduce the ratio of deviatoric stress to mean stress and the cumulative volumetric strain as functions of the cumulative shear strain, obtained using the NSCD method [25]. The ratio of mean stress to deviatoric stress presents a hardening behaviour, followed by softening and a plateau (corresponding to the critical state of soil mechanics [158]), while the volumetric strain displays a dilatancy property [198]. Both of these are well-known behaviours of granular media, which shows the capability of NSCD to efficiently reproduce complex phenomena typical of granular media.

Unfortunately, there is no report in the literature of works using discrete models to reproduce large scale dynamical phenomena in ballasted railway tracks. One of the reason is probably the lack of scalability of the NSCD method [197, 108, 10, 263]. The latter is a measure of a parallel computer's capability to solve larger systems when provided with a more powerful computer (see Amdahl's law [13] and Gustafson's law [102] for a formal definition of some scalability metrics). Hoang *et al.* [108] illustrated this lack of scalability using domain decomposition and a shared memory parallelization paradigm, for the simulation of a granular sample contained in an open cubic box of 0.5 cm edge with 2000 grains (polyhedral shape) submitted to a harmonic force. Fig. 1.11 shows a strong decrease of efficiency when the number of processes increases. This is related to the relatively larger time that the

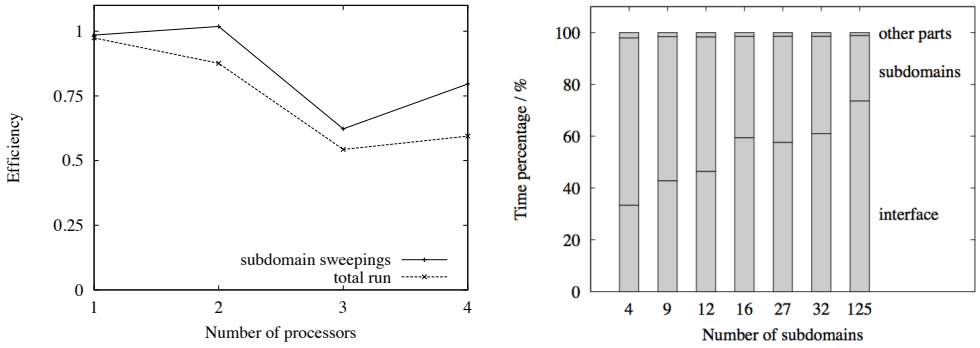

(a) Efficiency against number of process (b) Time percentage against number of subdomains

FIGURE 1.11: CPU time and numerical efficiency in OpenMP implementation, extracted from Hoang *et al.* [108]

algorithm spends in communications between processors when the number of subdomains increases.

In the railway context, another more minor issue arises with discrete models. The coupling between the ballast layer and the soil, which can be efficiently modeled as a continuum medium, remains a challenge. Complex two-scale models can be introduced [263], coupling discrete and continuum models at the interface, for instance by the Arlequin method [71, 72, 218]. Such an issue arises in particular from the incompatibility of continuum models to support point loads [92], while discrete models cannot accommodate surface loads.

1.3.2 Homogenization approach for continuum models of the ballast layer

An alternative approach consists in modelling the ballast as a continuous medium, using the stress tensor as the static variable and the displacement field as the kinematical variable. The stress and strain tensors can be derived, respectively, from the contact forces network [262, 209, 34, 162, 216, 166] and the displacements of the grains [253, 134, 50, 30, 201, 77] in discrete simulations. However, the relation between the parameters of the continuum and granular models is not obvious. Such continuum models have been developed along various directions [183, 15]:

1. phenomenological approaches, that consist in postulating the form of the energy functional, introducing a heuristic constitutive relation, generally non-linear, through observation of experimental results.

2. homogenization approaches, in which an equivalent homogeneous energy functional is derived from mathematical considerations and asymptotic analysis; these approaches can be extended to higher-order continuum approaches (such as Cosserat models [243]), with the introduction of additional degrees of freedom and non-local continuous operators;

Phenomenological approaches have yielded a wide variety of non-linear models, either oriented to the description of granular flows [113, 90, 124], or of static pilings [151], including the consideration of wave propagation [97, 141]. The homogenization of granular structures has been widely studied, for general lattice structures [160, 249, 154, 173, 104], random packings of spheres [43, 73, 260, 59, 58, 122, 7], as well as railway ballasted tracks [155, 159, 224, 31]. Generalized continua can then be used, such as for instance higher order medium [39, 243, 79, 157]; non-local theories [236]; gradient medium [94, 93, 19, 181], and gradient with non-affine displacement field [152].

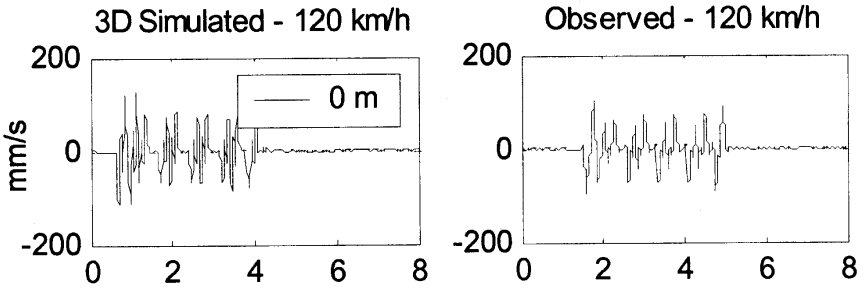

(a) Velocity comparison at 0 m away from the track

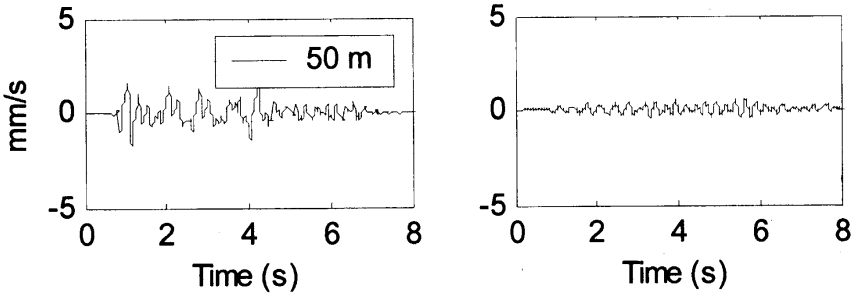

(b) Velocity comparison at 50 m away from the track

FIGURE 1.12: Velocity comparison between a SEM model and observed measurements, extracted from Paolucci *et al.* [180]

As these models are based on homogeneous parameters, they cannot reproduce the heterogeneity of the stress fields that is experimentally observed. However, most of these continuum models can be efficiently implemented in parallel algorithms to understand the dynamical behavior of ballasted railway tracks over very large scales. For instance, Paolucci *et al.* [180] proposed a numerical model, based on Spectral Element Method (SEM), to predict the low-frequency ground vibrations induced by the passage of HST at Ledsgaard, Sweden. The acceleration was recorded from a series of train passages with different constant velocities, between 70 and 200 km/h. The accelerometers were located at various distances, up to 50 m from the track, and depths, and numerical models (2D and 3D) were used to predict the vibrational levels on and away from the track. The comparison with experimental results was satisfactory for the vibrational response on the track. On the other hand, at distances further away, an over-estimation of the level of vibrations appeared in the model, as shown in Fig. 1.12. In other words, the homogeneous continuum model used in [180] seems to be lacking a dissipation mechanism that would allow to reproduce the measurements more accurately.

1.4 Objectives and contributions

Both the discrete and continuum approaches are interesting in their own right. The discrete approaches provide very detailed information about the micro-mechanical heterogeneity and behaviour of the granular system, but the numerical simulation of large packings is out of reach. The continuum-based models are more manageable on a large scale but they lose the heterogeneity of realistic force networks, which has been shown to be fundamental to explain many granular phenomena.

The objective of this thesis is to explore an intermediate approach. The ballast is modelled, as in the classical homogenization approaches, by a classical continuum medium, but with heterogeneous mechanical properties, fluctuating over a characteristic scale similar to

the diameter of the ballast grains. Because of the heterogeneity of the material parameters, the stress and strain fields fluctuate within the continuum sample, as in a realistic granular medium. As the model is continuum-based, very efficient parallelized numerical techniques allow to solve large-scale dynamical problems. To simplify the parametrization of the field's fluctuating property, a stochastic model is used. Hence, the model is parameterized only by statistical information (average diameter of the particles, mean, variance and autocovariance of the mechanical property). These parameters have to be experimentally identified, through inverse problems using numerical granular models or experimental measurements. The influence of the heterogeneity on wave propagation in ballasted railway tracks and the surrounding environment has to be carefully analyzed.

Besides the introduction, this thesis is structured as follows :

- The next chapter is the core of this work. It introduces the randomly-fluctuating heterogeneous continuum model that constitutes the main novelty of this thesis. The first-order marginal density and correlation structure of the proposed stochastic model of the Young's modulus are careful presented. To identify the model parameters, an inverse problem is set up, using as reference static NSCD simulations of ballast samples under vertical compression and lateral confinement. The results of this chapter were published in Computational Mechanics [5]. The publication of this paper was accompanied by an international press release of Institut National des Sciences de l'Ingénierie et des Systèmes of CNRS, SNCF Innovation & Research and INSA Strasbourg[2].

- Chapter 3 proposes a detailed analysis of the influence of heterogeneity on wave propagation in a ballasted railway track. Using time-space data provided by a large scale numerical simulation with the spectral element method, the dispersion curves for a ballasted railway track are constructed. A very interesting phenomenon of Anderson localization is observed and discussed. The results of this chapter were submitted as a journal paper to Journal of Sound and Vibration [4].

- Chapter 4 presents an first analysis of two experimental datasets that will be used to identify the parameters of the randomly-fluctuating heterogeneous continuum model on dynamical data. The first set of measurements was obtained on a small scale in the laboratory, using a so-called ballast pool, which is a simple box containing ballast grains. The second dataset consists in accelerations recorded during the passage of several HST on an HSL. For lack of time, only preliminary analyses can be proposed in this document.

- Conclusions arising from this work and suggestions for future research are presented in Chapter 5.

[2] http://www2.cnrs.fr/sites/en/fichier/cp_ballast_vf_anglais_web.pdf

Chapter 2

Randomly-fluctuating heterogeneous continuum model of a granular medium

The objective of this chapter is to develop a continuum model that represents, statistically, a granular medium. To start, we should remember the discrete and heterogeneous characteristic of the granular media, as discussed in the Section 1.2. The passage from the discrete medium to a continuum one can be made using phenomenological or homogenization approaches. In the homogenization process, the contact forces and grain displacements are replaced by one kind of stress tensor (static variable) and the displacement field (kinematical variable). The homogenization method consists in: search a functional of the energy that satisfies the Hill-Mandel criteria [271]. It means: the virtual work made in a Representative Volume Element (RVE), subscale, is equal to the virtual work made in an equivalent homogeneous media [271], macroscale. This procedure leads us to an apparent homogeneous property for the material [111, 112, 126]. However, one of the main hypothesis used in the classical homogenization, the scale separation [156], is not satisfied in the problem studied by this thesis. In this case, or when we want a finer resolution for the continuum, we should employ a Statistical Volume Element (SVE), which leads to heterogeneous random continuum fields [174, 76].

We choose to represent the granular media using a randomly-fluctuating heterogeneous continuum model. The model will consider the small displacements regime, without non-local theory, in a linear isotropic elastic medium. It will allow us an easy coupling with the soil layer beneath the ballast. The proposition of a stochastic heterogeneous model to replace the granular material is presented in the first section (Section 2.1) and constitutes the core of the chapter. The following subsection (Section 2.1.1) describes discrete numerical samples of a granular medium, whose normal force distributions can be simulated with the NSCD. These simulations are used to identify the random model of Young's modulus. Section 2.2 presents a comparison between the results obtained in Section 2.1.1 and the model present in Section 2.1.

2.1 Stochastic Heterogeneous Continuum model

In this section, a random model of Young's modulus is introduced. While we limit ourselves to this parameter a similar model could be proposed for other mechanical parameters, such as the density or the Poisson ratio. However, the identification process might have to be adapted depending on the parameter considered. The random field is assumed stationary and ergodic, and its first-order marginal law and correlation model are described below. Most parameters are based on geometrical and mechanical information of granular particles, obtained directly from the observation of discrete samples, and summarized in Section 2.1.2.

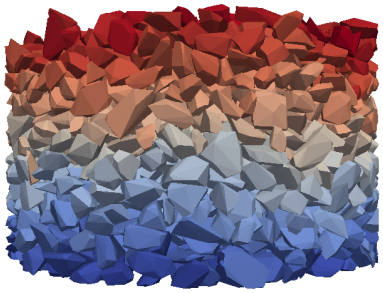

FIGURE 2.1: Example of one of the 29 samples of granular medium simulated with the NSCD.

The only exception is the variance, that is identified by the solution of an inverse problem in Section 2.2. To begin, a description of the discrete numerical samples of ballast are presented (Section 2.1.1). They were used as the reference for the identification process, and to extract some of the model parameters.

2.1.1 Discrete model of a granular medium and numerical samples

This section introduces discrete samples of a granular medium, and describes the distribution of the force chains, as estimated with the NSCD. These samples will be used to identify the parameters of the randomly heterogeneous continuum model in Section 2.2. The link with the continuum models is performed through equivalent stresses.

Description of the discrete numerical samples

We consider 29 samples of 2700 granular particles, on average, contained in cylindrical boxes with a radius of R =35 cm and a height of H =39 cm (see Fig. 2.1). The particles are convex polyhedra with diameters between 2.5 cm and 5 cm, whose shapes have been obtained by digitalization from real ballast [25]. The 2700 granular particles are randomly drawn from a larger database so the particles are not the same in all samples. An isotropic confinement pressure of 60 kPa is applied on all samples. A vertical load of 63 kN is also applied on the upper face. Gravity is considered within all samples, with particles having a density of 2700 kg/m^3. Contact forces in each of the samples are estimated using the LMGC90 software [146], which is built on the NSCD and considers Coulomb dry friction and mutual exclusion as contact laws. The preparation (creation of the granular assemblies by free fall of randomly-rotated particles in the cylindrical box from grid positions in the air) and simulation of one granular sample takes on average 6200 s of CPU time.

For each sample, only the contacts contained within a $48 \times 48 \times 32$ cm^3 hexahedral box are considered, to limit the influence of the boundary conditions. Finally, results from the 29 samples can be aggregated, yielding approximations of the distribution of the contact forces. For instance, Fig. 2.2 presents the probability distribution function for the normal contact forces normalized by their average value estimated from the 29 samples and plotted in log-log scale.

In the literature, there seems to be a consensus about the exponential distribution for the modelling of the probability distribution of higher-than-average normal forces (so-called strong forces). This consensus is built at the same time over theoretical considerations [64, 31, 81], experimental evidence [155, 164, 252, 109] and numerical simulations [167, 191]. For the samples considered here, the higher-than-average force distribution is proportional to:

$$p(f_n) \propto \exp\left(\beta \frac{f_n}{\langle f_n \rangle}\right). \tag{2.1}$$

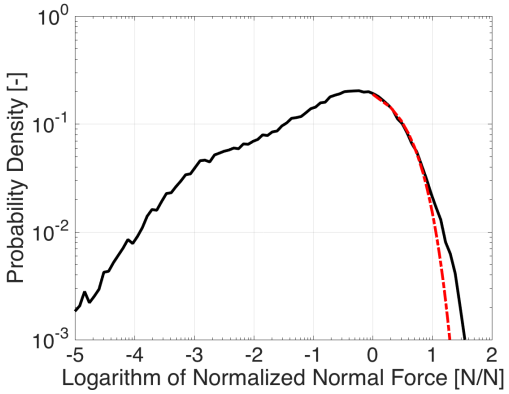

FIGURE 2.2: The probability density function of the logarithm of normal contact force normalized by its average (solid line), and exponential approximation (dashed line, see Eq. (2.1)).

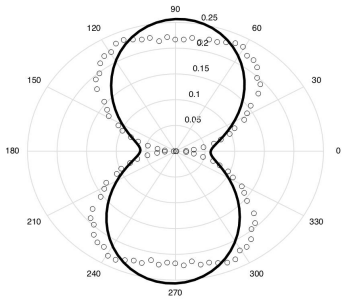

FIGURE 2.3: Anisotropy of the normal contact force distribution, averaged over the 29 discrete samples (in circles), and first spherical harmonic approximation (solid line, see Eq. (2.2)).

where $\beta = 1.13$. Note that the latter value is compatible with the values found in the literature $0.88 < \beta < 1.71$ [22, 194, 204], and matches the coefficient of [25], obtained for similar samples. For lower-than-average forces, the situation is not so clear and several models are competing [155, 78, 109]. In that respect, the size of the particles [155], the shape of the particles [25], and the mean packing fraction [109] seem to be influential.

Finally, the anisotropy of the behaviour is reflected in Fig. 2.3 and well approximated by the following spherical harmonic model [193, 23]:

$$P_n(\phi) \approx \frac{1}{2\pi}[1 + a_c(3\cos^2(\phi - \phi_c) - 1)], \tag{2.2}$$

where $a_c = 0.3$ is an anisotropy parameter related to the fabric tensor [193]. The coefficient $\phi_c \approx 0.03$ rad is the most probable contact angle. As is the case here, it is usually collinear with the principal load direction.

Fig. 2.4 presents the probability distribution functions of the different components of the equivalent stress σ^V, Eq. 2.3, (in a cylindrical basis) for different averaging volumes in a cube: $V = (2\text{ cm})^3 = 8\text{ cm}^3$, $V = (4\text{ cm})^3 = 64\text{ cm}^3$ and $V = (8\text{ cm})^3 = 512\text{ cm}^3$. Due to the type of loading, the vertical component σ^V_{zz} is obviously much larger than the other components. It is also clear that the distributions are wider (there is more variability) when the averaging volume is smaller. When averaging over larger volumes, a more homogeneous

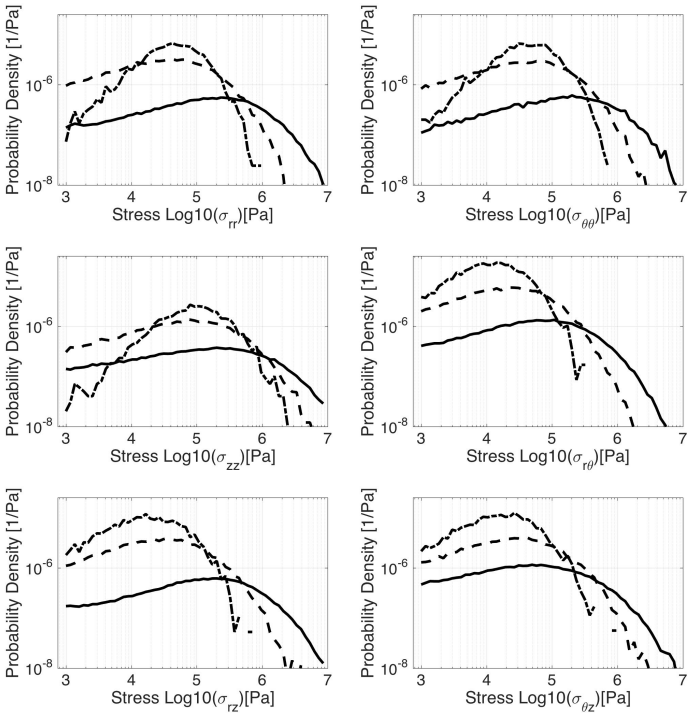

FIGURE 2.4: Probability distribution functions of the different components of the equivalent stress σ^V, as a function of the averaging volume: $V = (2\,\text{cm})^3$ (solid line), $V = (4\,\text{cm})^3$ (dashed line) and $V = (8\,\text{cm})^3$ (dash-dotted line).

distribution is obtained, less variable and more clustered around the average value. Unfortunately, the tails of the distributions are not well represented, once that only 29 samples were available to evaluate Eq. 2.3.

Notion of equivalent stresses and relation between discrete and continuum models

The forces in a granular model are point forces localized at the interface between grains. These quantities have no counterpart in continuum models. It is however possible to define generalizations of the notion of stress tensor to discrete medium. Several proposals have been made in static [74, 200, 161] and dynamic regimes [98, 216]. The equivalent stresses for static (or quasi-static) loads is introduced here. Given a network of contact forces f^c_α (at contact points c and with coordinates α) in a granular medium, the equivalent stress field [147, 262, 161, 249, 257, 168] is defined as

$$\sigma^V_{\alpha\beta} = \frac{1}{V}\sum_{c=1}^{N_c} f^c_\alpha \ell^c_\beta = n_c \left\langle f_\alpha \ell_\beta \right\rangle = \sigma^V_{\beta\alpha}, \tag{2.3}$$

where ℓ^c is the so-called branch vector, linking the centres of the two particles in contact at c, the sum in Eq. 2.3 is on the N_c contact points in a cell with volume V, and $n_c = N_c/V$ is the density of contacts (see [262] and Section B.1 for more details). Obviously, this quantity depends on the size of this averaging cell volume (with more variability over the whole sample for smaller averaging volumes). One of the main advantages of this definition is that it makes sense from the smallest scale (e.g. one contact point) to the largest one (e.g. the sample).

It is also an additive quantity, with respect to the volume (Lebesgue) measure. However, the definition of an equivalent tensor of deformations has not yet found a consensus: several propositions have been made [32, 132, 50, 201, 51]. One proposition was detailed in the Section B.2.

2.1.2 Geometrical information on the granular packing

The average diameter is defined as the mean (over all contacts and all samples) of the branch vector lengths:

$$\underline{d} = \left\langle \frac{1}{N_c} \sum_{c=1}^{N_c} |\ell^c| \right\rangle, \tag{2.4}$$

where $\langle \cdot \rangle$ indicates an average over all discrete samples. In the set of cylindrical samples that we considered, we obtain $\underline{d} \approx 3.9$ cm. Alternatively, in the context of ballasted railway tracks or other engineering works, it would be possible to identify that average diameter directly from the normalized granulometry curves. Using for instance the minimum and maximum ballast gradations proposed by the standard EN 13450 (Fig. 1.2), one obtains average diameters between $\underline{d} = 3.6$ cm and $\underline{d} = 4.5$ cm.

On the same granular packings, we can also measure the packing density, defined as the volume of the grains relative to the total volume of the cylinder:

$$\underline{\phi} = \left\langle \frac{V_{\text{grains}}}{\pi R^2 H} \right\rangle, \tag{2.5}$$

where V_{grains} indicates the cumulated volume of all the grains in a given sample. Note that, as we will consider a continuum model with volume $\pi R^2 H$ (that is to say with no holes), we will consider a density

$$\rho = \underline{\phi} \rho_{\text{grains}}, \tag{2.6}$$

where ρ_{grains} is the density of the constituent of the grains. This diminished density ensures that the total weight of the continuum samples will be the same as that of the discrete samples. In our model we use for density model: $\rho_{\text{grains}} = 2700$ kg/m^3, $\underline{\phi} = 0.5830$ and $\rho \approx 1574$ kg/m^3.

2.1.3 Correlation model for Young's modulus

Considering the geometrical information above, a correlation model for the random field of Young's modulus is now chosen. In order to propose a theoretical correlation model, we assume in this section that the considered material is idealized as a two-phase medium: void matrix and impenetrable spheres. Even though the random field of Young's modulus corresponds to a unique phase, it is believed that proceeding this way will provide an appropriate order of magnitude of the scale of fluctuations in space. The amplitude of fluctuations (variance) will be identified in Section 2.2. We propose to consider the correlation structure of a dense packing of impenetrable spherical particles of diameter $\underline{d}$, with volume ratio $\underline{\phi}$, developed by Torquato and coworkers [251, 250, 190]. This function depends only on $\underline{\phi}$ and $\underline{d}$, and shows in particular the impenetrability condition and cosine decaying behaviour, more pronounced with increased volume ratio, as can be noted in Fig. 2.5. Usually, the correlation function is based on the probability that n spheres of radii $a_1, \ldots, a_n$ centered at positions $\mathbf{x_n}$, respectively, are empty of inclusion centers. However, it leads to a sum of infinite number of terms [250]. We choose the Meyer representation of the canonical function S_n (denoted H_n in the book [250]). This theoretical correlation model is based on the approximation made by Ornstein-Zernike in a 2-point matrix probability function the correlation $S_2(r)$. Now the

correlation model can be written as a sum of a finite number of terms. Formally, this relation reads:

$$S_2(r) = 1 - \underline{\phi} V_2(r) + \underline{\phi}^2 \mathscr{F}^{-1}\left[\tilde{m}(k)^2 \frac{\tilde{c}(k)}{1-\underline{\phi}\tilde{c}(k)}\right], \tag{2.7}$$

where $\mathscr{F}^{-1}[\cdot]$ denotes the inverse Fourier transform of a function, k is the spatial frequency, $\underline{\phi}$ (denoted ρ in the original papers [251, 250, 190]) is the number density of the particles or volume ratio and $V_2(r)$ is the normalized volume of the union of two spheres whose centers are separated by r, equal to

$$V_2(r < \underline{d_w}) = \frac{4\pi}{3}\left(1 + \frac{3}{4}\frac{2r}{\underline{d_w}} - \frac{1}{16}\left(\frac{2r}{\underline{d_w}}\right)^3\right) \tag{2.8}$$

for $r < \underline{d_w}$ and $V_2(r > \underline{d_w}) = 8\pi/3$ otherwise. The Fourier transform of the indicator function of the particle (equal to 1 inside the particle, and 0 outside) $\tilde{m}(k)$ is equal to

$$\tilde{m}(k) = \frac{4\pi}{k}\left(\frac{\sin k}{k^2} - \frac{\cos k}{k}\right) \tag{2.9}$$

and, using the Percus-Yevick approximation [184] corrected by Verlet-Weis [256], the Fourier transform of the direct correlation function is given by:

$$\begin{aligned}\tilde{c}(k) = -\frac{4\pi}{k^3}\Bigg\{&\lambda_1\left[\sin(2k) - 2k\cos(2k)\right] + \frac{3\eta_w\lambda_2}{k}\left[4k\sin(2k) + (2-4k^2)\cos(2k) - 2\right] \\ &+ \frac{\eta_w\lambda_1}{2k^3}\left[(-2k^4+6k^2-3)\cos(2k) + (4k^3-6k)\sin(2k) + 3\right]\Bigg\},\end{aligned} \tag{2.10}$$

with $\eta_w = \eta - \eta^2/16$, $\eta = 4\pi n/3$, $\lambda_1 = (1+2\eta_w)^2/(1-\eta_w)^4$, $\lambda_2 = -(1+\eta_w/2)^2/(1-\eta_w)^4$ and $\underline{d_w}^3/\eta_w = \underline{d}^3/\eta$. Finally, the sought correlation model $\mathscr{R}(r)$, which is a normalized auto-covariance, is directly related to the 2-point matrix probability function through the relation (see [250, Chapter 2]):

$$\mathscr{R}(r) = \frac{S_2(r) - (1-\eta_w)^2}{\eta_w(1-\eta_w)}. \tag{2.11}$$

The reason for normalizing is to remove the discontinuity at the origin, due to the fact that we are considering a correlation model for a discontinuous two-phase medium, and look for a correlation model of a continuous random field of Young's modulus. The variance will be identified in Section 2.2. Other, more complex theories describe the correlation pattern for polydisperse packings of sphere [259, 41, 40, 266, 67, 135, 250] and are expected to behave better at long distance, but have not been considered to date. The Meyer representation proposed by Quintanilla [190] for randomly oriented ellipsoids may be studied in future works. Theoretically, the Percus-Yevick approximation is not appropriate for dense arrays of particles, such as those that we are considering, but this approximation can be improved, in particular using the Verlet-Weis [256] or Kincaid-Weis [128] semi-empirical modifications to the Percus-Yevick radial distribution. In this work, we considered and used the modifications proposed by Verlet-Weis. This empirical correction tries to reduce, for large r, the main maximum of the structure factor, and the small difference in the phase in the radial distribution function. Finally, the correlation model of Eq. (2.11) is plotted in Fig. 2.5, for different volume fractions and diameters.

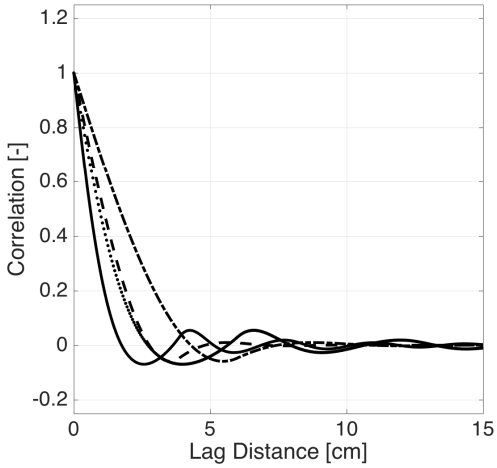

FIGURE 2.5: Correlation function for an impenetrable sphere packing with constant diameter $\underline{d}$ and volume ratio $\underline{\phi}$. Four cases were presented here: $\underline{d} = 3.9$ cm and $\underline{\phi} = 0.5682$ (solid line); $\underline{d} = 3.9$ cm and $\underline{\phi} = 0.2$ (dashed line); $\underline{d} = 6$ cm and $\underline{\phi} = 0.5682$ (dotted line); $\underline{d} = 6$ cm and $\underline{\phi} = 0.2$ (dash-dotted line).

2.1.4 First-order marginal law for Young's modulus

We now turn to the choice of the first-order marginal law. Young's modulus is a positive quantity, and the choice of first-order marginal law should reflect that physical requirement. We consider in this work two of these: (i) log-normal law, and (ii) Gamma law. Both models are parameterized by an average μ_E and variance σ_E^2. The probability density function of the log-normal distribution is:

$$p(E) = \frac{1}{Es\sqrt{2\pi}} \exp\left(-\frac{(\ln E - m)^2}{2s^2}\right) \tag{2.12}$$

where $s^2 = \ln(1+\sigma_E^2/\mu_E^2)$ and $m = \ln(\mu_E) - s^2/2$ are the variance and mean of the underlying Gaussian distribution. The probability densify function of the Gamma distribution is:

$$p(E) = \frac{E^{k-1}}{\Gamma(k)\theta^k} \exp\left(\frac{-E}{\theta}\right), \tag{2.13}$$

where $\theta = \sigma_E^2/\mu_E$ and $k = \mu_E^2/\sigma_E^2$ are the shape parameters of the Gamma distribution, and $\Gamma(k) = \int_0^{+\infty} t^{k-1}\exp(-t)dt$ is the Gamma function. An example of these two densities (for $\mu_E = 1$ N/m^2 and $\sigma_E^2 = 10\mu_E^2$) is plotted in Fig. 2.6. They mainly differ in the tails, that is to say for the description of very small and very large values. Note also that, as desired for a positive parameter, the support of both functions is limited to $\mathbb{R}^+$.

2.1.5 Generation of realizations of the stochastic field of Young's modulus

As realizations of the stochastic field of Young's modulus will be required for the numerical simulations in the next sections (cylindrical samples in Section 2.2), we conclude this section with a description of a numerical strategy for the generation of the samples. This can be performed in two different ways: either in the space or in the spectral domain. The latter is widely used for its simplicity and efficiency [230]. It consists in summing a large number of functions oscillating with random phases and with amplitudes designed to match the desired

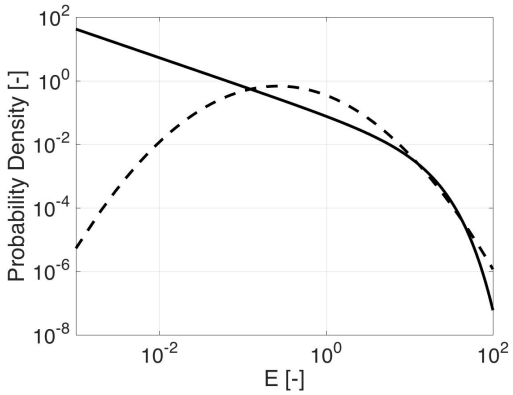

FIGURE 2.6: Probability density function for the Gamma distribution (solid line) and log-normal distribution (dashed line) for $\mu_E = 1$ N/m^2 and $\sigma_E^2 = 10\mu_E^2$.

correlation model:

$$E(x) = 2\sum_{j=1}^{N} \sqrt{\sigma_E^2 \hat{\mathscr{R}}(k_j)\Delta k}\,\zeta_j \cos(k_j x + \phi_j) \tag{2.14}$$

where the ζ_j are independent unit centered gaussian random variables, the ϕ_j are independent random variables, uniform over $[0, 2\pi]$, N in the number of terms in the sum, Δk is the discretization step in wave-number space, and $\hat{\mathscr{R}}(k_j)$ is the normalized power spectral density function in wave-number space, that is to say the Fourier transform of the normalized autocovariance introduced in Eq. (2.11). Although written here for simplicity in 1D, the extension to 3D is described in full details in [229]. This algorithm generates random fields that are asymptotically Gaussian and asymptotically ergodic, so that a Rosenblatt transformation [199] is then applied to obtain the desired first-order marginal density. Note that this pointwise transformation is known to modify in general the correlation structure [99, 186]. In Fig. 2.8, a comparison is proposed between the target correlation structure and the correlation structure estimated from one single realization of the Rosenblatt-transformed random field (generated for the cylinder of Section 2.2 and Fig. 2.7). As expected, a slight shift in the correlation length seems to be observed, but the shape remains quite unchanged. The influence of the correlation structure of the random field is discussed in more details in Section 2.3.3.

The efficiency of this technique mainly lies in the possibility to take advantage of the efficiency of the Fast Fourier Transform (FFT) algorithm in a straightforward way [230, 229]. However, when simulating realizations over large clusters of computers, as required in the simulation in Section 3.3, the algorithmic complexity of the FFT is too large. We therefore consider a particular implementation of the spectral representation method, which considers independent realizations (obtained with the scheme above) over each processor and overlap and merging to retrieve the continuity and correlation over the global domain. More details on this implementation can be found in [178]. One example of realization of random fields are proposed: a typical sample used in Section 2.2 is presented in Fig. 2.7.

2.2 Identification of the stochastic continuum model parameters

This section discusses the identification of the variance of the stochastic model of Young's modulus described in the previous section and the comparison with the model presented in Section 1.2. The reference for the identification is the distribution of equivalent stresses $p_r(\sigma_{zz})$ in the set of numerical granular samples described in Section 2.1.1.

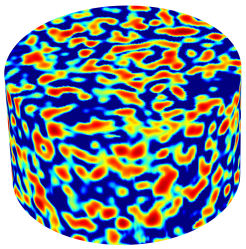

FIGURE 2.7: One realization of the random model of Young's modulus ($\underline{d} =$ 3.9 cm and $\underline{\phi} = 0.5830$) for a cylinder of the same size as in Fig. 2.1: radius R =35 cm and height H =39 cm.

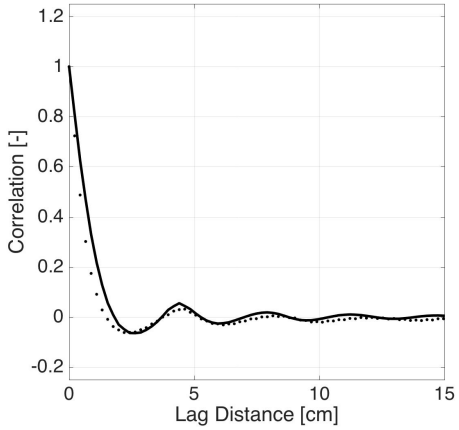

FIGURE 2.8: Comparison of the theoretical correlation model, used to generate the Gaussian random fields (solid line) and the correlation estimated from one cylindrical sample of the Rosenblatt-transformed random field (dotted line).

2.2.1 General methodology

Usually the identification process is made solving an optimization problem, where an objective function is maximized or minimized [36], Eq. 2.15 in our case. In this thesis we used the Nelder-Mead method or amoeba method [165]. It consists in an iterative zero order method, in other words, it does not depends of the sensibility matrix of the problem [207, 206]. The method uses a simplex (generalization of the notion of a triangle or tetrahedron to arbitrary dimensions) with $n+1$ vertices in a n dimension.

The algorithm starts with the definition of a non-degenerate simplex chosen in this space. By successive iterations, the process consists of determining the point of the simplex where the function is maximal in order to replace it by the reflection (that is to say the symmetrical) of this point with respect to the center of gravity of the remaining n vertices. If the value of the function at this new point is lower than the values taken at the other points, the simplex is stretched in that direction. Otherwise, it is assumed that the local shape of the function is a valley, and the simplex is reduced by a similarity centered on the point of the simplex where the function is minimal. This method is implemented in the function *fminsearch* [136] in Matlab® [153]

Identification process

The steps of the identification process are summarized in Fig. 2.9 and listed below:

1. an initial value of the variance is chosen;
2. a realization of a heterogeneous Young's modulus field is generated;
3. the distribution of stresses $p(\sigma_{zz})$ in the Finite Element model (described in Section 2.2.1 below) is computed;
4. the L^2 distance between that distribution and the reference is computed;

$$L_r = \int_{\Sigma} (p(\sigma_{zz}) - p_r(\sigma_{zz}))^2 d\sigma_{zz}. \tag{2.15}$$

   The interval $\Sigma \in \mathbb{R}$ is chosen so as to remove the tails of the experimental distribution, for which the data is too scarce to ensure statistical convergence. In this work, we have considered the interval $[1 \times 10^4 - 7 \times 10^6]$ N/m^2, which corresponds to 90% of the experimental probability density of σ_{zz};
5. depending on the distance obtained, and using a simplex algorithm [136], new values of the variance are proposed, and an iterative process is considered on steps 1-5. If convergence is not obtained, a new value of the variance is proposed and a new iteration starts at step 2; else the algorithm exits.

Note that in the entire process, only the variance evolves. The remaining parameters (average Young's modulus, correlation length and model, first-order marginal density), as well as the averaging volume for the reference distribution, are fixed. Note also that the Kullback-Leibler distance [18] has been tested instead of Eq. (2.15) and yielded the same qualitative results as those presented below.

Description of the continuum samples used for identification

The continuum samples that are used for the identification process imitate the discrete samples described in Section 2.1.1. They are cylinders of radius R =35 cm and height H =39 cm, loaded with an isotropic confinement pressure of 60 kPa on the lateral face and with a vertical pressure of 63 kN on the upper face. Gravity is also considered within the model. The generation of one realization of the random field and the simulation of the corresponding response took on average 4800 s of CPU time.

We consider a homogeneous density $\rho = 1574$ kg/m^3 (see Section 2.1.2) and a homogeneous Poisson ratio $\nu = 0.23$ [117]. As the identification process is driven by stress distribution, and because we are considering a linear model, the average Young's modulus is expected to be ill-constrained in this experiment. We therefore choose to fix its value at $\underline{E} = 80$ MPa [117], and will investigate this further in Section 2.3.4. The density and the Poisson ratio can be modelled as an heterogenous material. However, in the present case, we believe that this approach does not contribute significantly for the results. An imposed pressure was applied in the top of the sample (around 160 kPa). This pressure is much higher than the weight of the sample at the bottom layer (around 585 Pa). Due to this huge difference in the pressure we believe that the density does not play a major role in our analysis, moreover, the static analysis removes the inertia term of the equation. Regarding the Poisson's ratio we can state that a similar response can be obtained when comparing with Young's modulus. However, the Poisson's ratio can assume negative values and cannot be bigger than 0.5 (due to thermodynamic restrictions). This restriction should affect choice made for the first order marginal law (gamma law), in other words, a more suitable law should be studied.

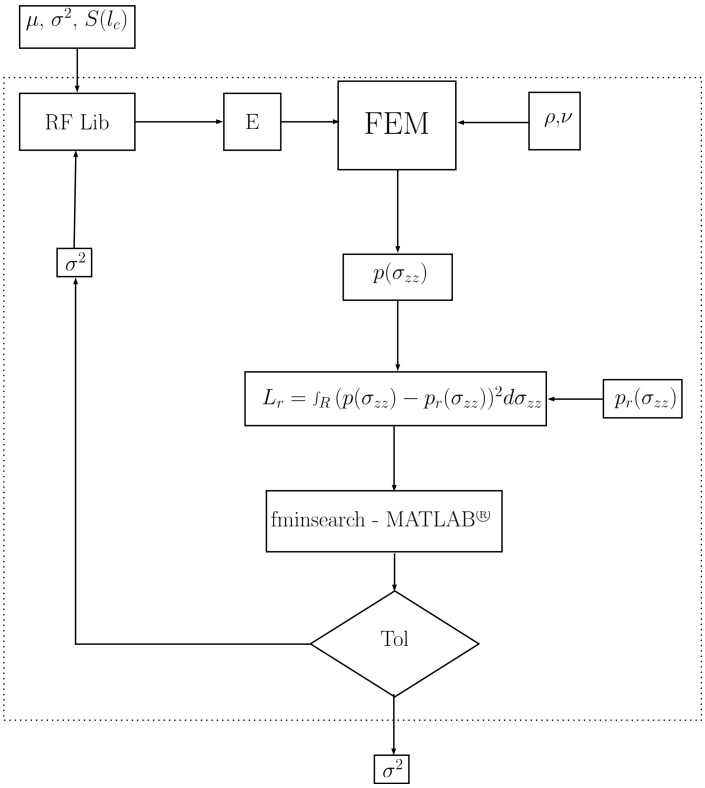

FIGURE 2.9: Optimization scheme.

All simulations are performed with the Finite Element Method (COMSOL software) with a mesh of close to 380'000 hexahedra, corresponding to elements of size $h \approx 0.7$ cm, linear elements ($p = 1$) were used, much smaller than the correlation length. To simplify the post-treatment process, note that output stresses are extracted only within a box of size $48 \times 48 \times 32$ $(\text{cm})^3$, inset into the cylinders. It was checked that there is no significant difference between the stress distribution within the box and within the full cylinder.

2.2.2 Identification for a Gamma first-order marginal with averaging volume $V = (4\ \textbf{cm})^3$

Considering a Gamma first-order marginal density, and the experimental distribution of equivalent stresses obtained with an averaging volume of $V = (4\text{cm})^3$, the optimization process leads to the evolution of the L^2 distance plotted in Fig. 2.10. Although there is variability between samples, there is clearly a minimum of the L^2 distance, with a normalized variance close to $\sigma_E^2/\underline{E}^2 \approx 11$. Note that the minimization was re-started several times to make sure that no bias resulted from sample-to-sample variability. In each restart the departure point changed randomly.

The distributions of continuum stresses are plotted in Fig. 2.11 (solid lines) and compared to the experimental equivalent stresses (dashed lines). The identified stress distributions match very well with the discrete ones, both for the σ_{zz} coefficient, which was used to drive the identification, and the other coefficients, that were not used in the identification. The only apparent deficiency of the model lies in a slightly higher value of the lower-than-average shear stresses in the identified continuum model with respect to the experimental ones. Note that, on each plot, there are actually several continuous lines, corresponding to different realizations of cylindrical samples with the same statistical parameters. This shows that a cylindrical sample is statistically representative for the distribution of stresses, because

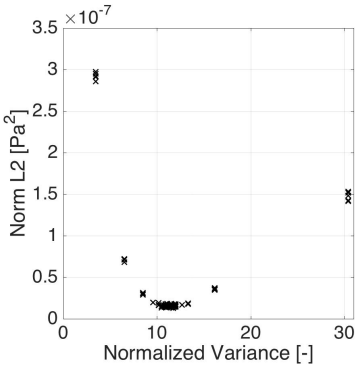

FIGURE 2.10: Evolution of the L^2 distance during the optimization process for a Gamma first-order marginal distribution and averaging volume $V = (4\text{ cm})^3$ as a function of the normalized variance $\sigma_E^2/\underline{E}^2$.

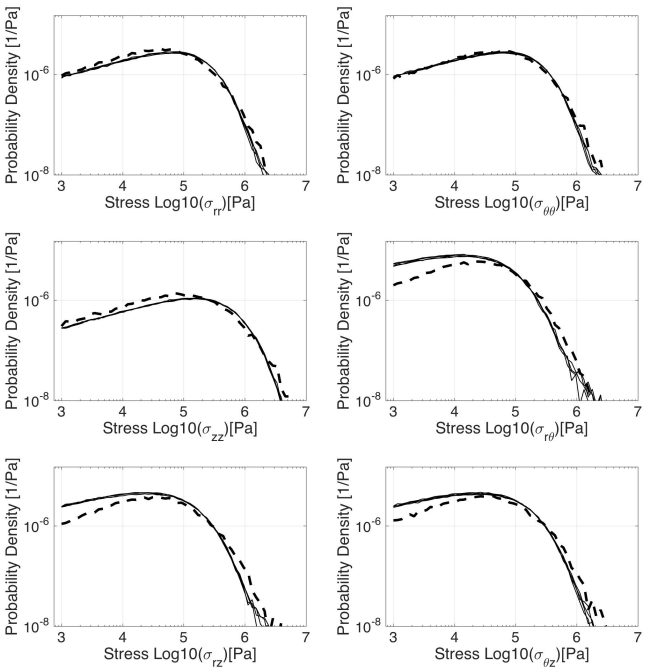

FIGURE 2.11: Distribution of the logarithm of the equivalent stresses for the discrete samples and averaging volume $V = (4\text{ cm})^3$ (dashed line), and for the identified continuum model with Gamma first-order marginal density (solid line).

there is almost no variability in the stress distribution from sample to sample, although there is a large variability in the pointwise values of the Young's modulus.

2.3 Influence of the model parameters in the equivalent stress distribution

In this section, we study in details the influence of several model parameters (averaging volumes, first-order marginal density, correlation model, and mean value of the stochastic field) on the identification process of the equivalent stress distribution.

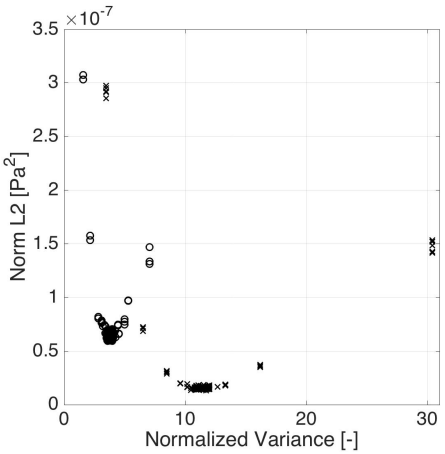

FIGURE 2.12: Evolution of the L^2 distance during the optimization process for a Gamma first-order marginal distribution and different averaging volumes: $V = (4\text{ cm})^3$ (crosses), and $V = (8\text{ cm})^3$ (circles), as a function of the normalized variance $\sigma_E^2/\underline{E}^2$.

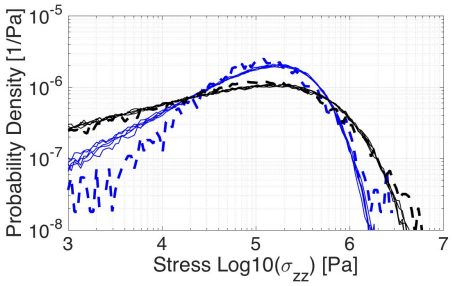

FIGURE 2.13: Distribution of the logarithm of the vertical equivalent stresses, σ_{zz} for the discrete samples (dashed lines) and for the identified continuum models with Gamma first-order marginal density (solid lines), for averaging volumes $V = (4\text{ cm})^3$ (black lines) and $V = (8\text{ cm})^3$ (blue lines).

2.3.1 Comparision of Gamma models for different averaging volumes

Still considering the Gamma first-order marginal density, we now consider a different averaging volume $V = (8\text{ cm})^3$ and compare it to the previous volume $V = (4\text{ cm})^3$. The optimization process produced the results plotted in Fig. 2.12. A clear reduction of the normalized variance can be observed, from $\sigma_E^2/\underline{E}^2 \approx 11$ for $V = (4\text{ cm})^3$ to $\sigma_E^2/\underline{E}^2 \approx 4$ for $V = (8\text{ cm})^3$ compared to the variance for $V = (4\text{ cm})^3$. Note that we do not consider here the identification for the averaging volume $V = (2\text{ cm})^3$ because the generation of random fields with Gamma first-order marginal densities and normalized variances larger than 26 resulted in numerical issues. This is linked to the inversion of the Gamma cumulative function in the Rosenblatt transform.

The obtained distributions of identified continuum stresses (σ_{zz} component) are plotted in Fig. 2.13 and compared to the experimental equivalent stresses. The variance reduction is clearly visible. The agreement between both groups of curves is very good, although less for the larger average volume, where the lower-than-averages forces are slightly overestimated. However, it should be noted that they correspond to very low probability of occurence (two orders of magnitude below the maximum), so that a larger experimental database might be desirable.

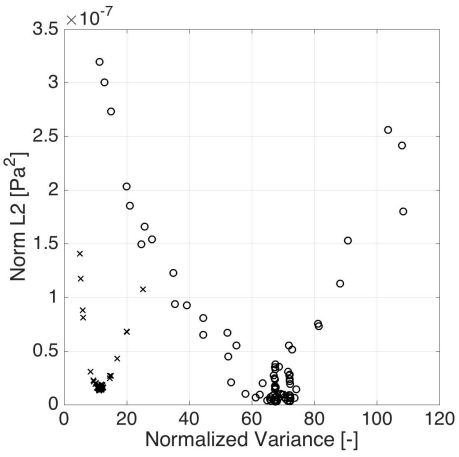

FIGURE 2.14: Evolution of the L^2 distance during the optimization process at $V = (4\text{ cm})^3$ as a function of the normalized variance $\sigma_E^2/\underline{E}^2$, for a Gamma (crosses) and log-normal (circles) first-order marginal distribution.

2.3.2 Influence of the first-order marginal density

Considering the averaging volume of $V = (4\text{ cm})^3$, we now consider a log-normal first-order marginal density, and compare the results obtained with those of the Gamma first-order marginal density (Section 2.2.2). The optimization process leads to the convergence presented in Fig. 2.14. It can be seen that the variance corresponding to the log-normal density is much larger than before: $\sigma_E^2/\underline{E}^2 \approx 72$. It is also interesting to remark that there is much more variability in the L^2 distance depending on the particular realization of cylindrical sample that is considered.

The stress distributions are then plotted in Fig. 2.15. Although the distribution for the σ_{zz} coefficient matches relatively well the experimental equivalent stress, as expected out of the optimization process, all the other coefficient are rather badly approximated. This is probably due to the very large difference between the log-normal and Gamma distributions for the tails of the distribution (see Fig. 2.6). The log-normal first-order marginal density can therefore not be considered as appropriate to model Young's modulus in the ballast.

2.3.3 Influence of the correlation model

To consider the influence of the correlation model in the identification process, we compared the model presented in Sec. 2.1.3 with a cardinal sine correlation model [238, 245]. The optimization process leads to the convergence presented in Fig. 2.16. A remarkable influence of the departure point on the values at convergence was observed. Indeed, when the departure point was lower than about 10 ($\sigma_E^2/\underline{E}^2 \approx 10$), the results were quite consistent, and the minimum was found close to $\sigma_E^2/\underline{E}^2 \approx 5$. However, when the initial point was larger than 10, the convergence process became stuck in local minima (see the square markers in Fig. 2.16). Note that the normalized variance found in this case is quite different from the value found in Sec. 2.2.2 for the same volume and first-order marginal law.

The stress distributions are then plotted in Fig. 2.17. The distribution for the σ_{zz} around and above the mean value is quite satisfactory, except for one realization of the optimization process. The lower-than-average stresses are however poorly represented. For all other components of the stress tensor, both the below-than-average and above-average stresses are badly represented. Finally, note that the realization with a departure point larger than 10 presents stress distributions whose shapes are completely different from the granular ones.

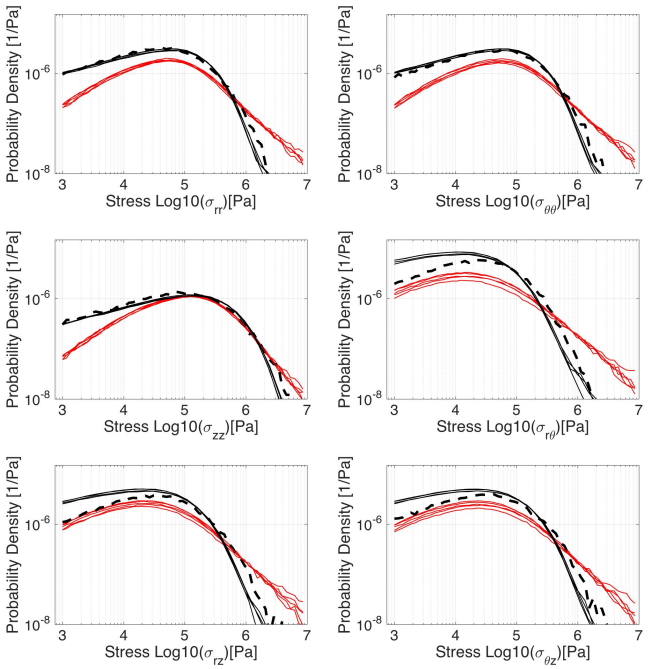

FIGURE 2.15: Distribution of the logarithm of the equivalent stresses for the discrete samples and averaging volume $V = (4\text{ cm})^3$ (black dashed line), for the identified continuum model with Gamma first-order marginal density (black solid line), and for the identified continuum model with Log-normal first-order marginal density (red solid line).

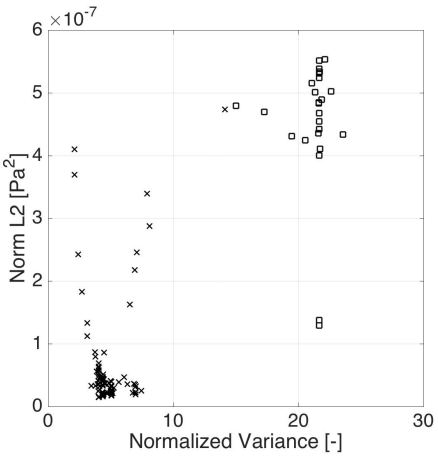

FIGURE 2.16: Evolution of the L^2 distance during the optimization process at $V = (4\text{ cm})^3$ as a function of the normalized variance $\sigma_E^2/\underline{E}^2$. The crosses represents the realizations where the departure point, for the optimization process, were below 10, $\sigma_E^2/\underline{E}^2 \leq 10$. The squares represent the realization where the departure point was greater than 10, $\sigma_E^2/\underline{E}^2 \geq 10$.

2.3.4 Influence of the average of Young's modulus

Finally, we consider a different average Young's modulus and compare the results to the case in Section 2.2.2. Fig. 2.18 presents the convergence of the L^2 distance for $\underline{E} = 80$ MPa (with

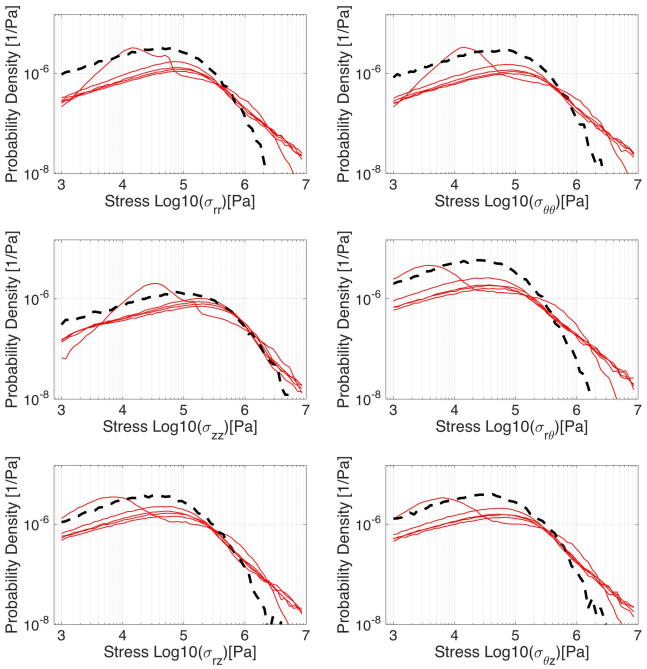

FIGURE 2.17: Distribution of the logarithm of the equivalent stresses for the discrete samples and averaging volume $V = (4\text{ cm})^3$ (black dashed line), for the identified continuum models with Gamma first-order marginal density and cardinal sine correlation model (red solid lines).

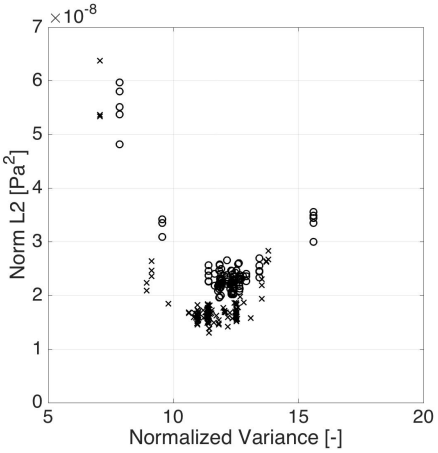

FIGURE 2.18: Evolution of the L^2 distance during the optimization process for a Gamma first-order marginal distribution at $V = (4\text{ cm})^3$ and $\underline{E} = 80$ MPa (crosses), and for $V = (4\text{ cm})^3$ and $\underline{E} = 800$ MPa (circles), as a function of the normalized variance $\sigma_E^2/\underline{E}^2$.

crosses) and $\underline{E} = 800$ MPa (with circles). It is clear from the orders of magnitude of the L^2 distance (compared to the previous figures) that the average Young's modulus has very little influence on the identification. This was to be expected because the identification is performed on stress distributions rather than on kinematical quantities. The stress distributions are not plotted because they almost overlap in the two cases.

2.4 Concluding remarks

In this chapter, we introduced a novel approach to the modelling of granular materials (ballast grains) for ballasted railway tracks. In between homogeneous continuum models, that cannot reproduce the complex dynamical behaviour of realistic tracks, and discrete models that are difficult to simulate at the appropriate scale, we proposed a heterogeneous continuum model. Young's modulus was modelled as a randomly-fluctuating parameter whose statistics have been identified on discrete simulations of granular samples with realistic shapes. The stress distributions match extremely well the equivalent stresses in the discrete simulations, even for components that have not been used in the identification process. The variance depends on the averaging volume for the equivalent stresses and has been identified as close to $\sigma_E^2/\underline{E}^2 \approx 11$ for $V = (4\text{ cm})^3$. As expected, the average is not well constrained by the chosen experimental data.

In terms of limitations of the model, it should be stressed that the model can obviously not take into account situations when grains re-arrange. It is therefore not appropriate for fatigue simulations or long-term behaviour of the track. Also, it considers locally averaged stresses and strains, so that it is probably not appropriate to predict local stress states, sometimes required for fatigue simulation at the interface with the sleepers for instance [116].

It will be interesting to discuss in detail the impact of the heterogeneity on wave propagation, as this feature is classically observed in wave propagation in granular media. This study was presented in the Chapter 3.

Chapter 3

Wave propagation in a highly heterogeneous medium

Dispersion curves are among the most classical tools used in the analysis of wave propagation. These curves link the values of (k, ω) for which the dispersion relation vanishes and represent the values for which a plane wave can actually propagate in the medium in a given direction. These simple 2D diagrams allow a quick understanding of the properties of the wave propagation medium. In a linear elastic isotropic unbounded medium, the dispersion curves are two straight lines, for the pressure and shear waves, respectively. Lord Rayleigh developed the dispersion relation for elastic half-spaces, discovering the Rayleigh wave [196]. The dispersion equation for a plate was solved by Sir Horace Lamb [139], displaying an infinite number of modes, most of them dispersive. The objective of this chapter is, therefore, to construct numerically the dispersion curves for a randomly heterogeneous continuum model of a ballasted railway track.

Preliminaries results suggest that the Anderson localization phenomena can occur in a highly heterogeneous media, as presented in Section 3.1. Dispersion curves for the ballast were constructed (Section 3.3 using the methodology presented in Section 3.2) and a discussion on the relevant physical phenomena, including Anderson localization, was made. Additional simulations (Section 3.4) will be performed in generic granular media to confirm that the trapping of waves observed at higher frequencies (over 100 Hz) is indeed Anderson localization and not some effect of waveguide or impedance mismatch between the soil and the ballast.

3.1 Dynamic simulation of the passage of a train on a ballasted railway track

In this section, we consider the stochastic model of Young's modulus developed in the previous chapter and analyze the impact of the heterogeneity it models on a dynamic simulation of the passage of a train on a ballasted railway track. This simulation is not realistic because there is no dissipation involved. However, we believe it illustrates very clearly the importance of considering heterogeneity in the numerical modelling of granular media.

3.1.1 Description of the numerical model of the ballast

We consider the model depicted in Fig. 3.1. It is a 38 m-long one-way track segment, with a ballast (in yellow on Fig. 3.1) of height 48 cm and width between 3.9 m at the top and 5 m at the bottom. Below the track, the soil is numerically modeled on a width of 20 m and a depth of 5 m. The concrete sleepers have dimensions $20\times30\times200$ cm^3, are separated by $d = 0.6$ m, and are embedded on the ballast layer on a height of 10 cm. This simple setup is representative of a realistic ballasted railway track.

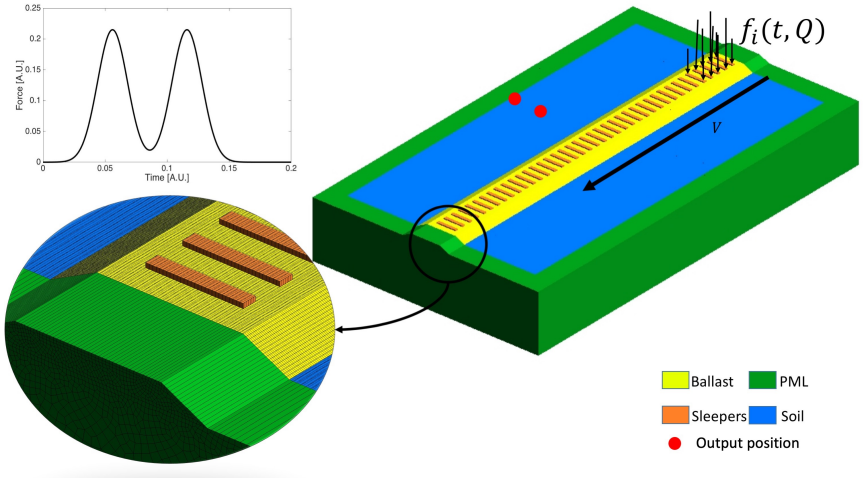

FIGURE 3.1: Geometry, loading, boundary conditions and mesh for the wave propagation analysis.

In the simulated domain, the wave field is the solution of the wave equation:

$$\nabla \cdot \sigma - \rho \ddot{\mathbf{u}} = \mathbf{0} \tag{3.1}$$

where the material is assumed isotropic and linear, so that the strain is $\varepsilon = (\nabla \mathbf{u} + \nabla \mathbf{u}^T)/2$ and the stress is $\sigma = \lambda(\mathbf{x})\mathrm{Tr}\varepsilon\mathbb{I} + 2\mu(\mathbf{x})\varepsilon$, with λ and μ the Lamé parameters, and $\mathbb{I}$ is the identity second-order tensor. The density is denoted ρ. The Lamé parameters are related to the wave velocities through $V_p = \sqrt{(\lambda + 2\mu)/\rho}$ and $V_s = \sqrt{\mu/\rho}$. The problem is closed with boundary and initial conditions. For instance, in an unbounded medium, the Sommerfeld radiation conditions state:

$$\lim_{r\to\infty} r\left(\frac{\partial \mathbf{u}}{\partial r} - ik\mathbf{u}\right) = 0, \tag{3.2}$$

where $r = \|\mathbf{x}\|$.

The soil is assumed homogeneous in all simulations, with $V_s = 180$ m/s, $V_p = 350$ m/s, and $\rho = 1900$ kg/m^3. The concrete sleepers are assumed homogeneous in all simulations, with $V_s = 2500$ m/s, $V_p = 4500$ m/s, and $\rho = 2400$ kg/m^3. In the simulations where the ballast is assumed homogeneous, we consider $V_s = 150$ m/s, $V_p = 380$ m/s, and $\rho = 1570$ kg/m^3. In the simulations where the ballast is assumed heterogeneous, the random model of mechanical properties is the one described in the previous chapter, and the average values are taken equal to those of the homogeneous case.

The vertical loading considered is a classical one for modeling the influence of a train-rail system (one bogie) on the sleepers [100]. It considers the flexibility of the rail by transferring the point loads of the boggie of a train onto consecutive sleepers. The movement of the train is taken into account by moving the position of the point loads at the appropriate velocity. The loading on each of the sleepers (and on each side of each sleepers, as indicated on Fig. 3.1) is given by:

$$F_i(t) = \frac{QY}{2}\left[C^{\frac{(v_0(t-\delta_i)-a)^2}{d^2}} + C^{\frac{(v_0(t-\delta_i)-a-L)^2}{d^2}}\right] \tag{3.3}$$

where Q is the load magnitude, $L = 3$ m is the wheelbase, $d = 0.6$ m is the distance between two consecutive sleepers, $a = 3 = 5d$ m is the critical distance, beyond which the load is assumed to vanish, $v_0 = 100$ m/s is the chosen train velocity, and $C = 0.61$ and $Y = 0.41$ are constants that depend of the soil-ballast combination. The latter values are obtained from the experimental values in [9]. In order to produce a “moving load" each sleeper i is associated

with a time delay δ_i. The Fig. 3.1 highlights the region where the vertical point loads are applied at the top of the sleepers at the initial time. The transmission of the point load to the ballast layer takes place through the sleepers. Only five sleepers are loaded in the image because the influence of the boggie on further sleepers almost vanishes.

In the inset of Fig. 3.1, the refinement of the mesh is also shown. The mesh is discretized with 0.81 millions of hexahedral elements. High-order polynomials of order 7 are used in the spectral element solver (see Section 3.1.2), which corresponds to 343 degrees of freedoms (DOFs) for each element, and a total of close to 175 millions of DOFs for the entire mesh. On the exterior of the soil box (green area in Fig. 3.1), a Perfectly Matched Layer (PML) [88] is added to absorb outgoing waves and mimic the Sommerfeld boundary condition. The PML implementation is based on the interpretation of the second-order Newmark scheme as a time-staggered velocity-stress algorithm. Using additional variables to the equations [35] the variables can be split in two, kinematic and dynamic fields are separated into unphysical components and finally, the equations can be written in the time domain [87]. It avoids frequency dependence in the problem (avoiding convolution calculation).

3.1.2 Spectral Element solver

In this chapter, Eq. (3.1) is approximated with the Spectral Element Method. The SEM is a high-order Finite Element Method that uses Gauss-Lobatto-Legendre (GLL) quadrature rule and Lagrange polynomials based on the nodes of that same quadrature. This ensures that the mass matrix is diagonal and allows to use explicit time integration schemes and very efficient parallelization (for a complete description of the method, see for instance [62], as well as the original papers [149, 38]). The space discretization of the variational form of the wave propagation Eq. (3.1) gives:

$$\mathbf{M}\dot{\mathbf{V}} = \mathbf{F}^{\mathbf{ext}} - \mathbf{F}^{\mathbf{int}}(\mathbf{U},\mathbf{V}) \tag{3.4}$$

where $\mathbf{U}$ and $\mathbf{V}$ are vectors containing the components of the displacement and velocity at the nodes, $\mathbf{M}$ is the (diagonal) mass matrix, and the vectors $\mathbf{F}^{\mathbf{ext}}$ and $\mathbf{F}^{\mathbf{int}}$ are vectors of external loads and internal forces. Using an explicit second-order finite-difference scheme in time leads to:

$$\frac{1}{\Delta t}\mathbf{M}\left[\mathbf{V_{n+1}} - \mathbf{V_n}\right] = \mathbf{F}^{\mathbf{ext}}_{\mathbf{n+1/2}} - \mathbf{F}^{\mathbf{int}}(\mathbf{U_{n+1/2}}, \mathbf{V_{n+1/2}}), \tag{3.5}$$

$$\mathbf{U_{n+1}} = \mathbf{U_n} + \frac{1}{2\Delta t}\left[\mathbf{V_n} + \mathbf{V_{n+1}}\right], \tag{3.6}$$

$$\mathbf{A_{n+1}} = \frac{1}{\Delta t}\left[\mathbf{V_{n+1}} - \mathbf{V_n}\right], \tag{3.7}$$

where $\mathbf{U_{n+1/2}} = (\mathbf{U_{n+1}} + \mathbf{U_n})/2$ and $\mathbf{F}^{\mathbf{ext}}_{\mathbf{n+1/2}} = (\mathbf{F}^{\mathbf{ext}}_{\mathbf{n+1}} + \mathbf{F}^{\mathbf{ext}}_{\mathbf{n}})/2$. Even though the stability condition requires to use very small time steps [62, 225, 65], the construction of the solution at each time step is very cheap because the inversion of the mass matrix is instantaneous. Our implementation of the SEM has demonstrated scalability for more than 10'000 cores [101] while other implementations in the literature have even been shown to scale over 100'000 cores [130]. Our implementation uses hexahedral non-structured meshes and Perfectly Matched Layers (PML) to account for unbounded domains [88]. All simulations presented in this thesis were ran at Moulon Mesocentre facility in France, jointly run by CentraleSupélec and ENS Paris-Saclay. The cluster uses Intel Xeon processors E5-2670 v3 @ 2.30 GHz (Haswell).

3.1.3 Influence of heterogeneity on the wave field

This section discusses the wave fields induced in the ballast-soil system by the passage of a train, using the numerical method of Section 3.1.2 and model of Section 3.1.1. As explained earlier, we consider two different models, and compare them. The models are similar in all features except for the mechanical parameters in the ballast layer: one of the model has homogeneous properties in the ballast, while the other is heterogeneous. Note that the average value of the heterogeneous mechanical property is equal to the value of the homogeneous one. Note also that the input force is normalized *a posteriori* in order to make sure that the total energy introduced in the two models is the same.

The normalized displacement field at time $t = 0.27$ s in the case when the ballast is homogeneous is plotted at the upper part of Fig. 3.2. The pattern is quite simple, with an energy clearly concentrated under the moving load. Most of the displacement seems to be concentrated in the ballast layer, with rapid decrease both in depth and at distance from the track. There seems to be mainly a guided wave within the ballast layer, connecting with Rayleigh wave in the soil. At the lower part of Fig. 3.2, the same displacement field is plotted in the case of the heterogeneous ballast. The wave pattern is very different, with most of the energy remaining within the ballast, and not necessarily concentrated below the moving load. The energy seems to be trapped within the ballast layer, but not moving forward as in the case of guided waves. Overall, the energy radiated in the soil seems to be smaller.

This last statement is confirmed by the times histories at the output positions marked in Fig. 3.1 and plotted in Fig. 3.3. Indeed, the maximum values of the displacement field are larger with a homogeneous ballast than with a heterogeneous one. On the other hand, after some time, the tendency is inverted. As most of the energy in the homogeneous case remains concentrated on a single front, once that front has passed, there is little energy remaining in the system. For a heterogeneous ballast, the energy initially trapped in the ballast keeps on sending waves into the soil for a longer time. Note that there is no energy dissipation in our model, so that the later part of the recordings is probably not very realistic. Within an actual ballast, a large part of the energy trapped in the ballast layer would be dissipated by friction and crushing of grains. To incorporate this dissipation in a generalized model requires developing a continuum dissipation model adequate for granular materials, with parameters homogeneous in space or not [121]. Even though there is no dissipation, the output positions located in the free field would still feel apparent damping because most of the energy does not escape the ballast, resulting in smaller displacements of those output positions.

The fact that the two images Fig. 3.2 and Fig. 3.3 are so different is a clear demonstration that heterogeneity in the ballast should be taken into account. Indeed, the results obtained here can be shown to be much more compatible with actual observations made in the field [69] than previous models.

3.2 Construction of the dispersion curve using numerical solutions in time-space

In this section, we present a methodology to obtain dispersion curves using numerical solutions of the wave equation in space-time.

3.2.1 Definition of dispersion curves

Assuming that the displacement field in Eq. (3.1) is expressed as a monochromatic plane wave: $\mathbf{u} = \tilde{\mathbf{u}} \exp i(\mathbf{k}\cdot\mathbf{x} - \omega t)$, where ω is the angular frequency, $\mathbf{k}$ the wave number and $\tilde{\mathbf{u}}$ the amplitude vector, we obtain:

$$(\Gamma(\mathbf{k}) - \rho\omega^2\mathbb{I})\tilde{\mathbf{u}} = \mathbf{0} \tag{3.8}$$

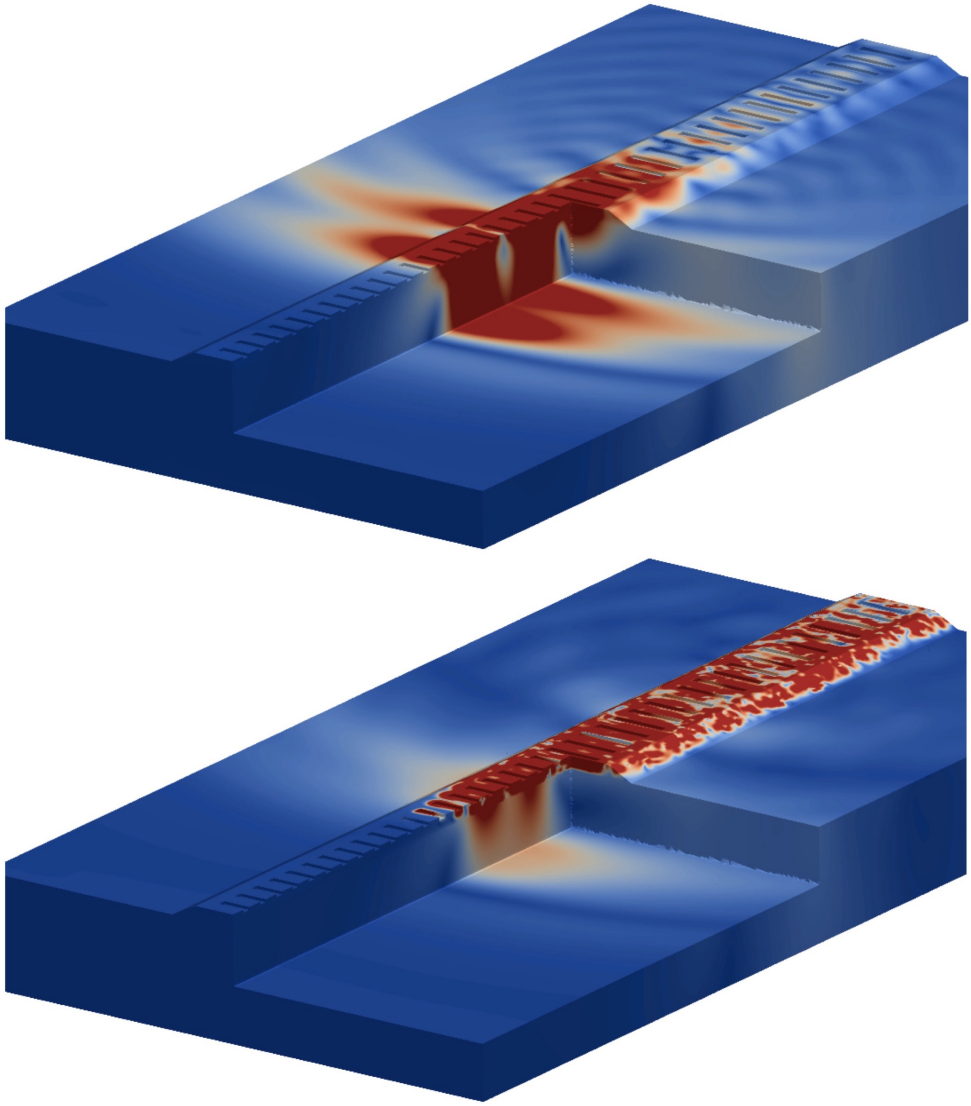

FIGURE 3.2: Displacement fields at time $t = 0.27$ s. The upper figure corresponds to the simulation with homogeneous ballast, while the lower one corresponds to simulation with heterogeneous ballast.

where $\Gamma(\mathbf{k}) = (\lambda+\mu)\mathbf{k}\otimes\mathbf{k} - i(\nabla\lambda\otimes\mathbf{k} + \mathbf{k}\otimes\nabla\mu) + (\mu|\mathbf{k}|^2 - i\mathbf{k}\cdot\nabla\mu)$ is Christoffel tensor. The dispersion equations are defined as $\det(\Gamma(\mathbf{k}) - \rho\omega^2\mathbb{I}) = 0$ and indicate the $(\mathbf{k},\omega)$ pairs that allow the existence of non-vanishing solutions of the wave equation. The values of $\mathbf{k}$ can be real, complex or imaginary. With the convention used here (as in [20, 21]), the real values correspond to propagative modes, pure imaginary values refer to evanescent modes, and complex values correspond to propagative modes with attenuation. For an elastic, isotropic and homogeneous medium, the propagative solutions are such that $\omega = V_p|\mathbf{k}|$ or $\omega = V_s|\mathbf{k}|$. In the latter case, two different polarizations (direction of vector $\tilde{\mathbf{u}}$) exist. For most other media, dispersion relations have to be computed numerically [137, 129].

3.2.2 General methodology to obtain dispersion curves using time-space data

A first approach consists in diagonalizing directly the Christoffel tensor, when available. In this paper, because the problem is too large, we rather use a methodology based on a 2D Fourier transform of numerical approximations of Eq. (3.1) to obtain an approximation of the pairs $(\mathbf{k},\omega)$ that satisfy the dispersion relation [11, 120, 171]. The general methodology

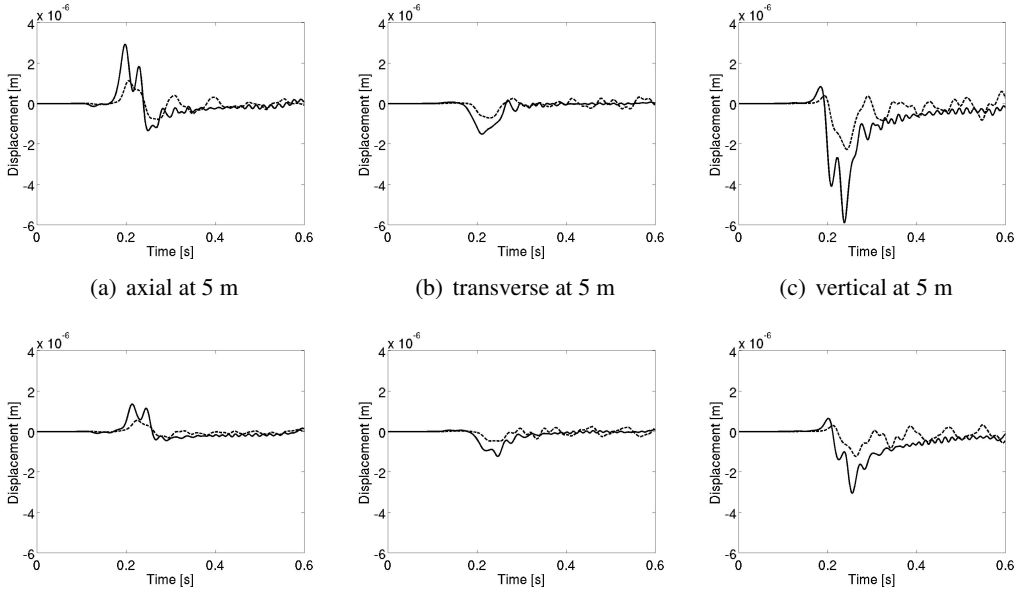

(a) axial at 5 m (b) transverse at 5 m (c) vertical at 5 m

(d) axial at 10 m (e) transverse at 10 m (f) vertical at 10 m

FIGURE 3.3: Displacements at the two output positions, located at 5 m and 10 m from the track (see Fig. 3.1 for the exact position). The solid lines correspond to the simulation with homogeneous ballast, while the dashed ones correspond to simulation with heterogeneous ballast.

to construct the dispersion relation consists in computing a displacement field, $\mathbf{u}(\mathbf{x},t)$ and performing Fourier transforms in both the time and space domains to obtain a 2D-variate function $\mathbf{H}_{\hat{\mathbf{k}}}(k,\omega)$ in a specific direction $\hat{\mathbf{k}} = \mathbf{k}/k$ with $k = \|\mathbf{k}\|$:

$$\mathbf{H}_{\hat{\mathbf{k}}}(k,\omega) = \int_{-\infty}^{+\infty} \int_{-\infty}^{+\infty} \mathbf{u}(\mathbf{x},t) e^{-i(\mathbf{k}\cdot\mathbf{x}+\omega t)} dx_k dt. \tag{3.9}$$

Note that $x_k = \mathbf{x}\cdot\hat{\mathbf{k}}$ represents the coordinate of the space position along the selected direction. The locations in (k,ω) where the amplitude $\|\mathbf{H}_{\hat{\mathbf{k}}}(k,\omega)\|$ is large match the dispersion equation [11]. Note that advantage is taken of the property of the method to resolve multimodal signals (more than one wave mode in the same time signal).

In order to compute an approximation of Eq. (3.9), we use $\mathbf{u}(\mathbf{x},t)$ estimated in positions $\{\mathbf{x}_m\}_{1\le m\le M}$ and aligned along direction $\hat{\mathbf{k}}$, and record the quantity of interest in those output positions at different time steps $\{t_n\}_{1\le n\le N}$. Assuming that the output positions are uniformly distributed along a segment of length L, and that the time instants are uniformly distributed in an interval of length T, we obtain the following map:

$$H_{pq} = \left| \sum_{m=1}^{M} \sum_{n=1}^{N} w(\mathbf{x}_m\cdot\hat{\mathbf{k}},t_n)\mathbf{u}(\mathbf{x}_m,t_n) e^{-2\pi i\left(\frac{pm}{M}+\frac{qn}{N}\right)} \right| = \left|\mathrm{FFT}_{2\mathrm{D}}[w(\mathbf{x}_m\cdot\hat{\mathbf{k}},t_n)\mathbf{u}(\mathbf{x}_m,t_n)]\right| \tag{3.10}$$

where $p = \mathbf{k}L$ is the normalizedwave-number and $q = fT$ is the normalized frequency. To avoid the presence of side lobes and reduce leakage, a bi-dimensional Tukey (tapered cosine) window function $w(x_k,t)$ was applied [105, 170].

In many examples described in this paper, the maps cited above are computed as averages of such functions using P lines of output positions, and N_{MC} realizations of the random medium (to be discussed later). In that case, the formulas above are computed for each line and each realization independently, and the average is computed dividing by $P \times N_{\mathrm{MC}}$.

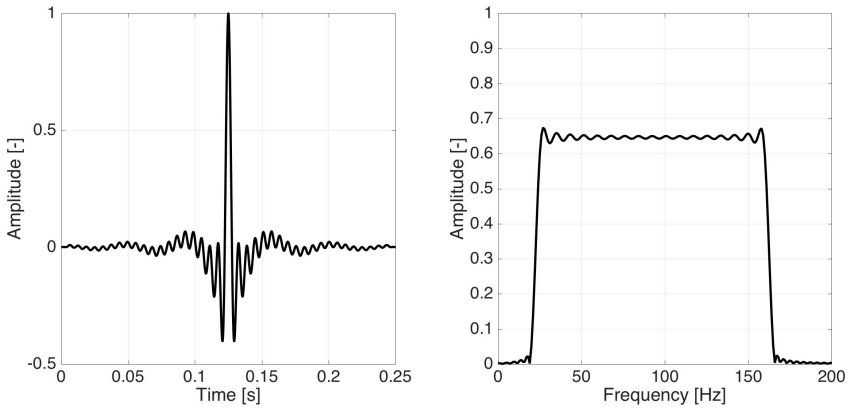

FIGURE 3.4: Amplitude (in time and frequency) of the load used in Section 3.2.3 (Ormsby function).

Also note that the source used for the construction of the maps has a very flat spectrum so the solution $\mathbf{u}(x,t)$ can be used directly. However, all results will be de-convolved (actually normalized by the source in the Fourier space of frequencies) before computing the maps.

3.2.3 Verification of the methodology in the unbounded isotropic case

This last part of the section is devoted to a verification of the methodology introduced in Section 3.2.2 in the isotropic case, for which the dispersion curve is known. We therefore consider a cube with side $L = 5\lambda_{max} = 50$ m, where λ_{max} is the longest wavelength in the model. The mesh is composed of hexahedral elements with side $\lambda_{min}/2 = 0.3125$ m. Each element uses 4th-order Lagrange polynomials in each direction, for a total of 375 degrees of freedom per element and 4096000 elements in the mesh. On all sides, 5 layers of PMLs with total thickness $0.255\lambda_{max}$ and power degree in the PML equal to $p = 3$ (not the discretization of the spatial domain) and amplitude equal to 9.87 were added to absorb outgoing waves and mimic an unbounded domain [75]. The mechanical properties are $V_p = 200$ m/s, $V_s = 100$ m/s, and $\rho = 1450$ kg/m^3. The model required around 140 h of CPU time on 144 processors.

A point force polarized in the x direction, is positioned at $[1,1,1]\lambda_{max}$. Its amplitude is given by an Ormsby function (see Fig 3.4):

$$A(t) = \left[\frac{(\pi f_4 \operatorname{sinc}(\pi f_4 t))^2}{\pi(f_4 - f_3)} - \frac{(\pi f_3 \operatorname{sinc}(\pi f_3 t))^2}{\pi(f_4 - f_3)}\right] - \left[\frac{(\pi f_2 \operatorname{sinc}(\pi f_2 t))^2}{\pi(f_2 - f_1)} - \frac{(\pi f_1 \operatorname{sinc}(\pi f_1 t))^2}{\pi(f_2 - f_1)}\right]. \quad (3.11)$$

with (for the example treated here) $f_1 = 20$ Hz, $f_2 = 25$ Hz, $f_3 = 160$ Hz, and $f_4 = 165$ Hz. This function displays a quasi-plane spectrum between frequencies f_2 and f_3, with a low-cut frequency f_1 and a high-cut frequency f_4.

In order to evaluate the Eq. 3.10, output positions are placed along different lines and record the displacement field. Three groups of 5 lines of output positions were placed aligned with the cube axes. Each line has a total length of $3.5\lambda_{max}$, with separation between output positions equal to $\lambda_{min}/10$. Finally, the distance between two parallel lines is $\lambda_{min}/2$. The general setting of output positions is represented on Fig. 3.5.

Fig. 3.6 presents the time history in the domain (PML is not represented). There are no apparent reflection coming out of the PML. We can clearly see the P and S waves with

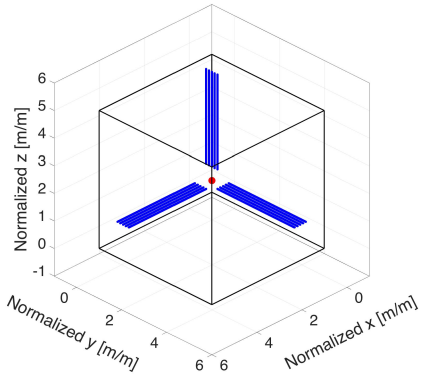

FIGURE 3.5: Output positions (blue lines), the red dot is the source position, the 15 lines are presented here, 5 in each direction lying in the source plane. The exterior cube represent the numerical domain used to simulate the unbounded domain.

different velocities. The P wave, faster then the S wave, presents large amplitudes along the x-axis and vanishing amplitude along the y and z axes. This is due to the polarization of the source along the x-axis. As the P-wave is a pressure wave, it is indeed strongly excited by the source. On the other hand, such a source does not generate pressure perpendicular to its polarization. For the S-wave, the opposite is logically observed, with large amplitudes along the y and z axes and vanishing amplitude along the x-axis. The color scale represented in the each snapshot was calculated dividing all the displacement magnitude field by the maximum displacement magnitude value after the application of the source in the model, in this case after 0.25 s.

Fig. 3.7 displays the dispersion curves obtained through the methodology of Section 3.2.2 using displacements obtained in the setting above. The colors indicate the values of $||H_{pq}||$ in decibels. There is clearly an excellent agreement between the values obtained using the proposed methodology and the analytical values of the dispersion curves. Because of the polarization of the source, the P-wave dispersion curve is only observed in the output positions aligned along the x-axis, while the S-wave dispersion curves are observed in the other two directions.

3.3 Dynamic behavior of a ballasted railway track

In this section, we now present the construction of the dispersion curves for a ballasted railway track. First, the model is set. Then, we provide some snapshots of the solution in time and analyze them. Finally, the construction of the dispersion curve itself is presented and discussed.

3.3.1 Randomly heterogeneous continuum model of a ballasted railway track

The ballasted railway track is modeled over a length of 84.375 m as an elastic half-space topped by a wedge-shaped structure, whose geometry is invariant along one direction (see Fig. 3.9). The geometry of the ballasted railway track was taken from [117]. The structure represents the ballast while the elastic half-space represents the soil that supports it. The soil is modeled as a bounded box with the following properties: $V_s = 180$ m/s, $V_p = 1100$ m/s, and $\rho = 1900$ kg/m^3 (see further down for the description of the ballast). The box of soil is surrounded on five sides by a layer of PMLs, that allow the wave to exit the box with little

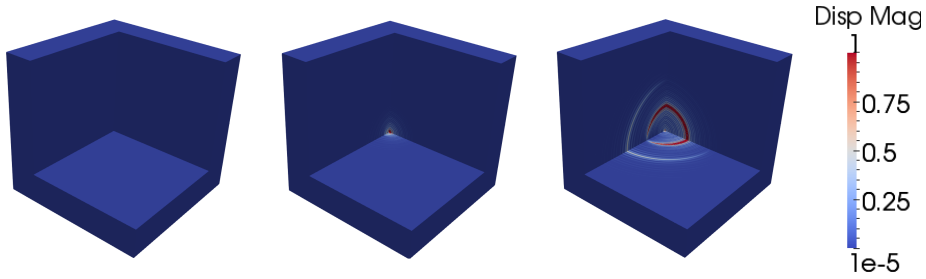

(a) $t = 0.000$ s (b) $t = 0.141$ s (c) $t = 0.282$ s

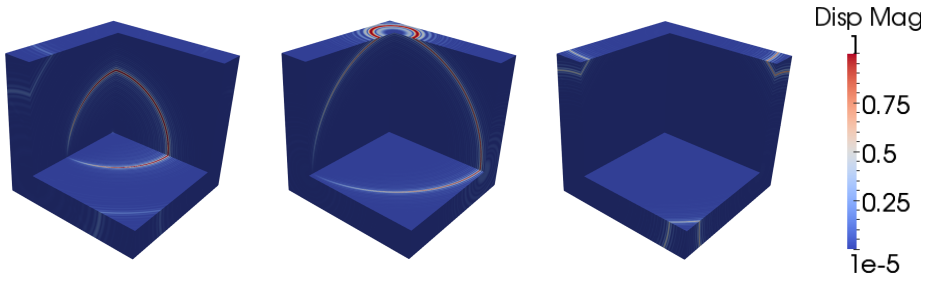

(d) $t = 0.423$ s (e) $t = 0.564$ s (f) $t = 0.705$ s

FIGURE 3.6: Displacement fields in an unbounded homogeneous model. The color scale represents the normalized magnitude of the displacement field, the color scale goes from 1×10^{-5} (blue color) up to 1 (red color).

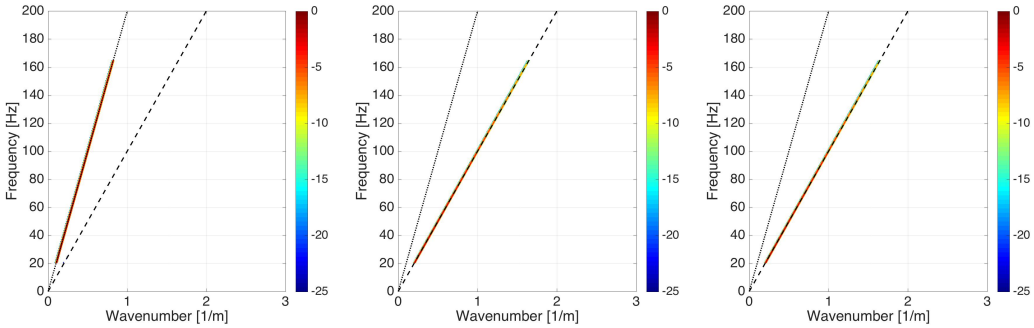

(a) Dispersion: axis x (b) Dispersion: axis y (c) Dispersion: axis z

FIGURE 3.7: Dispersion curves for an unbounded homogeneous media. The color scale is the amplitude of H_{pq} evaluated in Eq. (3.10), limited to values above -25 dB. The dotted black line is the analytical solution for the pressure waves dispersion relation. The dashed black line is the analytical solution for the shear wave.

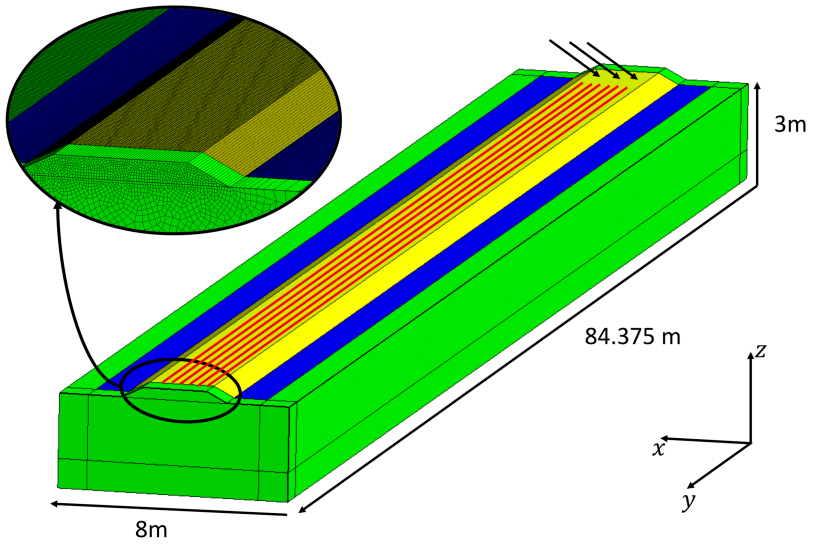

FIGURE 3.8: Geometry, loading (black arrows), and output positions (lines of red dots) for the model. The insert displays the mesh. The ballast appears in yellow, the soil in blue, and the PML region in green.

reflection, mimicking an unbounded medium. The PML uses 5 layers of elements with power degree 3, amplitude 9.87 and total thickness of the PML equal to 2.45 m. The mesh, shown as insert in Fig. 3.8, is discretized by 2.4 millions of non-structured elements, with 375 degrees of freedoms (DOFs) in each element, which amounts to a total of $\approx$ 160 millions DOFs in the entire model.

A series of point forces polarized in the $[1;1;1]$ direction, are positioned at the top of the ballast layer, 9 m away from the border of the model in a non-symmetric arrangement in the transversal section. These sources are expected to excite both shear and longitudinal waves in the model. Their amplitudes are given by an Ormsby function with a plane spectrum between 10 and 400 Hz ($f_1 = 8$ Hz, $f_2 = 10$ Hz, $f_3 = 400$ Hz, and $f_4 = 410$ Hz in Eq. (3.11)). The displacement is recorded in the output positions located along six parallel lines at the top of the ballast layer and aligned with the axis of the track (see Fig. 3.8). The lines are 72 meters-long and the output positions are separated by 0.0732 m $\approx \lambda_{min}/10$. This sampling is sufficient to be able to compute the Fourier transform in space accurately.

The ballast is modeled as a continuum-based randomly-fluctuating elastic medium, as introduced in [5]. Following the polar decomposition of the strain-stress tensor [245]), the density, ρ, and the shear, μ, and bulk moduli, κ, are taken as fully correlated stationary random fields indexed in space. The first-order marginal density for each of these random fields is taken as gamma law with averages $\underline{\rho} = 1570$ kg/m^3, $\underline{\kappa} = 179.60$ MN/m^2 and $\underline{\mu} = 35.32$ MN/m^2, and standard deviations $\sigma_\rho = 3925$ kg/m^3, $\sigma_\kappa = 449.02$ MN/m^2 and $\sigma_\mu = 88.31$ MN/m^2. This corresponds to a ballast layer with (arithmetic) average velocities $V_s = 150$ m/s and $V_p = 380$ m/s [117]. In such heterogeneous setting, the apparent velocities of the homogenized waves are expected to be close to the harmonic averages, which are here approximately $\overline{V}_p = 280$ m/s and $\overline{V}_s = 110$ m/s for the pressure and shear waves, respectively. Note that the standard deviations are equal to 2.5 times the averages, so that the fluctuations are very large. The correlation model [251, 190, 250] corresponds to that of a dense packing of impenetrable spheres of uniform diameter $d = 3.9$ cm in void, with volume ratio $\phi = 0.583$. The details, including identification and comparison with simulations with the discrete element method, can be found in Section 2.1 and Section 2.2. Realizations of the random fields can be obtained using a spectral representation method, specifically tailored for large

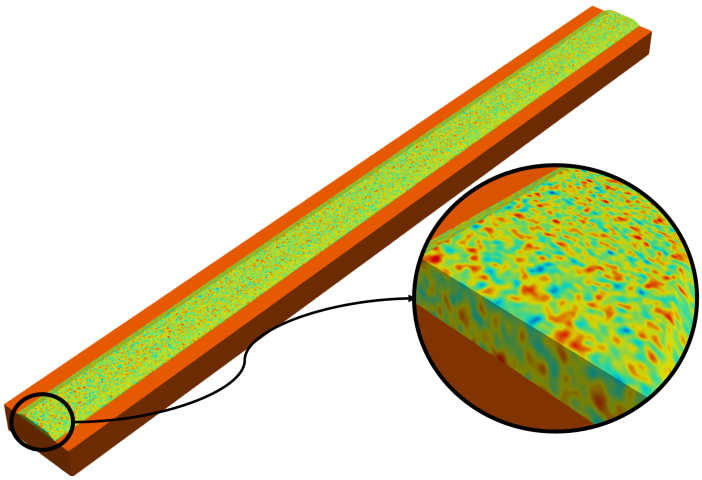

FIGURE 3.9: One realization of the density field in a ballasted railway track (PML not represented).

scale parallel applications [55], and made available as an open-source software [195]. One sample of the random field is provided in Fig. 3.9.

3.3.2 Analysis of the wave patterns

Fig. 3.10 displays snapshots at different times of the normalized displacement field in the ballasted railway track, with a similar normalization as in Fig. 3.6. The first observation is that a large part of the energy seems to remain localized within the vicinity of the source. This is not what is expected from a simulation in a homogeneous domain [69, 5], where waves should propagate non-dispersively with the velocity of a Rayleigh wave. In a setting including a homogeneous ballast layer, the situation would be more complex, and probably involve dispersive waves in the waveguide [69]. However, the fact that part of the energy remains localized close to the source is a specific feature of the heterogeneous model of the ballast. On the snapshots at longer times (at $t = 0.585$ s for instance), there seems to be a separation between waves with longer wavelengths that actually propagate away from the source, and shorter wavelengths that remain localized around the source. This effect therefore seems to be dependent on frequency. A possible explanation for this phenomenon, that seems to be stationary in time, and strongly selective in frequency, is Anderson localization [14, 141, 140], which will be discussed in next section.

3.3.3 Construction of the dispersion curves

We now turn to the construction of the dispersion curves for our model, using the methodology presented in Sec. 3.2.2 and based on displacement field acquired along the output positions indicated in Fig. 3.8. The maps H_{pq} are obtained for each of the 6 lines independently and for 5 different random samples of the ballast layer. The final map is obtained as an average over these 30 individual maps and is plotted in Fig. 3.11.

In this figure, three main frequency regimes are identified. Above about 100 Hz, no energy seems to propagate, which is consistent with Anderson localization. Although no color is seen on the dispersion curve in that regime, it of course does not mean that no energy is present (the source contains frequencies up to 400 Hz). The energy just does not propagate along the axis of the track (which is the direction that is being monitored here) and actually remains mostly localized in the vicinity of the source. This is in accordance with the separation observed between shorts and long wavelengths at later times in Fig. 3.10. Below

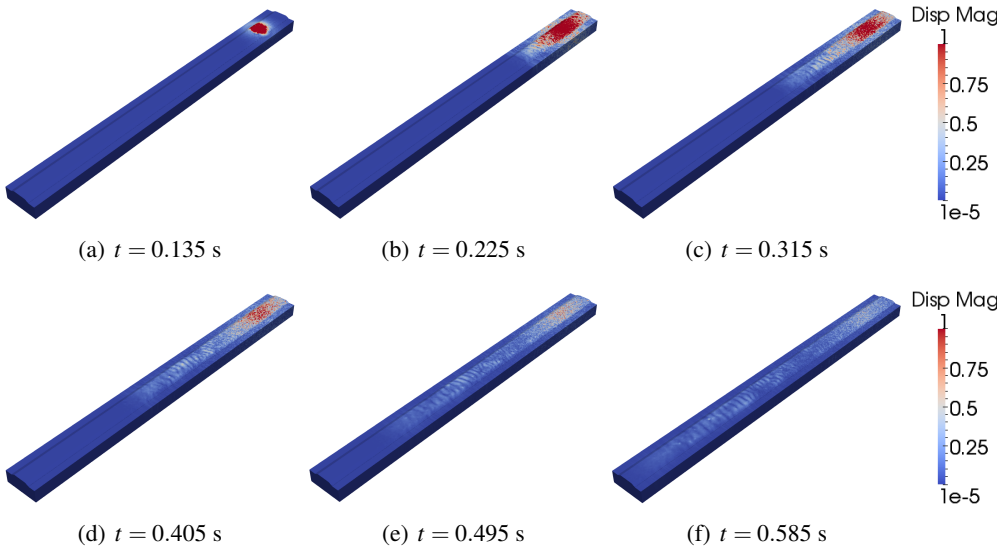

(a) $t = 0.135$ s (b) $t = 0.225$ s (c) $t = 0.315$ s

(d) $t = 0.405$ s (e) $t = 0.495$ s (f) $t = 0.585$ s

FIGURE 3.10: Normalized displacement fields in the ballasted railway track.

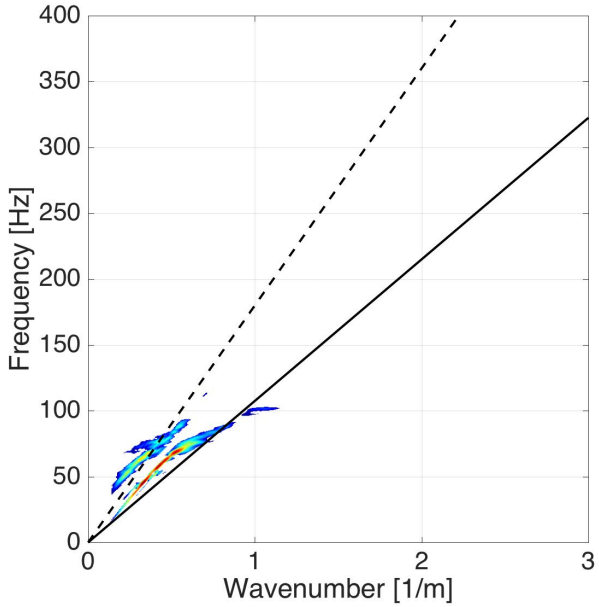

FIGURE 3.11: Dispersion curve for a heterogeneous ballast resting on a homogeneous soil. Dispersion relations for the homogenized ballast shear wave (black solid line) and soil shear wave (black dashed line). The color scale is the amplitude of the average H_{pq} in Eq. (3.10), averaged over 6 lines of output positions and 5 random realizations of the ballast layer. The color scale is limited at -40dB.

about 50 Hz, there seems to be mainly an S-wave (or more probably a Rayleigh wave, whose velocity is slightly smaller) propagating in the soil. At such long wavelengths (compared to the thickness of the ballast), the wave does not really interact with the ballast layer and propagates as if in a homogeneous soil without ballast. Between about 50 Hz and 100 Hz, the soil S/Rayleigh wave starts interacting with the ballast, and its apparent velocity is strongly reduced, approximating that of the ballast layer. A P wave also seems to appear in the ballast (faster than in the soil), bending rapidly with increasing frequency. This general behavior is

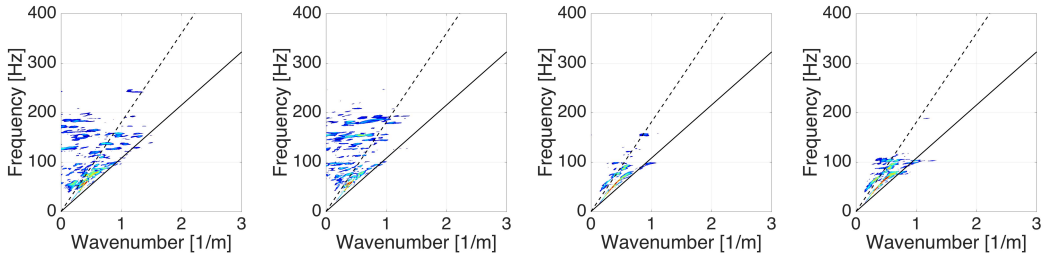

(a) Two lines for the same ballast realization (b) Two ballast realizations

FIGURE 3.12: Dispersion curves for individual maps: (a) for two different lines in the same realization of the ballast layer (no average), and (b) for two different realizations of the ballast layer (averaged over the 6 lines for that realization). Dispersion relations for the homogenized ballast shear wave (black solid line) and soil shear wave (black dashed line). The color scale is limited at -40dB.

.

consistent with experimental observations in unconsolidated granular packings [120].

To get an idea of the fluctuations among the different independent maps (before averaging), the maps corresponding to two different lines for the first realization of the random ballast are plotted in Fig. 3.12, along with the maps corresponding to the average over the 6 lines for two different random realizations of the ballast layer. The few maps presented here are representative of the entire set. Although the average on the lines and the realizations reduces noise, the main features discussed above are present in each and every individual curve. These features are therefore not a chance effect obtained from averaging but really a characteristic behavior of ballasted railway tracks.

3.4 Strong localization analysis

In the previous section, appearance of Anderson localization in ballasted railway tracks was hinted at, with its classical stationary character and a clear frequency dependence. However, there is a possibility that this localization might be some type of guided wave effect, due to the particular geometry of the ballast. This section aims at removing the ambiguity by showing that the same feature would be present in an unbounded domain, composed only of ballast material. Before move on a a few words about Anderson localization were presented.

3.4.1 Anderson localization

The physics Nobel prize of 1977 was given to Philipp Anderson, Nevill Mott, and John van Fleck for their explanation about the metal-insulator transition phenomena in non perfect crystals [14]. The prediction of a localized regime and the transition between the extended mode to a localized mode were presented in the Andersons paper. The localization corresponds to a total absence of energy diffusion in the crystal when some disorder level is present. In the Drude model of electrical conductivity, the electrons are scattered by impurities, bouncing inside the metal and behave as particles. This model captures the finite electrical resistance presented in the metals. However, at lower temperatures, the quantum interference effects become dominant and electrons behave more as waves than as classical particles. This dominance is present at sufficiently strong disorder also, as predicted by Anderson. When the electrons lose their mobility (high leve of impurities) the metal became an

insulator. However, as an interference phenomenon, Anderson localization is not restricted to electrons, it should occurs for any type of wave [138].

In 1959 the first experimental evidence of the Anderson localization was present in spin diffusion [85]. Other works studying light waves [265, 217, 242, 222, 6], microwaves [68, 57, 185], and Lamb waves [261, 145] and acoustic waves [110] also present this behavior. In order to model this phenomena, selfconsistent theory [2, 1, 258, 255, 235, 234, 60] and scale theory [3] were used, but no consensus about the mathematical treatement was found. Another model should be stressed here due to similarity with this work: Leibig proposed a random network of springs and masses to reproduce the wave propagation in granular media [141], one of the results found was localized modes in this network. A similar model was proposed in [48]. In the recent years the development of metamaterials increased the interest into “trapping waves" mechanism using negative equivalent mass and stiffness (see [42] for exemple).

3.4.2 Description of the numerical model

To remove the effect of the ballast geometry and its interface with the underlying soil, we consider an unbounded domain, as in Section 3.2.3. This domain is modeled as a cube of edge 10.98 m, with PMLs all around. The mesh is discretized with a uniform grid of ≈ 7.2 millions cube elements with edge 0.06 m. Polynomials of 4th order are used, inducing close to 1.4 billion DOFs in the entire model. The PML uses 3 layers of elements with power degree 2, amplitude 3.71 and total thickness of the PML equal to 1.69 m. A point force polarized in the x direction, is positioned at $[0.66, 0.66, 0.66]$ m. The time history of the source is that of Eq. (3.11) with a plane spectrum between $f_2 = 40$ Hz and $f_3 = 140$ Hz, and cutoff frequencies at $f_1 = 35$ Hz and $f_4 = 145$ Hz.

Two different media will be considered in this section, and the corresponding two dispersion curves will be constructed. The first medium is homogeneous, with mechanical parameters corresponding to the (arithmetic) average of the ballast in the previous section, with $\underline{\kappa} = 179.60$ MN/m^2, $\underline{\mu} = 35.32$ MN/m^2, and $\underline{\rho} = 1570$ kg/m^3. The second medium is the same heterogeneous ballast as in the previous section and in Section 3.3.1, with average values of $\underline{\kappa} = 179.60$ MN/m^2, $\underline{\mu} = 35.32$ MN/m^2, and $\underline{\rho} = 1570$ kg/m^3, and standard deviations $\sigma_\rho = 3925$ kg/m^3, $\sigma_\kappa = 449.02$ MN/m^2 and $\sigma_\mu = 88.31$ MN/m^2. The correlation model is identical to the one used above to describe the ballast layer and the fields correspond to average velocities of $V_p = 380$ m/s and $V_s = 150$ m/s, and apparent velocities of $\overline{V}_p = 280$ m/s and $\overline{V}_s = 110$ m/s.

Since the geometry is this time isotropic, the lines of output positions for the construction of the dispersion curves can be set in all directions before averaging. Fig. 3.13 shows the position of the output positions, along lines separated by angles of 10^o in both the horizontal and vertical directions, and with output positions along the lines separated by distances of 0.066 m, from 0 m to 10.98 m from the source. The monitors record the displacement in x, y, and z directions.

3.4.3 Analysis of the wave patterns

For each of the two cases considered, Figs. 3.14 and 3.15 display snapshots of the displacement magnitude at different time instants. In the homogeneous case, the expected symmetrically spherical waves are observed. As in Section 3.2.3, P and S waves are observed with different velocities, and with polarizations matching that of the source. On the other hand, in the heterogeneous cases, there is no clear coherent pulse propagating away from the source and the energy remains localized in the vicinity of the source.

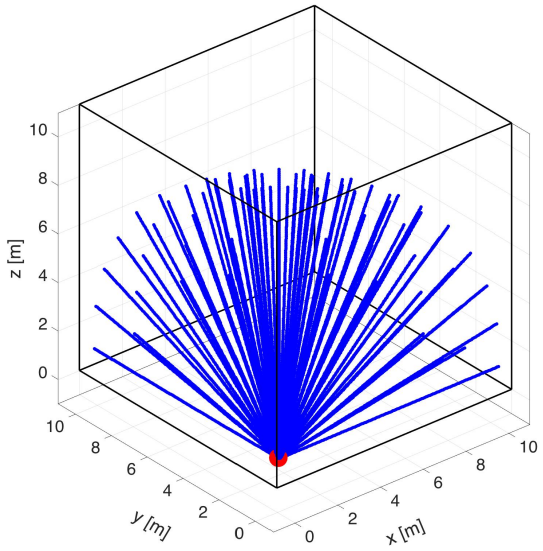

FIGURE 3.13: Position of the monitors (blue line) and the source (red point).

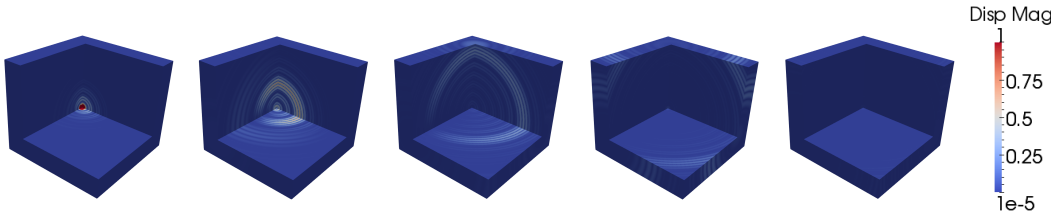

(a) $t = 0.094$ s (b) $t = 0.188$ s (c) $t = 0.282$ s (d) $t = 0.329$ s (e) $t = 0.470$ s

FIGURE 3.14: Normalized displacement field in a homogeneous unbounded medium.

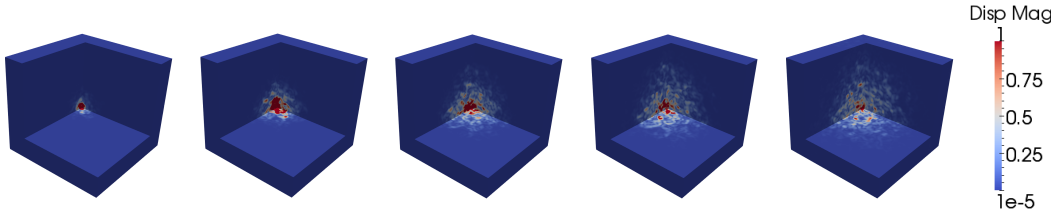

(a) $t = 0.094$ s (b) $t = 0.188$ s (c) $t = 0.282$ s (d) $t = 0.329$ s (e) $t = 0.470$ s

FIGURE 3.15: Normalized displacement field in a heterogeneous unbounded medium.

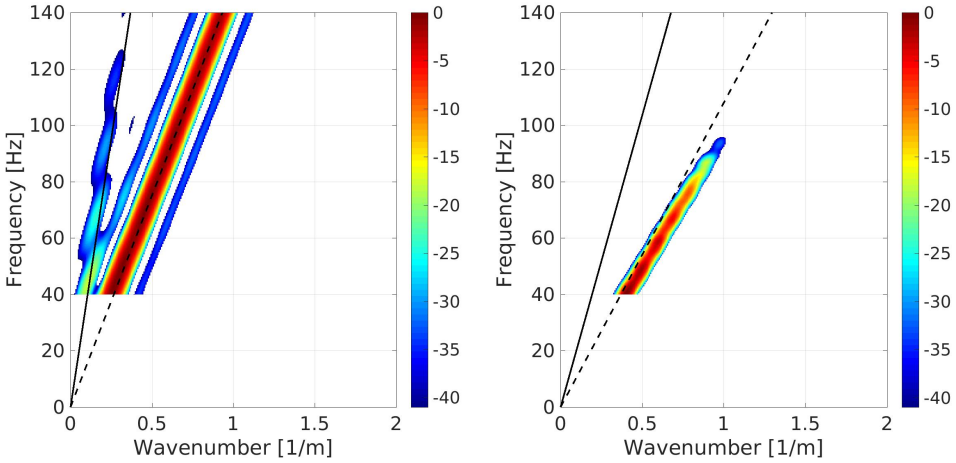

(a) homogeneous (b) heterogeneous

FIGURE 3.16: Dispersion curves for unbounded homogeneous and heterogeneous media. The color scale is the amplitude of H_{pq} evaluated in Eq. (3.10), limited to values above -40 dB. The dotted black line is the analytical solution for the homogenized pressure waves dispersion relation. The dashed black line is the analytical solution for the homogenized shear wave.

3.4.4 Dispersion curve for an unbounded medium of ballast material

Eq. (3.10) was evaluated as an average over the 100 lines monitored for both the homogeneous and heterogeneous cases and Fig. 3.16 present the obtained maps H_{pq}. The reference value used to evaluate the decibel scale was picked from the maximum value of the homogeneous case for both the map in the homogeneous and heterogeneous cases. As expected, a good agreement is obtained in the homogeneous case with both the analytical shear wave and pressure wave modes. Turning to the heterogeneous model, the filtering effect at 100 Hz is clearly observed as in the ballasted railway track of the previous section. This shows that it is indeed an intrinsic property of the heterogeneous material, and not a wave guide effect due to the geometry of the ballasted track. Below 100 Hz, however, the material behaves as a purely isotropic material, which shows that the velocity reduction observed in the previous section was indeed the consequence of the combination of ballast and soil at different wavelengths.

3.4.5 Characterization of Anderson localization

In this last section, we provide additional evidence that the filtering effect above 100 Hz is indeed Anderson localization. Anderson localization is characterized by its strong frequency dependence, which is already apparent in the dispersion curves constructed previously. It is also characterized by the stationarity in time of the localized energy, which means that the energy remains in the vicinity of the source rather than slowly diffusing away. To illustrate this, the displacement magnitude is therefore averaged over all monitors at the same distance from the source and plotted in Figs. 3.17 and 3.18 as a function of time and distance from the source, filtered in three frequency bands (using a second order bandpass Butterworth filter). In the homogeneous case, the energy clearly propagates along a straight line, whose slope is controled by the velocity of the medium. As expected in a non-dispersive medium, this effect is independent of frequency. On the other hand, in the heterogeneous medium, the behavior is strongly dispersive. Below 50 Hz, an isotropic homogenized behavior is retrieved. Above 50 Hz, the energy seems to propagate along vertical lines, which clearly indicates that it remains localized in time at the same distance from the source. The normalization

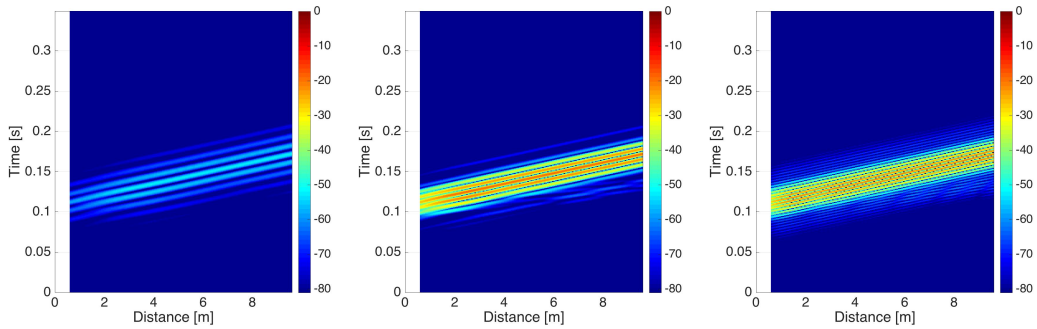

(a) $0-50$ Hz (b) $50-100$ Hz (c) $100-150$ Hz

FIGURE 3.17: Displacement magnitude in an unbounded homogeneous medium. The color scale is the amplitude of the displacement field, limited to values above -80 dB.

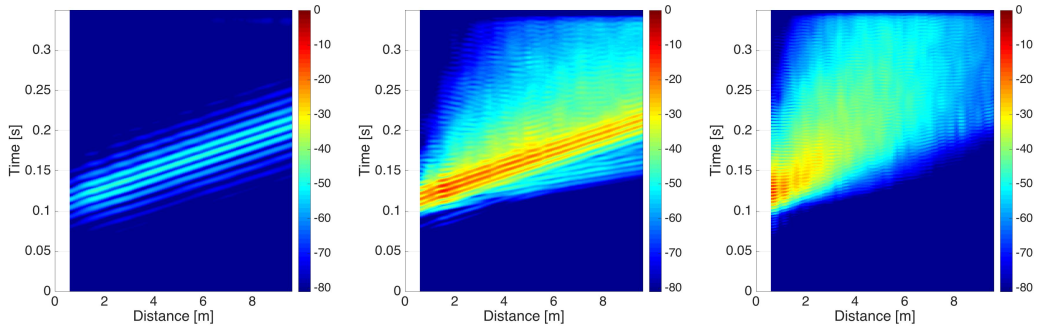

(a) $0-50$ Hz (b) $50-100$ Hz (c) $100-150$ Hz

FIGURE 3.18: Displacement magnitude in an unbounded heterogeneous medium. The color scale is the amplitude of the displacement field, limited to values above -80 dB.

factor for the decibel scale is the maximum displacement magnitude for complete spectra of frequencies.

3.5 Concluding remarks

In this chapter dispersion curves were constructed to analyze the dynamical behavior of a ballasted railway track set on a homogeneous soil. The model proposed in the Chapter 2 was used to model the ballast. The dispersion curve of the ballasted railway track shows a tremendous influence of the heterogeneity. The behavior is dispersive with higher frequency waves going slower than lower frequency waves. Above 100 Hz, Anderson localization sets in, where the higher frequency waves remains trapped in the vicinity of the source. Although very widely studied in the physics literature, this phenomenon has been studied in the acoustical literature only from the experimental angle, trying to discriminate between dissipation and localization in measurements [110]. To conclude, the results presented here seem to indicate that the higher part of the energy generated by the passage of trains on a ballasted railway track remains trapped in the ballast rather than being dissipated in the surrounding soil, contrarily to the common knowledge in the field [180].

Chapter 4

First analyses of experimental measurements on the ballast

In this chapter we start to fill one of the missing points of the Chapter 2. In that chapter the model was fitted using numerical data in a time-independet regime. The main goal of the present chapter is preparing a time-dependent data (used as reference) as an input to the inverse problem in order to take into account the dynamic behaviour. This procedure was done in a similar way in Section 2.1.1. We want use data from physical testing, not numerical. A preliminary analysis of the data is presented in this chapter. It will be used to feed an inverse problem. Unfortunately, due to lack of time, the full identification of the mean and variance of the mechanical parameters could not be completed, despite that, the ongoing work is still performed for publication in articles in the near future. A preliminary identification of the velocity is however presented.

This data comes from two different datasets. The first dataset comes from a laboratory experiment on a small box of ballast made at Laboratoire d'Acoustique de l'Université du Maine (LAUM) by Vincent Tournat and Laurianne Barguet, in a project funded by SNCF I&R. From this dataset we extracted a very preliminar identification of wave velocity. This dataset is described in Sec. 4.1. The second dataset consists of measurements on an instrumented segment of a ballasted HSL on commercial exploitation. The results are presented in Sec. 4.2.

4.1 Measurement of the mobility curve in a ballasted box in a laboratory

In order to better understand the dynamical behaviour of the ballast layer, a controlled experiment was performed in a laboratory condition. A project lead and funded by SNCF was conducted at Laboratoire d'Acoustique de l'Université du Maine (LAUM) by Vincent Tournat and Laurianne Barguet. The main goal of this project was to characterize the dynamical behaviour of the ballast layer. One of the tools used in the railway domain to characterize the dynamical behaviour is the mobility. The mobility $Y_{mn}(\omega)$ is a spectral ratio between the velocity $V_m(\omega)$ measured in a point m as a consequence of the application of a point source $F_n(\omega)$ in position x_n [82]:

$$Y_{mn}(\omega) = \frac{V_m(\omega)}{F_n(\omega)}. \tag{4.1}$$

The next section presents the experimental setup, the measurements made in the ballast box, and finally the mobility curves derived from this test.

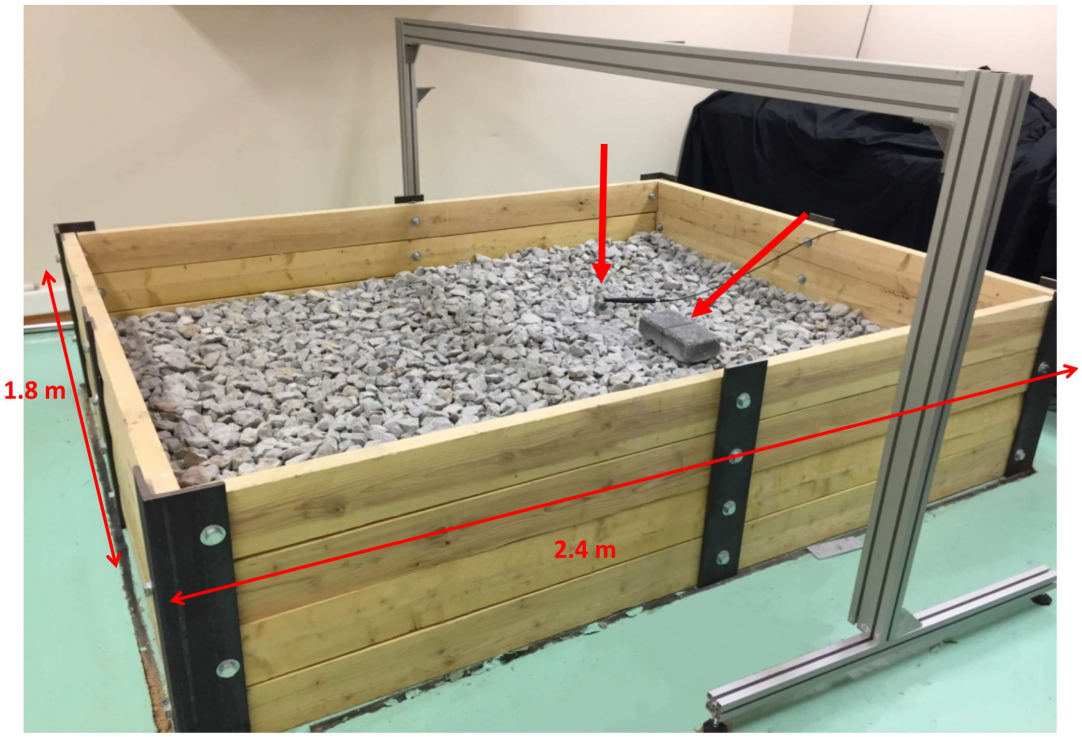

FIGURE 4.1: Experimental setup. Wooden box filled with ballast grains with 1.8×2.4 m^2 and variable thickness. Concrete block, placed at source position 1, (see Fig. 4.2), and impact hammer used in the tests are indicated by the red arrows.

4.1.1 Experimental setup - Ballast box

A ballasted box of 1.8×2.4 m^2 was used to perform the mobility measurements. The tests were performed using two different thicknesses for the ballast layer: 0.255 or 0.29 m. The box configuration is presented in the Fig. 4.1. The box consists of wood planks walls fixed in the ground by bolted steel profiles. The bottom part of the box is the concrete floor. The box was filled with fresh ballast grains (these grains were never used in railways tracks). The density provided by the LAUM was $\rho \approx 1450$ kg/m^3. On the top of the ballast grains a small block ($0.265 \times 0.125 \times 0.08$ m^3) made of concrete was placed in three different positions. It was used to provide a better distribution of the load onto ballast grains, see Fig 4.1. To obtain the mobility curves, an instrumented impact hammer was used to hit the centre of the concrete block (KISTLER 9726A20000 with a sensibility of 0.221 mV/N, and head mass of 500 g). The acceleration produced by the impact was measured simultaneously by a pair of uni-axial accelerometers attached on ballast grains (PCB M352C68 with a sensibility of 100 mV/g and 10 dB of gain). As noted in Fig. 4.1, the surface of the grains are not perfectly flat and/or aligned with the horizontal plane. This difference will introduce an error in the measure, however, we assume that the acceleration measured is vertical. The data acquisition was made with a 6 seconds retangular time window using a sampling rate of 30 KHz.

The variables analyzed in the experimental setup were: thickness of the ballast layer (0.255 m, and 0.29 m); the impact source position (source positions 1 (red), 2 (green), and 3 (blue) in Fig. 4.2); and the distance between the source and the sensor (0.1 m, 0.25 m, 0.79 m, and 1.17 m). Each combination of those variables was tested 10 times to ensure the stability of the results. We summarise these experimental sets in Table 4.1.

TABLE 4.1: Description of the different experimental setups. See Figure 4.2 for a description of the source positions. Ten experiments are realized for each setup.

Set name	Source position	Distance source-sensors [m]	Thickness [m]	Trials
S1d10h25	1	0.10	0.255	10
S1d10h29	1	0.10	0.29	10
S1d25h25	1	0.25	0.255	10
S1d25h29	1	0.25	0.29	10
S2d10h25	2	0.10	0.255	10
S2d10h29	2	0.10	0.29	10
S2d25h25	2	0.25	0.255	10
S2d25h29	2	0.25	0.29	10
S2d79h29	2	0.79	0.29	10
S2d117h29	2	1.17	0.29	10
S3d10h25	3	0.10	0.255	10
S3d10h29	3	0.10	0.29	10
S3d25h25	3	0.25	0.255	10
S3d25h29	3	0.25	0.29	10

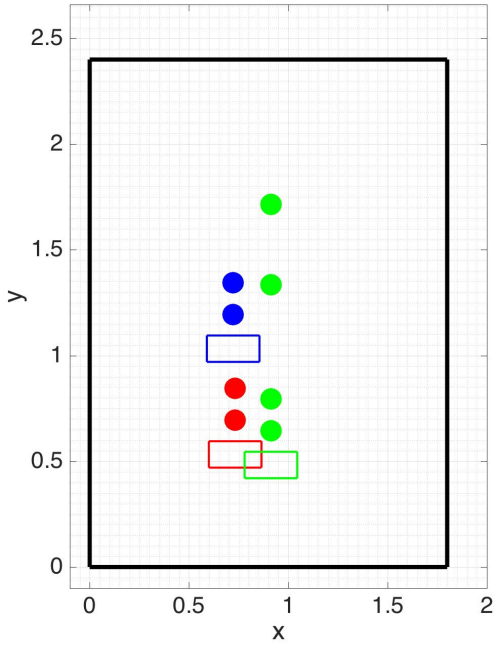

FIGURE 4.2: Schematic representation of the position of the sources and accelerometers in the $x-y$ plane. The red rectangle represents the position of the concrete block for all the sets with source position 1 (S1), the green and blue one represent the same information for source positions 2 (S2) and 3 (S3), respectively. The filled circles are the positions of the accelerometers, the red ones for the set S1, the green ones for S2 and blue ones for S3.

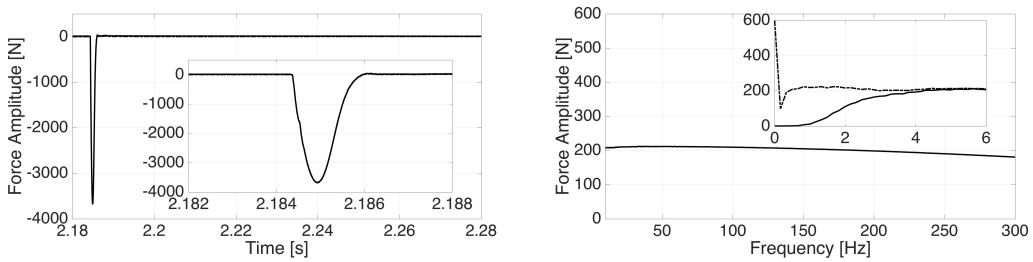

(a) Time history (b) Frequency history

FIGURE 4.3: Force recorded by the impact hammer for the 5th trial of sets S1d10h25 and S1d25h25. Fig. 4.3(a) presents the time history recorded in the impact hammer, Fig. 4.3(b) presents the amplitude of the FFT of the time signal. The solid line is the filtered signal and the dashed line is the non filtered signal.

4.1.2 Recorded data

The obtained signals have a significant low frequency contribution, as shown in the insert of the Fig. 4.3(b) (dashed line is the non filtered signal and solid line the filtered signal). It was removed only for the time-dependent plots by Butterworth [47] high pass filter with a cutoff frequency set at 10 Hz. However, the analysis in Sec. 4.1.3 uses the original recorded data.

Fig. 4.3 presents the force measured by the impact hammer, for a representative case, with the time history shown in Fig. 4.3(a), and the force amplitude vs. frequency in Fig. 4.3(b). The solid line is the filtered data and the dashed line is the non filtered data. Regarding the spectral power introduced by the source in the ballasted box, we can check that the hammer hit is capable to introduce -3 dB up to 300 Hz. The power injected at 300 Hz is close to 2 times lower than at the peak frequency, which is around 50 Hz, with a linear decrease in the amplitude of the excitation.

Fig. 4.4 shows the accelerations obtained in a representative case. The acceleration amplitude time histories for both accelerometers are plotted on Fig. 4.4(a). Fig. 4.4(b) presents the acceleration amplitude vs frequency for the respective time history. Regarding the time histories we observe the presence of two regimes: The first one is dominated by the wave propagation phenomena; and the second one by the modal behavior of the ballast layer. The beginning of those signals present a clear phase difference between the pair of accelerometers, see the insert at Fig. 4.4(a). This phase difference between the sensors reduces over time and around 2.22 s they start to move in phase. In the figure we can see a period of the order of 0.02 s, which corresponds to the main peak at 50 Hz in Fig. 4.4(b). The small size of the box brings up the vibration modes of the structure since the ratio $\lambda/L \approx 1$, where L, in this case, is a characteristic dimension of the box. In the frequency domain, we can see some peaks (indicating the resonances frequencies) and a lower amplitude overall for the furthest sensor.

The dispersion of the recorded data for each configuration was checked through an analysis in the frequency domain. The acceleration magnitude vs frequency for a representative case are presented in Fig. 4.5. The blue solid lines correspond to the trials for the distance of 0.1 m and the magenta one to the distance of 0.25 m. We can check that the dispersion in the data increases with frequency, probably linked with the scattering of the smaller wavelength travelling in the medium. For the low frequency only small variation is observed, the peak frequencies are clearly marked and the dispersion is quite low. We can note, that at high frequencies the accelerations amplitudes are smaller when the distance increase. This behaviour was presented in the literature about wave propagation in granular media as filter effect [140].

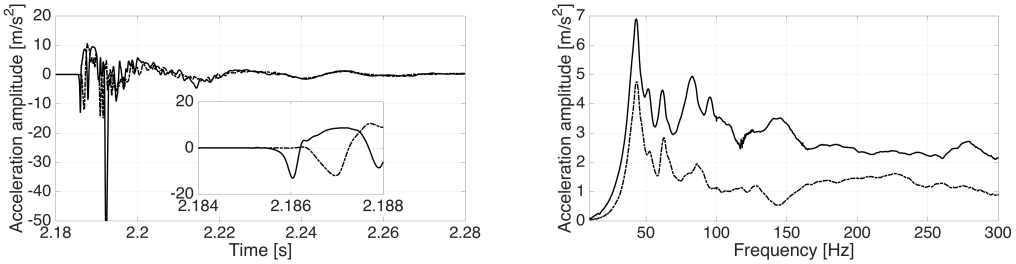

(a) Time history (b) Frequency history

FIGURE 4.4: Acceleration recorded by the sensors for the 5th trial of sets S1d10h25 (solid line) and S1d25h25 (dashed line). Fig. 4.4(a) presents the filtered time history recorded in the accelerometers, the Fig. 4.4(b) presents the amplitude of the FFT of the filtered time signal. Those acceleration histories correspond to the force presented in Fig. 4.3

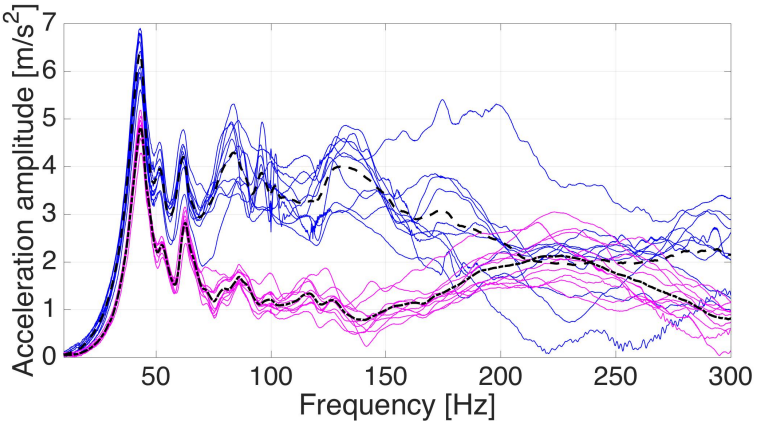

FIGURE 4.5: Acceleration amplitude vs. frequency, each solid line represents one experiment. The blue lines represent the set S1d10h25, with the black dashed lines as the average. The solid magenta lines represent set S1d25h25, with the black dash-dotted line as the average.

Regarding the source variability no major influence was noted, only some variations in the amplitude, as we can see in the Fig. 4.6. All sets were analyzed and have similar results to those presented here.

4.1.3 Mobility curves

In this section the mobility curves obtained from the experiments are presented. Based on the recorded data, acceleration and force, only the inertance/accelerance can be calculated. The inertance can be expressed by:

$$I_{mn}(\omega) = \frac{A_m(\omega)}{F_n(\omega)} = Y_{mn}(\omega) i\omega \tag{4.2}$$

where $I_{mn}(\omega)$ is the inertance, $A_m(\omega)$ is the Fourier Transform of the acceleration a_m at the point m, $F_n(\omega)$ is the Fourier Transform of the force f_n, Y_{mn} the mobility, and i is the imaginary number. Those curves allows us to find out the resonance frequencies of the structure. This measurement is better than a acceleration signal to analyse the resonances, since the influence of the source is removed by the de-convolution. Unfortunately the sensors used in the measurements were able to measure only the vertical component. All the vibrational

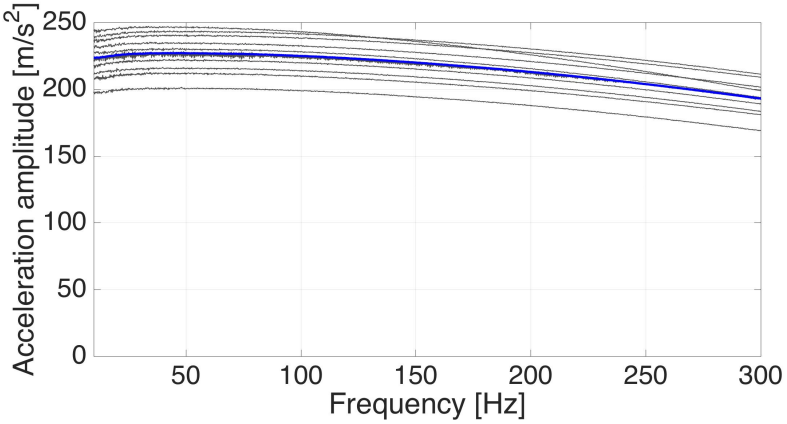

FIGURE 4.6: Force amplitude vs. frequency, each blue solid line represents one experiment. The solid black line is the mean between the realisations.

modes captured by the mobility curve are therefor linked with the modes that produce vertical displacements.

The mobility analysis made here is based on two hypothesis: the system is assumed Linear Time Invariant (LTI); The soil has a very large stiffness compared with the ballast. The first analysis performed is coherence analysis in the data. Then a complete set of mobility curves are presented. Finally, the influence of the source position and thickness on the mobility curves is analyzed.

Coherence analysis

The coherence is a statistic tool that estimates the power transfer between the input and output in a Frequency Response Function (FRF) (defined at Eq. 4.1), in this case the mobility of a linear system. It can be computed as:

$$C(\omega) = \frac{|G_{af}(\omega)|^2}{G_{aa}(\omega)G_{ff}(\omega)} \tag{4.3}$$

where $G_{af}(\omega)$ is the cross-spectral density between the acceleration, a, and the force, f, $|G_{af}(\omega)|$ is the magnitude of the power spectrum densities, and $G_{aa}(\omega)$ and $G_{ff}(\omega)$ are the autospectral density of a and f respectively. When the value of $C(\omega)$ is high, it means that we have a good repeatability of the experiment. This range of frequencies where we have high coherence corresponds to a reliable region for the interpretation of the FRF. Fig. 4.7 shows the mean coherence, in the solid black line, for all the different distances from the source, and the shadow, in gray, represents one standard deviation above and below the mean value. Roughly all measurements present a mean coherence between 0.9 and 1, for frequencies above 20 Hz. However, the measurements at 0.79 and 1.17 m present some frequencies regions with lower coherence. This result is due to the low number of trials for this configuration.

Mobility curves

The mobility curves presented in Fig. 4.8 and Fig. 4.9 were obtained using the Eq. 4.2. Fig. 4.8 shows the 10 trials made for the source position 1, thickness of 0.255 m and distances of 0.10 m and 0.25 m from source-sensor. They are plotted in solid gray lines, with the mean value plotted in solid blue line. Regarding the mobility, we note that the overall behaviour of the 10 trails are quite the same. In the low frequencies (between 20 Hz and 60 Hz) a small dispersion of the data is observed, when the frequency increases the dispersion increases. The

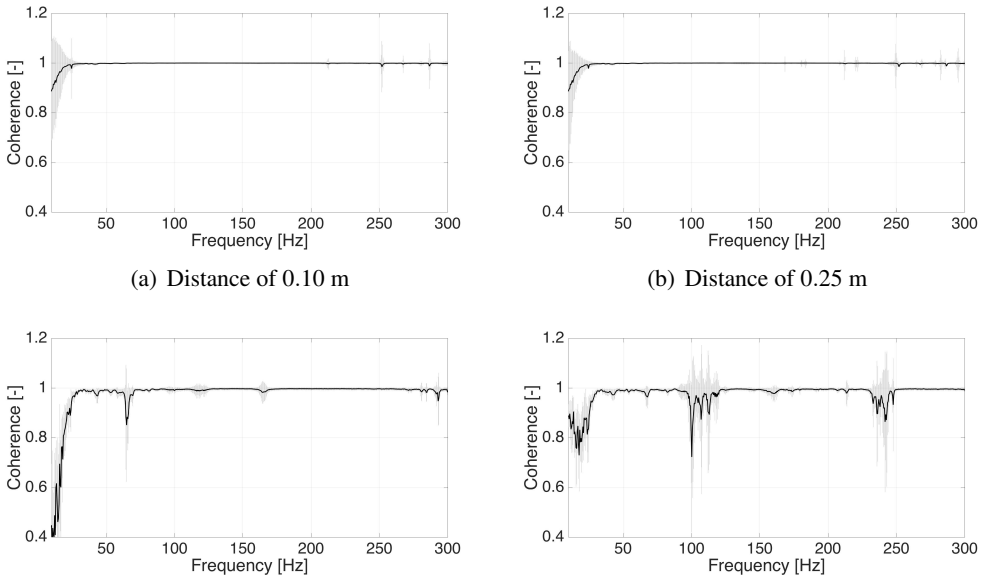

(a) Distance of 0.10 m

(b) Distance of 0.25 m

(c) Distance of 0.79 m

(d) Distance of 1.17 m

FIGURE 4.7: Coherence curves for the different sets. The solid black lines correspond to the mean coherence. The gray surface represents one standard deviation above and below the mean value.

mean mobility curve shows some resonance frequencies, for both distances. The predominant resonance, around 40 Hz was already noted in Fig.4.4(a). Resonances around 55 Hz and 65 Hz are also visible. Regarding the predominant resonance at 40 Hz a low quality factor can be noted.The energy of the system is almost all dissipated in this resonance. The low quality factor introduces a large bandwidth in this peak, making the identification of the other resonances in this area less evident. In the plots, an attenuation in high frequencies is noted, this "filter effect" is reported in the granular material literature [140]. The linear trend present in the phase plot indicate the presence of group delay in our experiment. The group delay is treated in explained in the next section.

Fig. 4.9 shows the 10 trials made for the source position 2, thickness of 0.29 m and distances of 0.79 m and 1.17 m from source-sensor. They are plotted in solid gray lines, with the mean value plotted in solid blue line, note that the scale is not the same as on Fig. 4.8 since the increase of the distance sensor-source reduced the energy captured by the sensors. Resonance frequencies around 50 Hz are still present for this configuration of the test in both distances, however their identification becomes more difficult due to the presence of many vibrational modes.

Group delay analysis

The analysis of the phase response in Fig. 4.8 and Fig. 4.9 shows the presence of a group delay in the phase mobility response of the ballast box. The group delay may be interpreted as the time delay of the amplitude envelope of a sinusoid at frequency ω. It can be interpreted as dispersion also, where each frequency propagates at a different speed. This behaviour is common in the study of linear systems when propagation phenomena occurs [45, 172, 53]. It means that the output, acceleration/velocity, has a delay compared with the input, the force. The group delay can be evaluated using the following relation:

$$\tau(\omega) = -\frac{d[\angle Y(\omega)]}{d\omega} \tag{4.4}$$

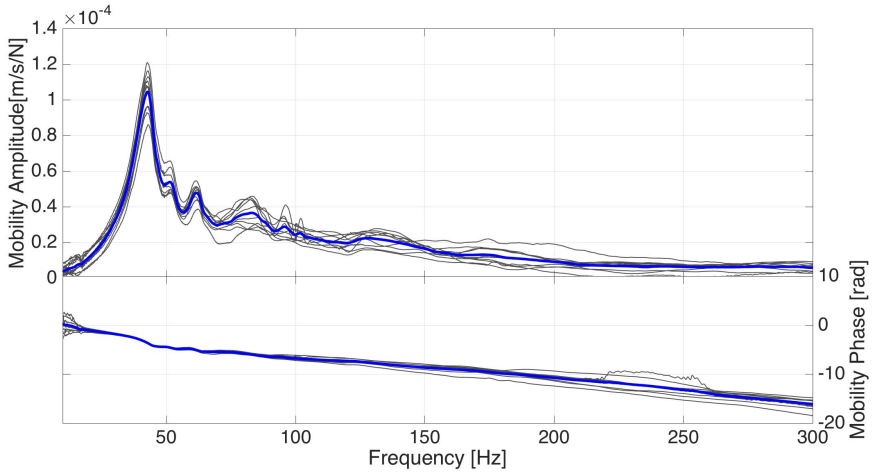

(a) 0.10 m away from the source

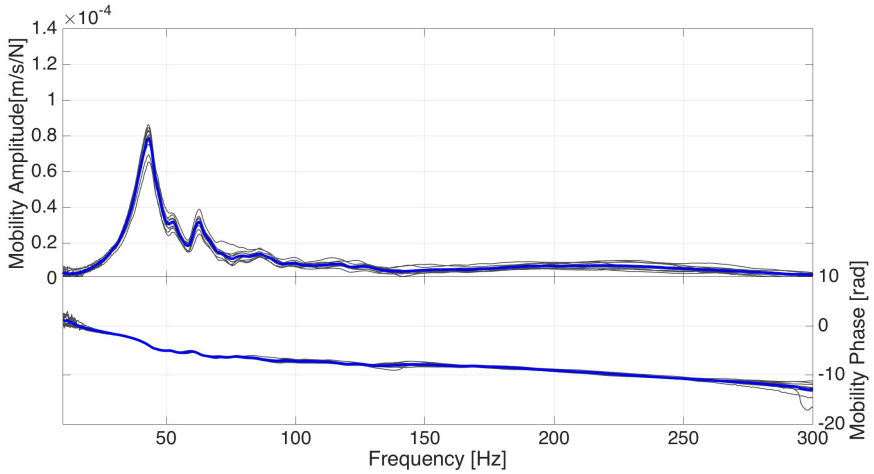

(b) 0.25 m away from the source

FIGURE 4.8: Amplitude and unwraped phase from mobility curves. The gray solid lines correspond to the different trials . Those mobility curves were extracted from the source position 1 and thickness of 0.255 m for both sensor-source distance (0.10 m and 0.25 m). The blue solid lines represent the mean between the experiments.

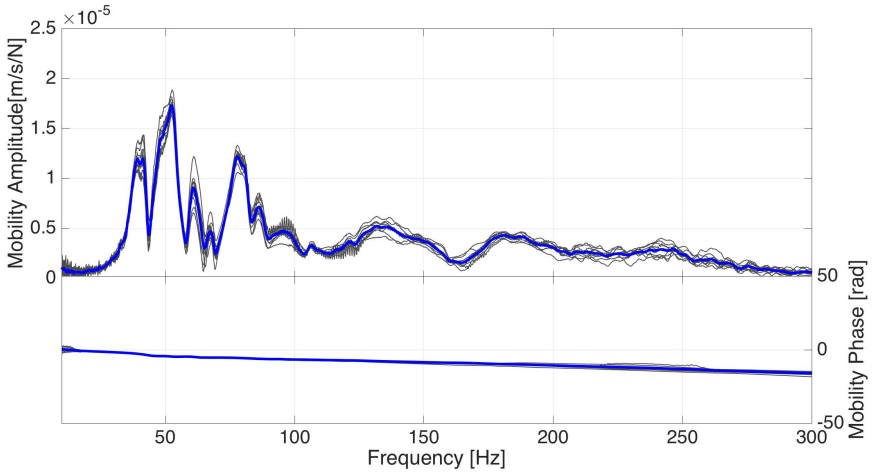

(a) 0.79 m away from the source

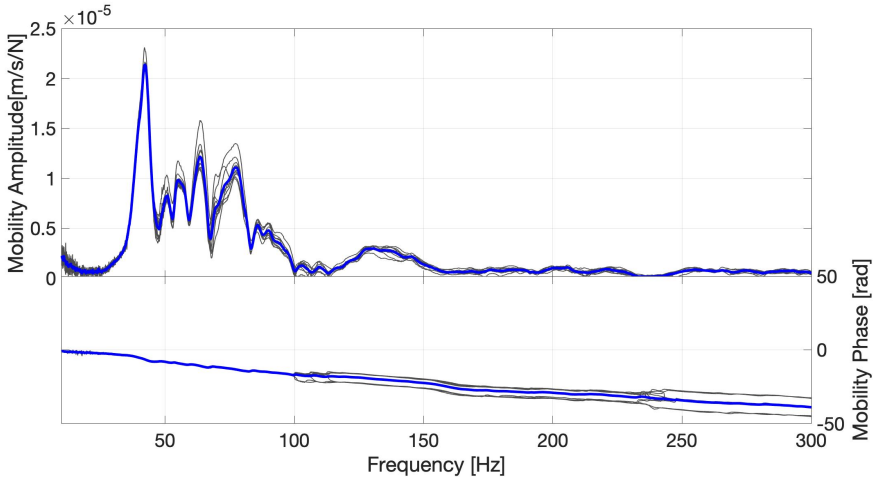

(b) 1.17 m away from the source

FIGURE 4.9: Amplitude and unwraped phase from mobility curves. The gray solid lines correspond to the different trials. Those mobility curves were extracted from the source position 2 and thickness of 0.29 m for both sensor-source distance (0.79 m and 1.17 m). The blue solid lines represent the mean between the experiments.

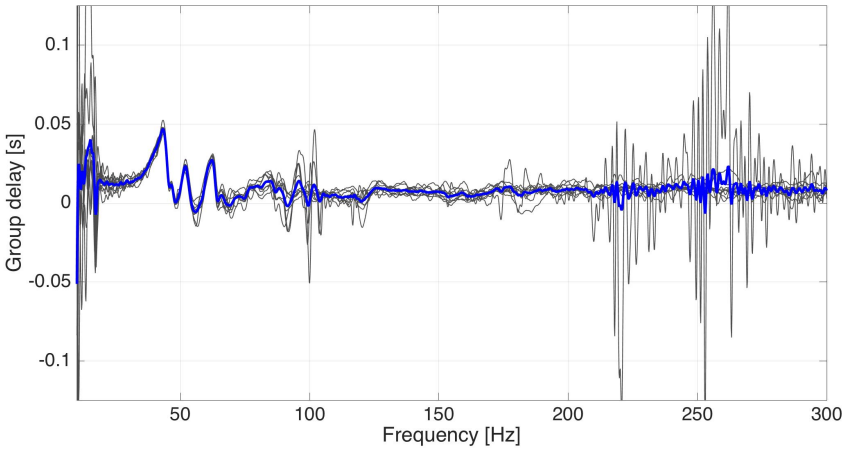

(a) 0.10 m away from the source

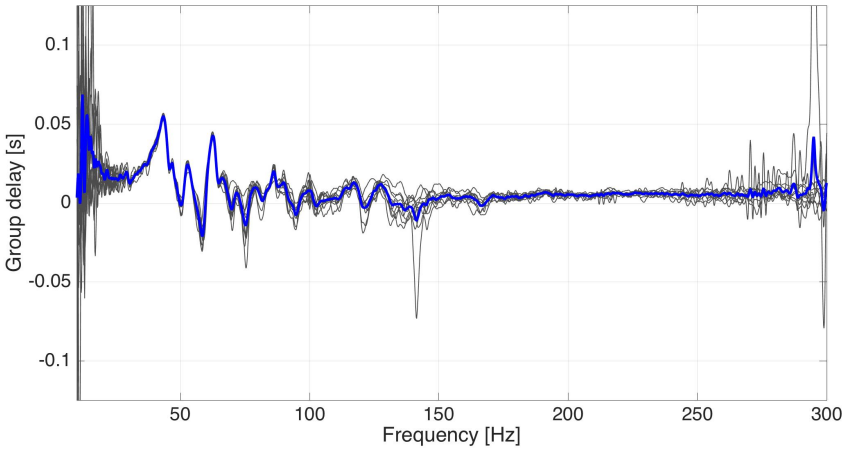

(b) 0.25 m away from the source

FIGURE 4.10: Group delay vs. frequency. The solid gray lines are the 10 tests performed for each setup (S1d10h25 and S1d25h25) . The blue solid lines represent the average between the tests.

where $\angle Y(\omega)$ is the unwrapped phase of the mobility, and τ is the group delay.

The group delay can be seen in Fig. 4.10 where the Eq. 4.4 was evaluated for a representative case. The gray solid lines represent each test made, and the solid blue line represents the mean value. The group delay presents a positive mean value, as expected, due to the negative slope in the phase plot of the Fig. 4.8. We note the increase of the delay near the resonance frequencies, as expected [172].

Influence of the source position

The Fig. 4.11 presents the influence of the source position on the mobility curve. Each line in the graphs corresponds to the average of the 20 realisations of a given configuration. The left figure is the sensor at 0.1 m and the right is the sensor placed at 0.25 m from the source. The source position 1 presents, for all distances, the highest amplitude level for the mobility peak. For the sensor placed at 0.10 m away from the source the amplitudes in the high frequency regime are very similar for the positions 1 and 2, and lower for the position 3. At the same time for the sensor placed at 0.25 m there is no significant difference between the 3

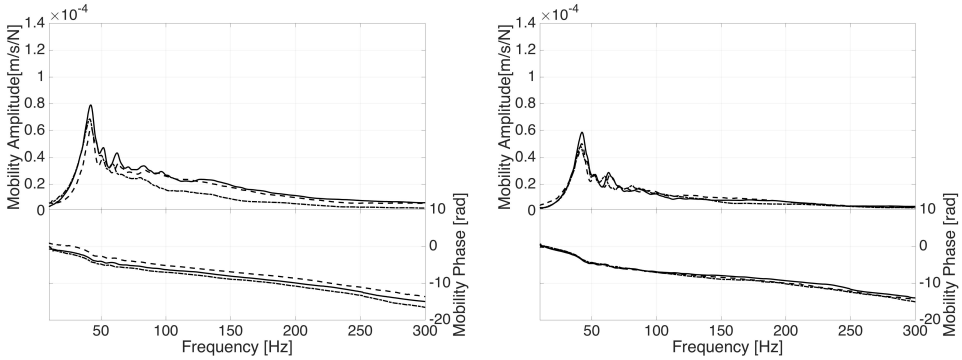

(a) 0.10 m from the source (b) 0.25 m from the source

FIGURE 4.11: Influence of the source position in mobility vs frequency curves. The solid lines stand for the position 1, dashed lines stand for the position 2, the dotted lines stand for position 3.

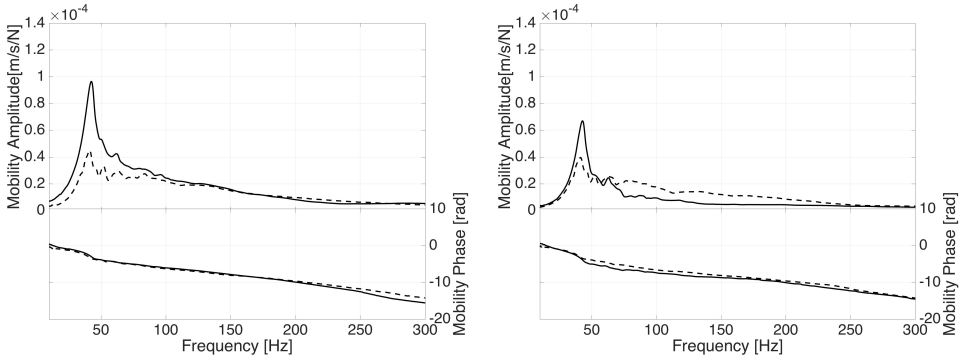

(a) 0.10 m from the source (b) 0.25 m from the source

FIGURE 4.12: Influence of the thickness in the mobility response. The solid lines represent the thinner case, 0.255 m, and the dashed lines the thicker case ,0.29 m.

source positions. The resonance peaks are preserved at the same location for the three source positions, around 42 Hz. The small variation between the main resonance frequency for each source position are in the same level of variation between each measurement made in the 10 trails set, as shown in Fig. 4.8.

Influence of the thickness

In the Fig. 4.12 we check the influence of the layer thickness on mobility for the first set. Each line in the graphs corresponds to the average of the 30 realisations of a given configuration. The solid line represents the thinnest layer, 0.255 m, and the dashed line is obtained from the thickest thickness, 0.29 m. The first analysis shows no significant difference in the position of the resonance peaks, and a reduction in the amplitude of the peaks at a low-frequency range, below 100 Hz. In the high frequency both curves are very similar, in shape and amplitude. The phase information shows similar behaviour between the two thicknesses, presenting almost no significant difference for both cases. The small variation between the main resonance frequency for each thickness are in the same level of variation between each measurement made in the 10 trails set, as shown in Fig. 4.8.

4.1.4 Identification of shear wave velocity in the ballasted box

In this subsection we try to identify the wave velocity using two different methods. As presented in Sec. 4.1.2, we take advantage of both physical phenomena (wave propagation and modal resonance) to measure the velocity. The first approach is based on measurements of the wave time-of-flight between between sensors at short times. The second one uses the vibrational response of the structure, with a simple analytical model to identify the wave velocity.

Measure of the time-of-flight

In order to obtain the velocity we treated our data using an interferometry technique [107]. The time delay, τ_{max}, between two signals, f and g, is calculated using:

$$\tau_{max} = \max_t((f \star g)(t)) \tag{4.5}$$

where $(f \star g)(t)$ is the cross-correlation, expressed by,

$$(f \star g)(\tau) = \int_{-\infty}^{\infty} f(t)g(t+\tau)dt \tag{4.6}$$

where τ is the the lag-time. In our experimental setup the time delay between sensors was calculated. As we know the positions of the sensors, the velocity can be determined using:

$$V_s = \frac{\Delta x}{\tau_{max}}. \tag{4.7}$$

Unfortunately, the propagation in uncertainty [202] in Eq. (4.7) is unknown. Informations like the distance between the accelerometers and the instrument used to measure the distance were not reported. The lack of this information makes it impossible to evaluate the error propagation.

Sets in very early in Sec. 4.1.1, we saw that the modal behaviour influence of that regime in the experiments. To avoid this influence only the first part of the signal is used. Fig. 4.13 shows the original signal in solid black lines, in dotted black line a signal after the application of a Tukey window [105, 170]. This procedure was applied in all the signals. The process of time-delay evaluation was performed evaluating the Eq. 4.5. This sequence is showed in Fig. 4.13(c). The solid black line represents the evaluation of the Eq. 4.6. The solid blue line represents the evaluation of the τ_{max}. Unfortunately, some of the measurements presented anomalies that made their use difficult in the identification. As presented in Fig. 4.14, the presence of an inversion of the first arrival between the two accelerometers of the same experiment sometimes led to erroneous estimation of the velocity. These very high values (above 2000m/s for instance) have been disregarded.

The Table 4.2 presents the measurements made for the ballast thickness of 0.255 m, and Table 4.3 for the thickness of 0.29 m. The summary of those measurements can be found in the Table 4.4. Those velocities are comparable with literature values, for exemple, 180 m/s [117].

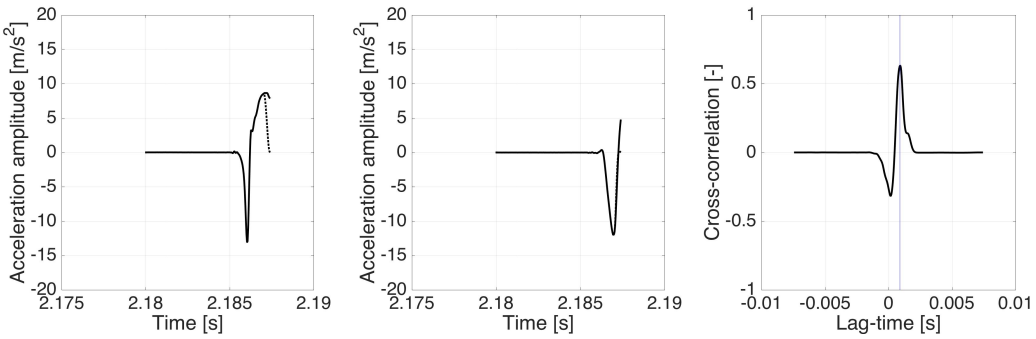

(a) Accelerometer signal at 0.1 m (b) Accelerometer signal at 0.25 m (c) Between accelerometers

FIGURE 4.13: Procedure to identify the time delay. The accelerometers records and the correlation between them. For the accelerometer the original signal is presented in solid line, the dotted line is the windowed signal. The correlation is represented in solid line, and the blue line is the time delay.

TABLE 4.2: Velocity measurements: Thickness 0.255 m. V_{12} [m/s] is the velocity between sensors.

Trial	Source position 1	Source position 2	Source position 3
1	136.36	-	109.76
2	187.50	-	214.29
3	140.62	-	102.27
4	-	-	236.84
5	180.00	264.71	-
6	187.50	-	95.74
7	155.17	-	72.58
8	321.43	-	195.65
9	173.08	-	-
10	225.00	346.15	88.24
Mean	189.62	305.42	139.42
Standard deviation	56.37	57.59	64.93

TABLE 4.3: Velocity measurements: Thickness 0.29 m. V_{12} [m/s] is the velocity between sensors.

Trial	Source position 1	Source position 2	Source position 3
1	-	346.15	132.35
2	-	-	150.00
3	195.65	204.55	109.76
4	187.50	-	145.16
5	204.55	321.43	140.62
6	128.57	-	160.71
7	-	321.43	155.17
8	300.00	264.71	150.00
9	-	321.43	321.43
10	264.71	250.00	346.15
Mean	213.49	289.95	181.13
Standard deviation	60.64	51.08	81.88

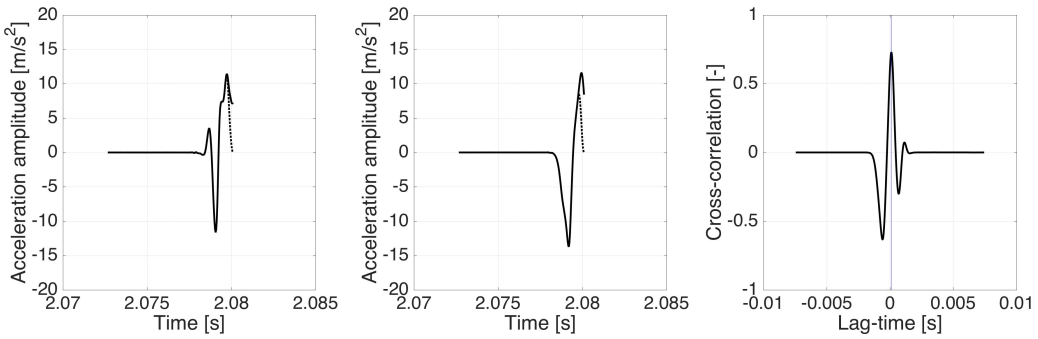

(a) Accelerometer signal at 0.10 m (b) Accelerometer signal at 0.25 m (c) Between accelerometers

FIGURE 4.14: Illustration of the problem of using correlation for the estimation of wave propagation velocity.

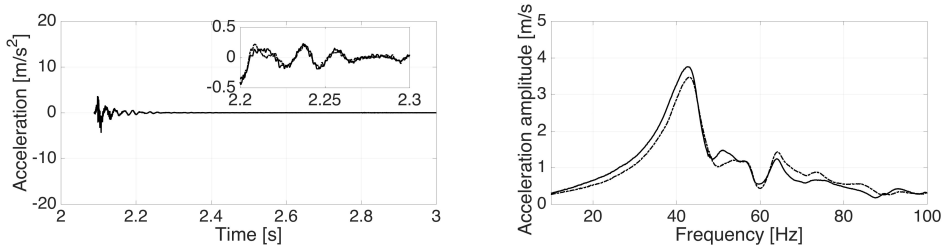

(a) Time history (b) Frequency history

FIGURE 4.15: A windowed signal of acceleration recorded. The solid lines correspond to the closest sensor 0.10 m and the dashed-dot lines correspond to the furthest sensor 0.25 m. The insert in the time history shows in detail the acceleration signal.

TABLE 4.4: Mean velocity and standard deviation of the velocity. V_{12} is the velocity measured between sensors.

	V_{12} [m/s]
$\underline{v}$	202.60
σ_v	80.42
trials	42

Identification on modal behaviour

In the previous section we windowed the signals in order to obtain only the part relative to the transient behaviour. In this section, our analysis focuses on the vibrational behaviour. Fig. 4.15 shows the time history and the frequency spectrum of the vibrational part of the windowed acceleration. The insert shows that the two sensors are in phase.

The model proposed in order to estimate the homogenized velocity in the medium is a simple vibrational model for a rectangular block. To carry it out, it was assumed that in the low frequency regime (below 100 Hz) the heterogeneity is homogenized. In other words, the wavelength of the vibration is much larger than the size of the ballast grains, so the medium can be seen as a homogenized continuum. We use a linear elastic isotropic medium to model the ballast box. The Dirichlet boundary conditions were considered as: free-free displacement in the axes x and y; and in z-axis a fixed-free displacement. A schematic view

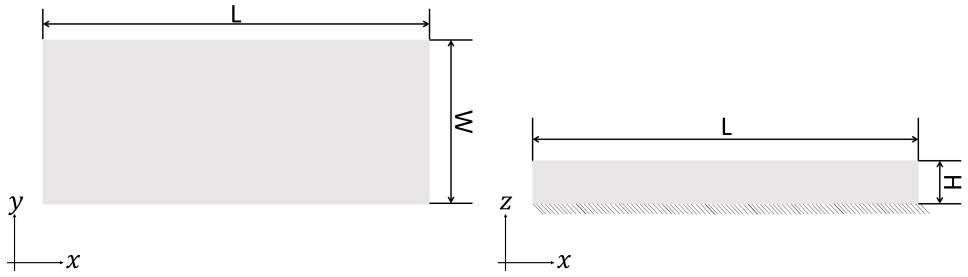

(a) $x-y$ view (b) $x-z$ view

FIGURE 4.16: Boundary conditions imposed to the model.

of the problem is presented in Fig. 4.16. The variable separation method was applied in the solution of the equilibrium equation for the vibrations in a rectangular box leading to:

$$\frac{\partial^2 w}{\partial t^2} = c_{sv}^2 \left(\frac{\partial^2 w}{\partial x^2} + \frac{\partial^2 w}{\partial y^2} \right), \tag{4.8a}$$

$$\frac{\partial^2 u}{\partial t^2} = c_p^2 \frac{\partial^2 u}{\partial z^2}, \tag{4.8b}$$

where w and u are the transversal and longitudinal displacement, respectively, the subscript sv is to indicate shear vertical velocity and the p subscript is for longitudinal velocity. As we stressed at the beginning of this section, only displacements in the vertical axis can be measured. So, the only modes that were captured by the accelerometers are: transversal modes in x and y-axis, and longitudinal modes in the thickness, z-axis. This restriction drove us to this model. From Eq. 4.8 we derive the dispersion relation:

$$\omega^2 = c_{sv}^2 k_x^2 + c_{sv}^2 k_y^2 + c_p^2 k_z^2, \tag{4.9}$$

with k_x, k_y, k_z as the components of the wave-number in [rad/m]. The wavenumbers that satisfy the boundary conditions are $k_x = a/2L$, $k_y = b/2W$ and $k_z = c/4H$, where a, b, and c is the modal order for the x, y, and z-axis, respectively, L, W and H are the length, width and height of the box, respectively. Rewriting the Eq. 4.9 we find:

$$f_i^2 = c_{sv}^2 \left(\left(\frac{a}{2L} \right)^2 + \left(\frac{b}{2W} \right)^2 \right) + c_p^2 \left(\frac{c}{4H} \right)^2, \tag{4.10}$$

finally f_i is the i resonance frequency. Each tripet (a,b,c) corresponds to one resonance frequency f_i, Fig. 4.17 shows the deformation shape of the box for some triplets (a,b,c).

Identification of the resonance frequencies and inverse problem

Now we turn our attention to the identification of the resonance frequencies of the box. Fig. 4.18 displays all the 60 tests made for each inertance evaluated. The blue lines are the inertances for the thinest ballast height 0.255 m and the red ones for the thickest 0.29 m. Dotted lines were used to represent the closest sensor, 0.10 m, ands dashed line the sensor placed at 0.25 m. The first behaviour that can be noted is the shift of the main resonance peak. The peak moves to lower frequencies when the thickness of the layer increases (mean value of -1.60 Hz). It can indicate the presence of a mode that is affected by the variation of the thickness, as a longitudinal mode in the thickness. For this frequency we set the first longitudinal mode in the thickness (assuming no coupling with the transversal modes the

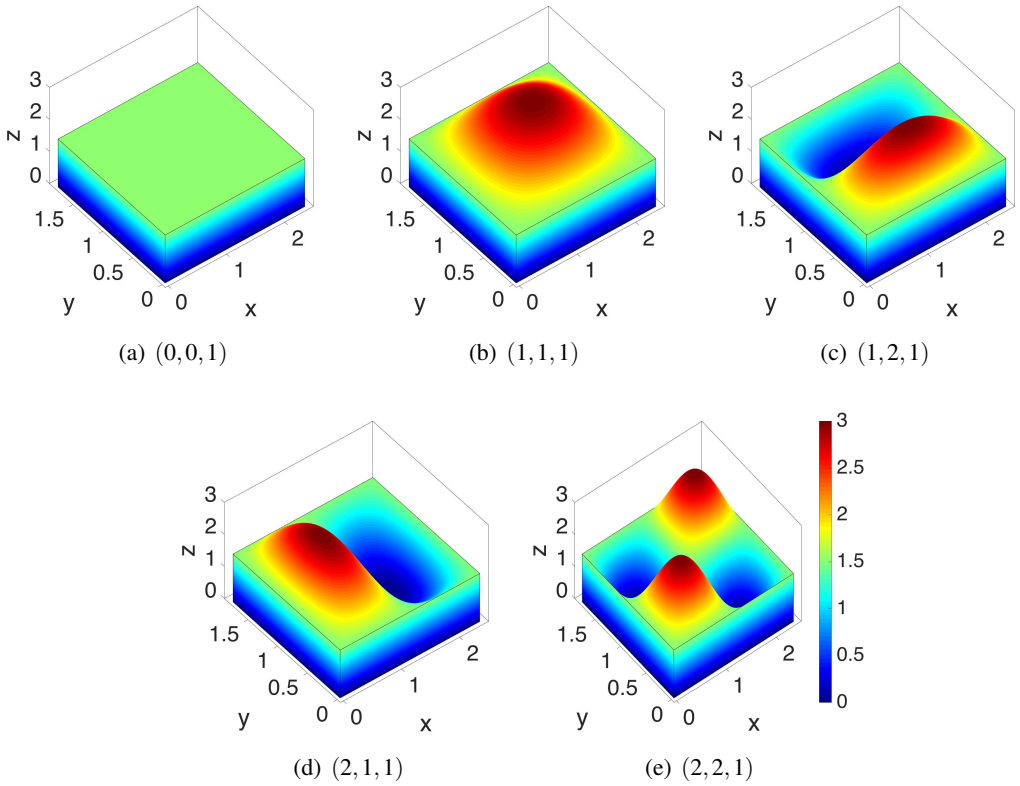

FIGURE 4.17: Transversal and longitudinal vibrational modes in a rectangular box. The colour scale is an arbitrary vertical displacement.

triplet). The Eq. 4.10 can be simplified as:

$$f = c_p \left(\frac{1}{4H} \right). \tag{4.11}$$

The inverse problem, in this case, is: $c_p = 4Hf$, where f is the resonance frequency. The results are presented in Table 4.5. Fig. 4.18 shows also the resonance frequencies used to evaluate the Eq. 4.11. The vertical green lines correspond to the resonance frequency for the thickness of 0.255 m and the magenta one the resonances for the thickness of 0.29 m. Regarding the dominant resonance, around 42 Hz, a low quality factor can be noted, in other words, almost all the energy of the system is dissipated in this resonance. The low quality factor introduces a large bandwidth in this peak, making the identification of the other resonances in this area less evident. The other resonance frequencies (transversal modes and the coupled modes) should be studied in further analysis.

TABLE 4.5: Mean velocity and standard deviation of the velocity, evaluated in the Eq. 4.11. S1, S2, and S3 correspond to the positions of the source, 1, 2, and 3, respectively.

	S1 [m/s]	S2 [m/s]	S3 [m/s]	All [m/s]
$\underline{c_p}$	45.70	45.98	44.60	45.43
σ_{c_p}	1.95	2.35	1.74	2.10

The histogram of the velocities obtained is presented in Fig. 4.19(b). Fig. 4.19 shows a comparison between the methods used to measure the velocity. The histogram of the shear

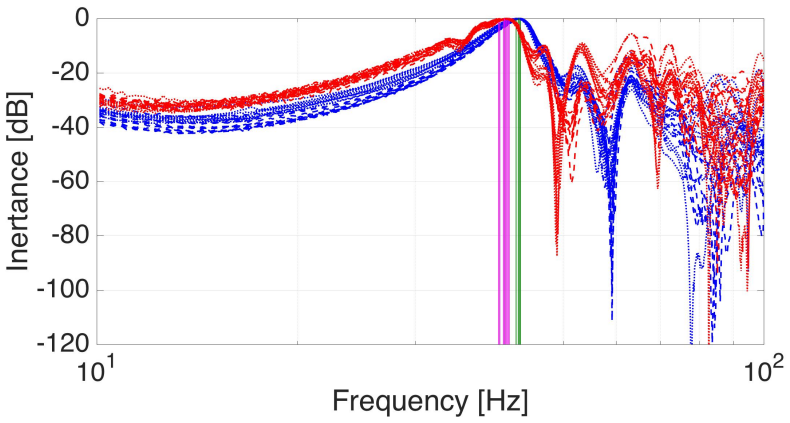

(a) Source position 1

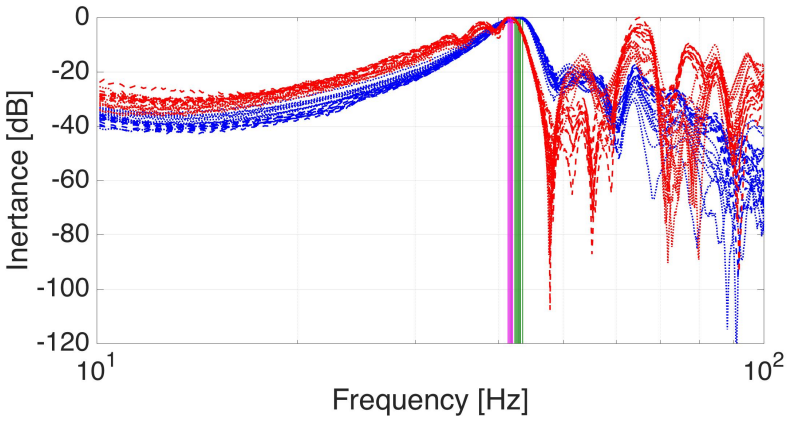

(b) Source position 2

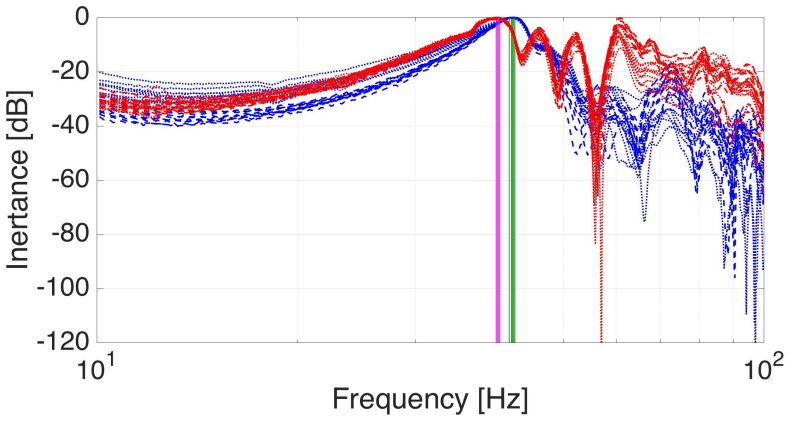

(c) Source position 3

FIGURE 4.18: Magnitude of the inertance for the ballast box. The blue lines are the inertance for the thinest ballast height, 0.255 m, and the red ones for the thickest, 0.29 m. Dotted lines were used to represent the closest sensor, 0.10 m, and the dashed line the sensor placed at 0.25 m. The vertical green lines correspond to the resonance frequency for the thickness of 0.255 m and the magenta one the resonances for the thickness of 0.29 m.

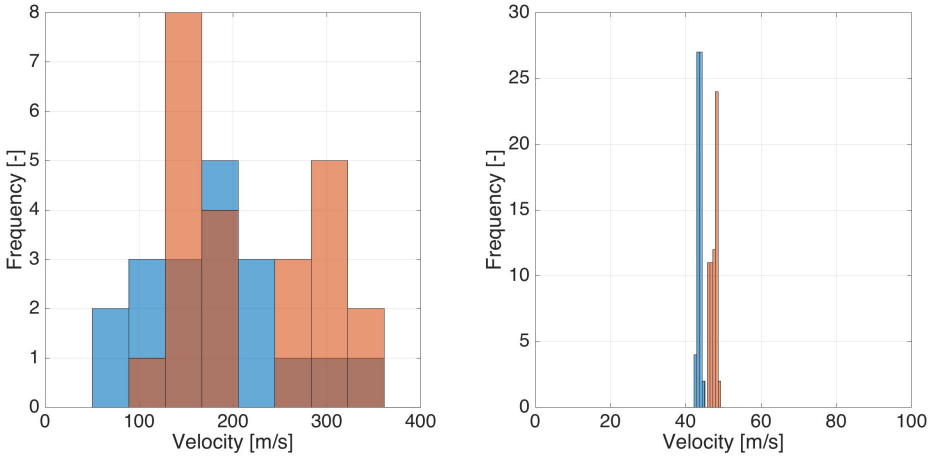

(a) Time of flight

(b) Vibrational response

FIGURE 4.19: Histogram for the measured velocity. In the left figure we present in blue the shear velocities for the thickness of 0.255 m and in orange the shear velocities for the thickness of 0.29 m. The right one present the histogram velocity identified using the resonance information, the blue one is the the pressure velocities for the thickness of 0.255 m and in orange the pressure velocities for the thickness of 0.29 m.

velocity measured by correlation and the pressure velocity measure by the inverse vibrational problem are plotted in this figure. Clearly, one huge discrepancy in the velocity measurements performed by both methods was noted. The velocities have one order of magnitude of difference. We expected to find a shear wave velocity lower than the pressure velocity (around 28 m/s if we set $\nu = 0.22$ [117]). While the correlation measurement lead to a much higher shear wave velocity, around 160 m/s. First of all, the velocity measured by the vibrational method is a global measure, since it depends on a mode of vibration of the entire structure. The correlation method measures a local property, only a few grains of ballast were between the source and the accelerometers. This produces a much higher dispersion in the results, once that the contact network, or force chains, changes significantly from one configuration to another. Other variable very important in this case is the compactness. To conclude, simulations should be performed to check this behaviour. The difference between local and global velocities can be used to estimate the variance and mean of the stochastic fields used to model the granular medium.

4.2 Acceleration measurements on a real ballasted HSL

This section describes one set of measurements made by SNCF Innovation & Research to analyse the response of the ballast layer during the passage of a HST on commercial exploitation of the High Speed Line (HSL). During the experiment a few dozen trains circulated with speeds between 206 and 320 km/h in one HSL. The campaign start on 31/03/2017 and finished on 04/05/2017. The main goal of those measurements was to understand the effect produced by the insertion of soft rail pads between the rail and the sleeper. A portion of a LGV-EE (HSL between Paris-Strasbourg) received this type of component near the kilometric point 204. The analysis made in this section addresses the signals obtained during a HST passage. The french HST had also two setups of trains, one composed by one simple unit and the other configuration composed by two simple unit creating a multiple unit.

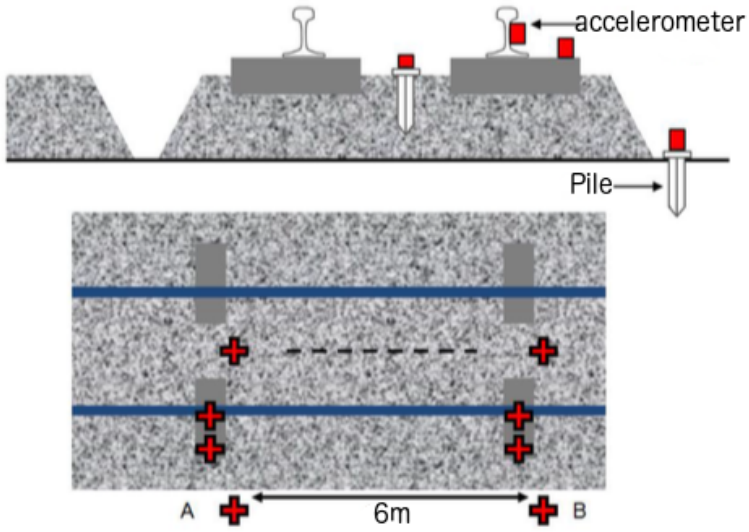

FIGURE 4.20: Experimental setup position of the accelerometers used in the measurements. The eight sensors placed at: the tail; sleepers; ballast; and soil. The upper image shows the cut plane $x-y$, and the lower figure shows the $x-z$ plane.

We would like to stress that this data was collected not in the framework of this thesis. Also, this initial analysis was developed mainly during the MSc project of Hadrien Pinault, who is now a PhD student at Arts et Métiers ParisTech, funded by SNCF Réseau. This data is object of the thesis of Patryk Dec now, student at CentraleSupélec and funded by SNCF Innovation & Research. Finally, for intelectual property reasons all the data present here were normalized between 0 and 1.

4.2.1 Experimental setup

The measurements were made through eight triaxial accelerometers. They were distributed as follows: two in the middle top of the ballast layer (using a metal pile); two on the sleepers; two in the middle of the rail web; and two near the ballast in the soil (using a metal pile). Fig. 4.20 shows a schematic view of this setup. Two lines of sensors were identified "A" and "B", they are distant of 6 m.

The measurement campaign recorded 237 trains in total. However, in this thesis only 148 measurements were analyzed. This dataset was chose because during this period the track does not suffer any kind of maintenance operation. The railway track received, during the test, french HST (TGV) and german one (ICE3). Three histograms to summarize the type of the train speed, they can be found in the Fig. 4.21.

4.2.2 Recorded data

All the three components of the acceleration for the 148 train passages were recorded. One set of measurements made for a simple unit TGV travelling at 302 km/h is plotted in the Fig. 4.22, to Fig. 4.25. The spectrum responses at the accelerations in the accelerometers placed at the rails are shown in Fig. 4.22. In the time domain the presence of the 11 packages corresponds to the 11 bogies of this TGV. A high level of acceleration was observed in the longitudinal acceleration. Regarding the frequency spectrum, the highest magnitudes are around 0.35. Comparing the sensors A and B, an unexpected result is found. The sensor A present the main component of the vibration in the longitudinal axis while the sensor B has

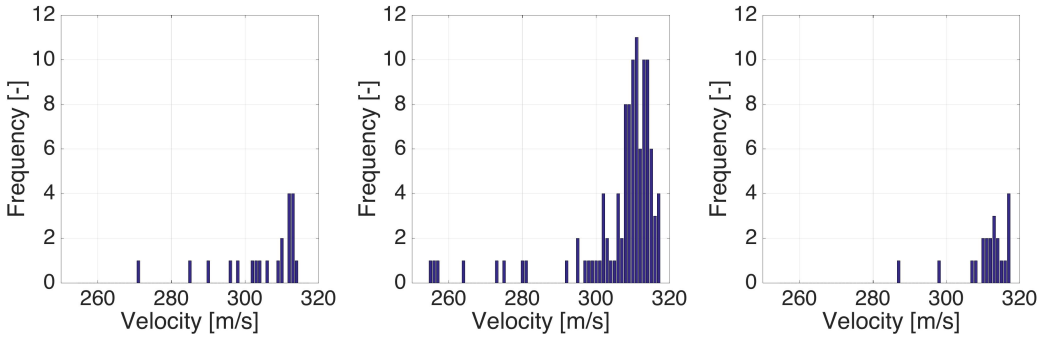

(a) ICE3 (b) TGV: Simple unit (c) TGV: Multiple unit

FIGURE 4.21: Histogram of the train passages velocities during the measurement campaign.

in the vertical direction. This might be due to a wrong labelling of the sensors in sensor A on the rail and it appeared for almost all analyzed signals. Additional information about the track and the experimental condition should be explored to better understand this behaviour identified.

The spectrum responses at the acceleration in the accelerometers placed at the sleepers are shown in Fig. 4.23. The time domain records show a reduction in the vibrational level (compared with the acceleration in the rail) and the predominance of the vertical vibration. Most of the energy was dissipated in the fastening system (especially in the rail pad). The 11 bogies are still present in the records. The frequency spectra show that the vertical components concentrate the energy around 0.32 and 0.47, for sensors A and B, respectively. This is probably a consequence of a slightly different position of the sensors A and B on their respective sleeper. The sensor B presents some longitudinal and transversal vibration around 0.15 with some considerable energy, which is also present in sensors A at lower levels.

The spectrum responses at the acceleration in the accelerometers placed at the ballast layer are shown in Fig. 4.24. There is presence of the 11 bogies in the records. The time history of the records shows an equivalence acceleration level for the 3 components, behaviour that was not present in the rail and sleepers. The heterogeneous nature of the ballast probably scatter the vibration, changing the energy from the vertical component to the other components. The frequency spectrum shows that the energy that reached the accelerometers contains only frequencies below 0.2.

The spectrum response of the acceleration in the accelerometers placed at the ground are show, in Fig. 4.25. The time records show a very small amplitude. The vertical component completely lost its predominant character. The energy still concentrates in the low frequencies.

As summary: the main component of the train load, the vertical one, is transmitted through the rail to the sleepers passing into the fastening system and ballast, finally the energy is dissipated before it reaches the ground. The vibrational level decreases from the rail to the sleeper, sleeper to the ballast, and ballast to the soil. This global behaviour was observed in all the measurements. The high heterogenous characteristic of the ballast layer produces a depolarization of the vibration, splitting energy from the vertical direction to all directions. The spectral content was filtered, especially the high frequencies components in the fastening system and ballast, so that only low frequencies reach the ground.

To better understand the global behaviour of the ballast three additional comparisons are proposed. The first stresses the influence of the type of the train in the frequency response. The second one consists in the influence of the speed of the trains, finally the influence of

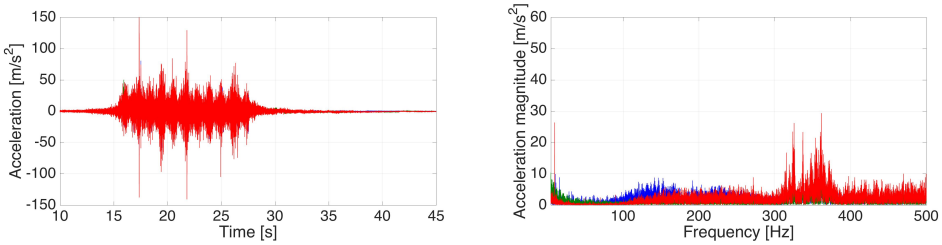

(a) Acceleration time history: sensor A.

(b) Acceleration vs. frequency: sensor A.

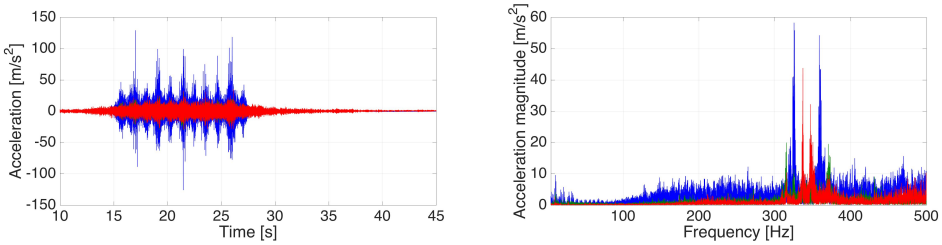

(c) Acceleration time history: sensor B.

(d) Acceleration vs. frequency: sensor B.

FIGURE 4.22: Acceleration records for the rail. The blue line is the vertical acceleration component; the green line is the transversal acceleration component; and the red one is the longitudinal acceleration component.

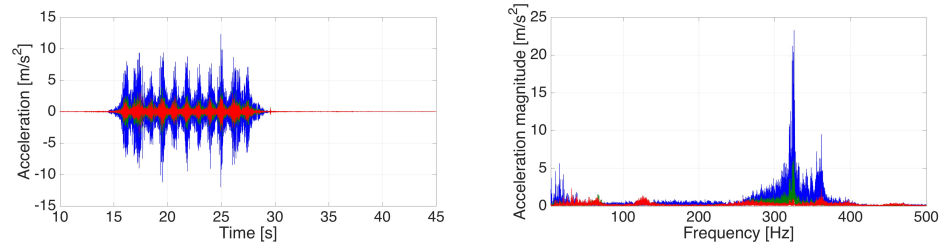

(a) Acceleration time history: sensor A.

(b) Acceleration vs. frequency: sensor A.

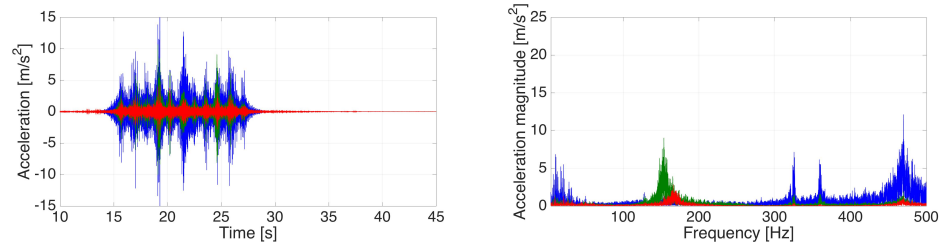

(c) Acceleration time history: sensor B.

(d) Acceleration vs. frequency: sensor B.

FIGURE 4.23: Acceleration records for the sleepers. The blue line is the vertical acceleration component; the green line is the transversal acceleration component; and the red one is the longitudinal acceleration component.

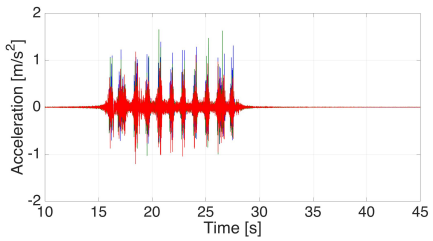

(a) Acceleration time history: sensor A.

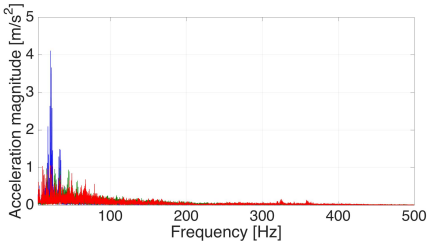

(b) Acceleration vs. frequency: sensor A.

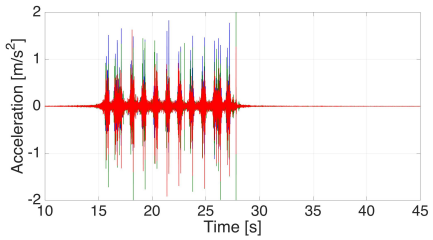

(c) Acceleration time history: sensor B.

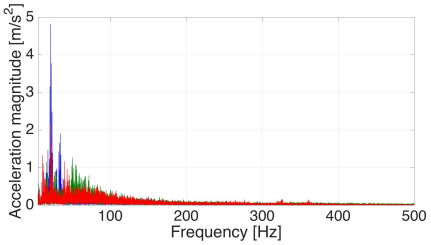

(d) Acceleration vs. frequency: sensor B.

FIGURE 4.24: Acceleration records for the ballast. The blue line is the vertical acceleration component; the green line is the transversal acceleration component; and the red one is the longitudinal acceleration component.

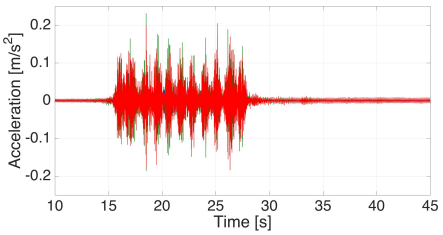

(a) Acceleration time history: sensor A.

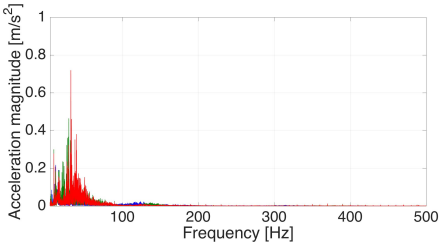

(b) Acceleration vs. frequency: sensor A.

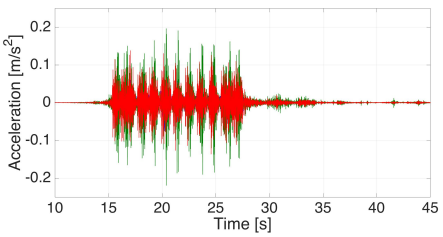

(c) Acceleration time history: sensor B.

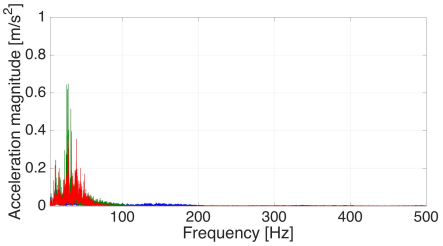

(d) Acceleration vs. frequency: sensor B.

FIGURE 4.25: Acceleration records for the soil. The blue line is the vertical acceleration component; the green line is the transversal acceleration component; and the red one is the longitudinal acceleration component.

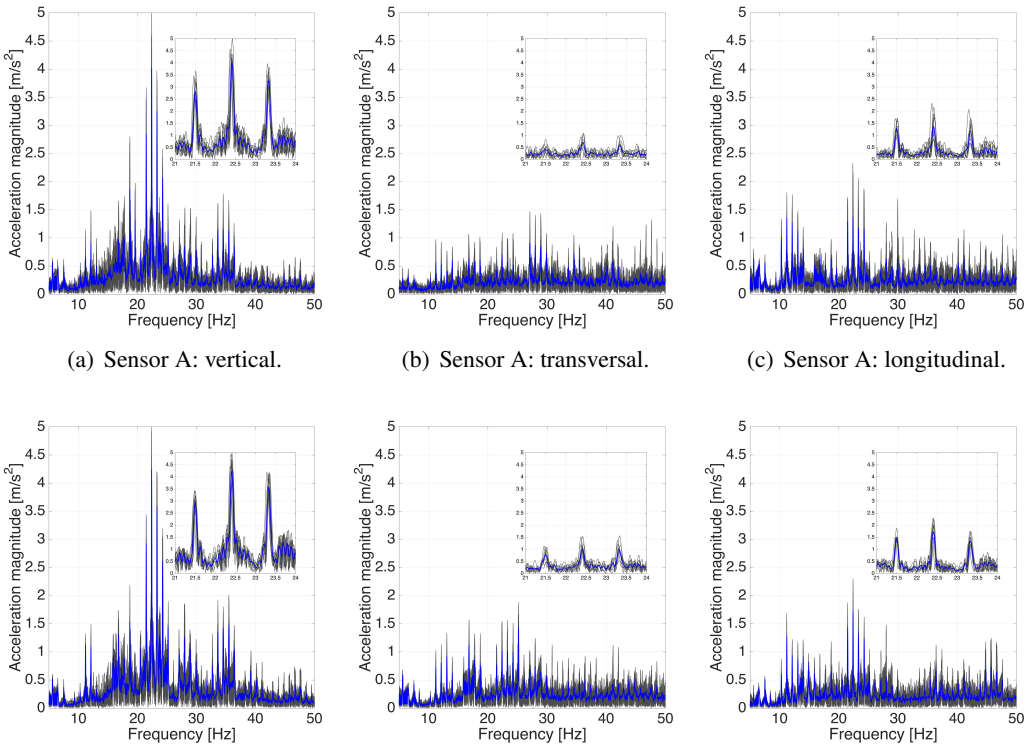

(a) Sensor A: vertical. (b) Sensor A: transversal. (c) Sensor A: longitudinal.

(d) Sensor B: vertical. (e) Sensor B: transversal. (f) Sensor B: longitudinal.

FIGURE 4.26: Acceleration spectrum magnitude of 9 trains passagens, gray line, the blue line represents the mean between the values. The upper line corresponds to the vertical, transversal, and longitudinal accelerations for the sensor A. The second line shows the same quantities for the accelerometer B.

the monitor position is studied. For conciseness only the signals collected in the ballast will be shown hereafter. A smaller frequency range is also considered, between 0.005 and 0.05, to better visualize the data. Before, the repeatability of the ballast acceleration spectrum is considered.

Repeatability of the ballast acceleration spectrum

In order to check the repeatability, one train speed is selected and analysed. The frequency spectrum response of 9 trains (simple unit) passing at 314 km/h during 4 weeks are presented in Fig. 4.26 in gray solid line. The blue solid line represents the mean between the trains passages. The upper line corresponds to the vertical, transversal, and longitudinal accelerations for the sensor A, the lower line for the sensor B. The insert in each figure presents the same quantities in a specific range (the most energetic), between 0.021 and 0.024. The 9 trains recorded present a very similar acceleration spectrum, even though they are not equal (different number/distribution of passengers, suspension, wheels, ballast condition, and so on). The inserts show that the mean value can represent the global behaviour of the trains, and improve the signal/noise ratio. So, the mean value is used in the forthcoming analyses.

Influence of the type of the train in the ballast response

As said before, two types of trains were recorded: the TGV; and the ICE3. The construction of those trains is different, with different weights, distance between wheels, suspension

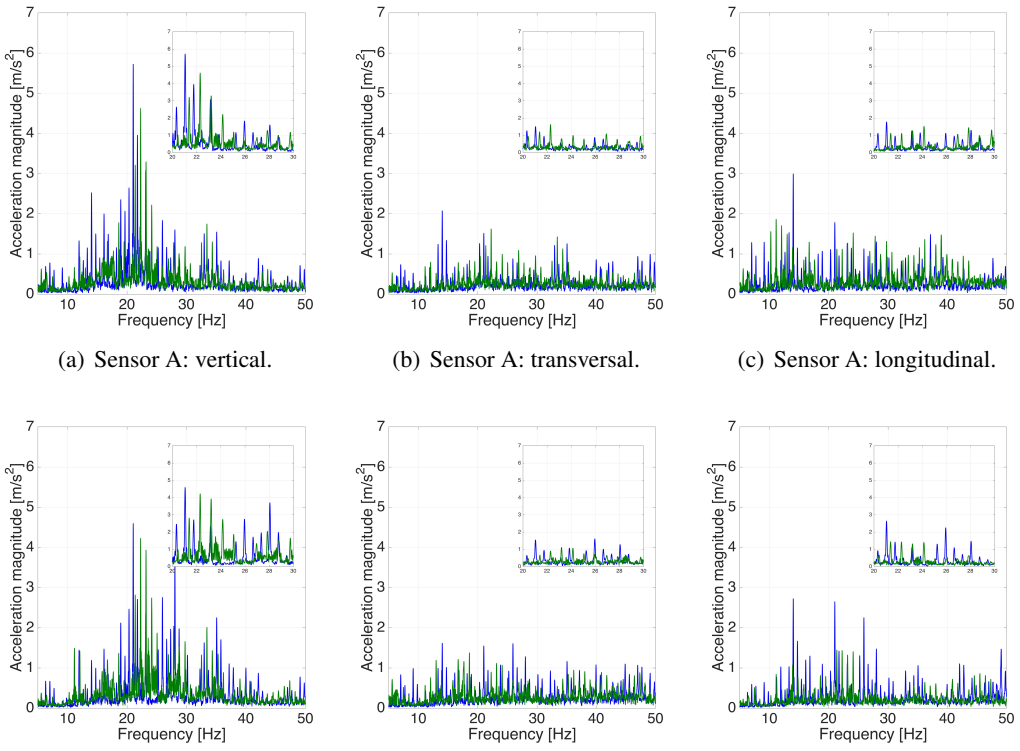

(a) Sensor A: vertical. (b) Sensor A: transversal. (c) Sensor A: longitudinal.

(d) Sensor B: vertical. (e) Sensor B: transversal. (f) Sensor B: longitudinal.

FIGURE 4.27: Comparison between the spectrum response of the French and German HST. The green lines represent the TGV while the blue ones the ICE3. The upper line corresponds to the vertical, transversal, and longitudinal accelerations for the sensor A. The second line shows the same quantities for the accelerometer B.

response, driving system. Fig. 4.27 presents the mean acceleration frequency spectrum for the ICE3 trains in a blue solid line and TGV in a green solid line. In total, 3 trains for each configuration were recorded at the same velocity of 312 km/h. As the number of passages of the train ICE3 is quite low (15% of the records) the next section is dedicated to the analysis of the TGV.

The amplitude acceleration response for a passage of a simple unit and a multiple unit for the velocity of 318 km/h is shown in Fig. 4.28. The blue line corresponds to the multiple units train and the green line the simple unit train. As can be seen in the inserts a quite good agreement in the amplitudes were found. However in other regions the match in the amplitudes was not so good, as expected. Using this result the simple unit passages cannot be mixed with the multiple unities train passage in subsequent analyses.

Influence of the train speed in the ballast response

The influence of the train speed in the wavelength spectrum response is presented in Fig. 4.29. In this plot three different train velocities Were analyzed, with trains going at 302 km/h (blue line), 310 km/h (green line), and 318 km/h (red line). Since the trains have the same geometry, driving system, and a very similar suspension system, a linear increase in the frequency would be expected when the speed increase. In this figure the axis of the abscissa was modified to the wavelength instead of the frequency. This change shows that the influence of velocity is entirely taken into account through this linear rescaling of the wavelength.

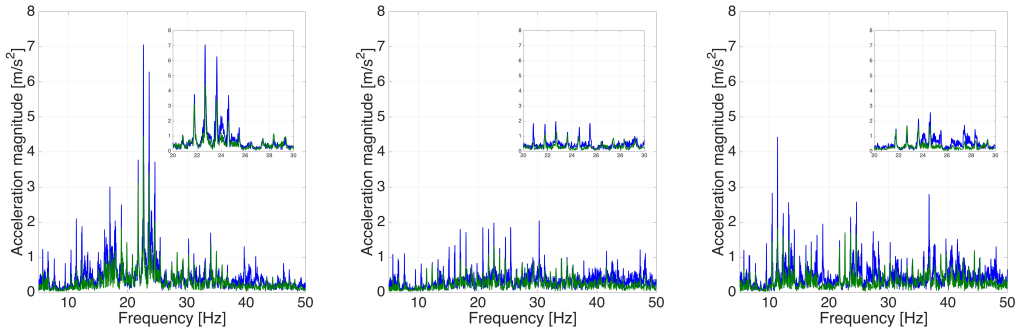

(a) Sensor A: vertical. (b) Sensor A: transversal. (c) Sensor A: longitudinal.

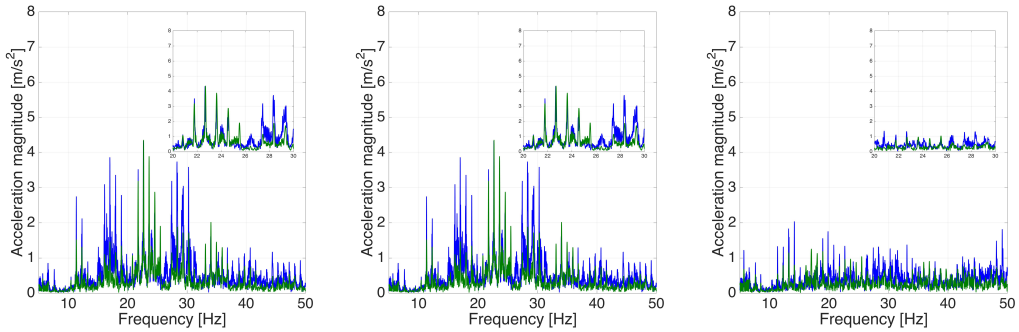

(d) Sensor B: vertical. (e) Sensor B: transversal. (f) Sensor B: longitudinal.

FIGURE 4.28: Influence of the train type in the amplitude acceleration response.A passage of a simple unit is represented by the green line and a multiple unit by the blue line for the train velocity of 318 km/h.

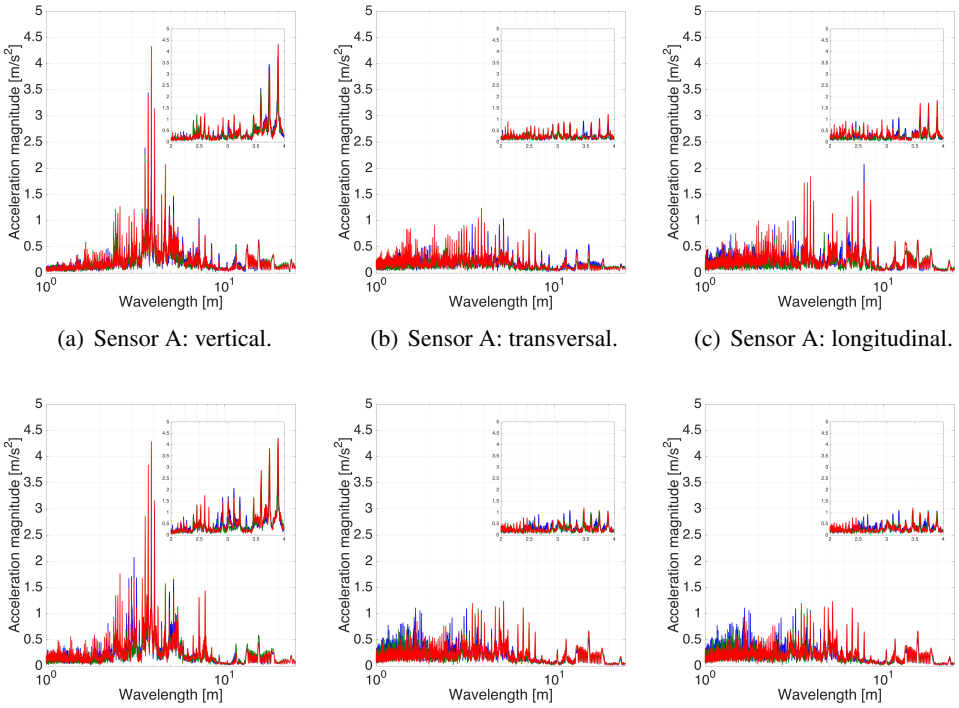

(a) Sensor A: vertical. (b) Sensor A: transversal. (c) Sensor A: longitudinal.

(d) Sensor B: vertical. (e) Sensor B: transversal. (f) Sensor B: longitudinal.

FIGURE 4.29: Influence of the train speed in the wavelength spectrum response of the acceleration in the ballast layer. The blue line is the train at 302 km/h, the green line at 310 km/h, and the red line at 318 km/h.

4.3 Concluding remarks

In this chapter two datasets were analysed. The ballast box experiment allows the study of FRF. The measurement campaign of acceleration put in evidence the acceleration frequency spectrum shift (to the high frequency) when the train speed increases, and the difference between train type that passed in this HSL. The filter effect of each component of the ballasted railway track was also stressed. The rail-pad/sleepers contribute to reduce the high frequencies, once the wave enters the ballast, it ends up being depolarized with a reduction of the amplitude of the vertical acceleration. The geometric effect contribute, also, for the amplitude reduction of the acceleration.

The velocities evaluated for the medium in the ballast box in this chapter present a huge discrepancy between them. This discrepancy is linked with the fact that they refer to different velocities. The first values of the velocity are higher. This measurement is the direct wave from the source to the sensor. It is affected only by the small path between source and sensor, normally some grains (4 or 6 grains, more or less). On the other hand, the vibration analysis showed a very slow velocity. It is expected because the wave is traveling in all the domain, not only in a few grains, in other words, it refers to a homogenized velocity. As discussed, in Chapter 3, the apparent velocity is lower than the average velocity [29]. However, a deeper study should be applied to the vibration data in order to understand why such a low velocity. This will be performed on the basis of wave propagation simulations using the model of Chapter 2.

Chapter 5

Conclusion and perspectives

In this thesis, we introduced a novel approach to model the behavior of the ballast during the passage of trains on ballasted railway tracks. The model we proposed is a randomly-fluctuating stochastic heterogeneous continuum model. It is intermediate between homogeneous continuum models that cannot reproduce the complex dynamical behavior of realistic tracks, and discrete models that are difficult to simulate at the appropriate scale for dynamic analyses. The randomly-fluctuating Young's modulus, presented in Chapter 2, proved to be a good alternative to discrete models to predict the stress distribution in ballast samples in statics. The stress components directly used in the cost function of the inverse problem, as well as those that had not been used, all proved to be accurate. Notably, these results were achieved for a simple linear elastic isotropic, although heterogeneous. No non-linearity or non-locality were introduced in the model.

The study of the impact of the proposed model in the wave propagation in ballasted railway tracks was performed in Chapter 3. The dispersion curve of the ballasted railway track showed a tremendous influence of the heterogeneity (with the higher frequency waves going slower than lower frequency waves). Above 100 Hz, the waves remain localized in the vicinity of the source through Anderson localization. Although very widely studied in the physics literature, this phenomenon has been studied in the acoustical literature only from the experimental point of view, which tries to discriminate between dissipation and localization in measurements [110]. Additional simulations in unbounded media proved that the observation of localization in the ballast layer was not related to the particular geometry of the layer, but indeed Anderson localization.

Finally, in Chapter 4, experiments in a ballast box and in a real segment of ballasted HSL were explored. Two methods were used to estimate the velocities in the ballast box. The result velocities appear very different, but this is compatible with theory on wave propagation in heterogeneous media, where local velocities may be much larger than homogenized velocities. As the difference is very large, further investigations should however be considered. In particular, simulations of propagation in the randomly-fluctuating ballast should be proposed, at short times as well as at later times, when modal behavior hits in. The campaign of acceleration measurements made during the passage of commercial trains was also presented. The inverse problem still has to be constructed, and the obtained velocities compared with those of the ballast box. Note however that differences may be expected, in particular because of the lack of compression in the ballast box.

Although the first results are extremely encouraging, several aspects of the model should be improved. The small discrepancy observed in shear stress in Sections 2.2.2 and 2.3 should be investigated, by considering for instance another first-order marginal law with different behavior for smaller-than-average stresses.

Only Young's modulus had its parameters estimated using an inverse problem, whereas it might be more appropriate to estimate all the mechanical properties. The model could be extended to an entire constitutive tensor being random, possibly introducing anisotropy [245],

and certainly considering constitutive non-linearities [121] for dissipation, fatigue and modeling of long-term behavior of the track. Long-term behavior and degradation of the ballast grains may be partially taken into account also by evolving the average diameter of the grains, which is a parameter of the correlation model. Pressure-dependence of the velocity in granular media [169, 151, 127] is a well-documented phenomenon, that might be reproducible within our model, either though an ad-hoc non-linear relation, or more interestingly by playing with compacity (which is a parameter of the correlation model) or by making the model non-homogeneous (in the statistical sense). Another known limitation of our heterogeneous randomly-fluctuating model is that it cannot deal with re-arrangements of grains [143]. Notwithstanding these limitations, we believe that it can be a first building block towards improving ballasted railway tracks, providing insight into a physical phenomenon of Anderson localization previously disregarded.

To look a little bit further ahead, the results presented in Chapter 3 indicate that the ballast layer is a very efficient wave trap. It seems capable to impede propagation of waves whose wavelength is rather large with respect to the thickness of the ballast layer. Anderson localization might therefore be a good ingredient to consider for vibration isolation purposes. A master student is currently considering this option to reduce the impact of railway-induced ground vibration on the buildings close to the tracks.

Appendix A

Generation of hexahedral mesh following geophysical features

The results presented in this appendix were made in collaboration with Professor Alvaro Coutinho and José Camata from NACAD/UFRJ - Núcleo de Atendimento a Computação de Alto Desempenho - Universidade Federal do Rio de Janeiro. This collaboration is a CAPES-COFECUB (Brazilian and French research promotion agency) joint project. NACAD is a laboratory that focuses on High-Performance Computing (HPC), working on efficient mesh generation algorithms, adaptive meshes, adaptive time step, in-situ visualization, and many others HPC subjects. This collaboration resulted in several publications in conferences, and one journal article is in preparation.

A.1 Scalable parallel mesher for geophysical applications

Research effort has been devoted to the development of high performance schemes for large scale wave propagation. Solvers can now scale efficiently over very large clusters [33, 131, 115]. The pre- and post-processing steps have not necessarily followed the same pace. Although various techniques and algorithms have been developed [56], octree-based meshing has recently demonstrated improved capabilities for scaling over today's largest machines [254, 244, 46, 49, 95, 118]. Recent advances in in-situ visualization showed the capability to deal with a huge amount of data, and scalability of the post-processing. The scalability of the entire wave propagation workflow is limited by its slowest link, thus the development of a scalable hexahedral mesher able to deal with larger meshes (e.g. geophysical meshes) is essential.

Meshing is particularly hard considering high-resolution wave propagation problems using conformal hexahedra in realistic Earth geometries [56]. Here, high resolution means meshes containing several billions of elements. For such large meshes, octree-based algorithms seem to be particularly successful [46, 49]. Octrees are spatial data structures used in various problems in computer science and engineering, e.g., object representation, image analysis and unstructured meshing [208]. Standard octrees divide a cell into eight new cells [270, 175, 176]. However, it has been shown that a 3-octree [182, 119], defined as a data structure where a cell is divided into 27 new cells [220] is more suitable for hexahedral mesh generation. Reviews about the subject can be found in [247, 227].

For wave propagation problems, the main parameter controlling the size of the elements is the wave velocity. In geophysical problems, there is on average a gradient of this velocity with depth, with lower velocities closest to the surface of the Earth. In this first step of our procedure, we, therefore, aim at constructing a mesh where the elements are homogeneous along the horizontal planes and are larger in depth than close to the surface. One exemple is present in Fig. A.1. The construction must also avoid hanging nodes. The procedure to create the hexahedra starts with the finest cells, and every m meters a transition layer is introduced.

This layer is composed of cells shown in Fig. A.5 (and based on [203]), that allows reducing the size of the elements between two layers. The whole process is done in parallel. The ghosts elements share the information (global identification) between processors through an MPI protocol [89]. The domain is initially partitioned in a 2D grid among processes, and the construction is done independently by each process, as can be seen in Fig. A.2. The output of this step of the construction is a structured mesh.

In order to represent realistic Earth geometries, a smooth scheme [221] is used to fit the octree mesh with a surface triangulation (STL) generated from SRTM3 topography data [84] sampled at 3 arc-seconds, and obtained from United States Geological Survey [232]. This STL file includes the topography (inland heights) and the altitude is set to zero over oceans and seas. Fig. A.3 shows a mesh of the Kefalonia region in Greece and an image obtained from Google Maps of the same region, approximately. The output of this step of the construction is still a structured mesh, but with deformed elements.

Realistic meshes of the Earth must also include the representation of the bathymetry, as well as various materials interfaces [269] inside the Earth (e.g. basins inducing strong site effects, Moho discontinuity, or others). With respect to the mesh constructed at the previous step, the bathymetry can be seen as material discontinuity (between solid and fluid) so we only describe in this paper the inclusion of bathymetry. The bathymetry is defined through an STL surface, constructed from the SRTM30_PLUS model [37], a 30-arc second resolution global topography/bathymetry grid obtained from Scripps Institution of Oceanography, University of California San Diego [233]. This STL surface is defined on a regular grid and is modified in the following manner: nodes at vanishing altitude are added along the coastline, using the information stored in the SRTM water body database [240], and inland nodes are removed. A 2D Delaunay triangulation is then used to construct a new STL containing only the fluid-solid interface. Other types of material or interface discontinuity can be treated similarly, through the definition of an appropriate STL file. The intercepted elements are refined following the approach proposed by Ruiz [203], then the nodes are moved to the bathymetry surface.

Some of the hexahedra constructed at the previous step are intercepted by the STL surface. For the final mesh to conform to the material interface, these hexahedra should be further divided. All the 256 possible types of intersection, by symmetry considerations, can be reduced to 15 cases [133]. Fig. A.4 shows all the 15 possibilities. Some of those elements can be easily divided into new hexahedrons, without hanging nodes (like templates 3, and 9). However, the complexity for some of then (templates 6 and 10, for example) turns this simple geometrical problem in a very hard problem to answer using templates. As suggested by Kudela *et al.* [133] the application of an octree refinement, at this time making the projection of the nodes in cut surface, can be one way to overcome this problem. On the other hand, the presence of hanging nodes still a problem. To overcome the new hanging nodes in the mesh, the transitions templates as those proposed by Ruiz [203] can be used, Fig. A.5 presents them. Moreover, the refinement level of this mesh could be controlled by the user in different regions of the domain. A simple example was presented in Fig. A.6, where the templates proposed by Ruiz [203] were used to refine a region and remove hanging nodes. One example is present in Fig A.7 and Fig A.8. Kashiwazaki coastal region in Japan was discretized with 18M elements. The bathymetry surface was used to reproduce a realistic interface between water and soil. The blue elements represent the water, the brown ones represent the soil.

The mesh quality is a critical parameter for the accuracy and efficiency in the solution of Partial Differential Equations using numerical methods, like wave propagation phenomena. After the entire process, some elements with low quality can be generate. The MESQUITE library [44] may be used to relocate vertices and improve the mesh quality.

A.2 Weak scalability analysis

We perform a weak scalability analysis of the parallel mesh generator on Occigen for a mesh of the Kefalonia region in Greece (between N 38°00'00 E 20°00' and N 39°00' E 21°00') in a cube of approximately 110×110×110 km^3. Fig. A.9 shows the final mesh considering 8 levels of refinement and 4 transition layers. We analyse how the CPU time varies with the number of cores for a constant amount of data per core. In our analysis, this amount of data is defined by the number of elements resulting from the meshing algorithm. Table A.1 shows the growth in problem size according to the number of cores. Note that, for each increase in the octree refinement level, the mesh size grows by a factor of 9, reaching 62 billions of hexahedra at level 10. Table A.1 also presents the overall CPU time (in seconds) for runs instrumented by TAU performance analysis system [226, 246] on Occigen, using its standard configuration on this system. Although the run time increases almost 3 times when refinement levels increase from 7 to 9, note that, for each level, the mesh size grows by a factor of 9, while the number of cores increases only by a factor of 3. From 9 to 10 refinement levels, we observe that both the mesh size and cores grow by the same factor. In this case, the additional refinement level increases run time in about 20%. Table A.1 also reveals that increasing the number of octree levels does not increase the computation/communication ratio, which stays below 30%.

TABLE A.1: Weak scaling of the mesh generation for the Kefalonia region in Greece.

Cores	Levels	Nodes	Elements	Time (s)	Comm(%)
81	7	85,602,744	83,102,679	12.061	21 %
243	8	769,790,232	747,937,476	32.994	20 %
729	9	6,926,153,724	6,731,438,013	105.188	25 %
6561	10	62,330,385,168	60,583,119,264	123.066	29 %

A.3 Examples of mesh generation

The final mesh is a non-structured hexahedral mesh, conformal to the topography, bathymetry and coastlines and with coarsening of the elements with depth. Two examples of meshes generated with the proposed scheme are presented in Fig. A.10 and Fig. A.11. These meshes were generated on Occigen (at CINES, France), a BULL machine equipped with 2106 computing nodes. Each Occigen node has two Intel Haswell (E5-2690) processor (12 cores per node), totalizing 50544 cores. The first example considers the Cadarache inland region in France (between N 43°48' E 4°30' and N 44°05' E 5°00') in a cube of approximately 40×32×35 km^3. There is no solid-water interface and the topography goes up to 276 m. The second example considers the Kashiwazaki coastal region in Japan (between N 37°10' E 138°15' and N 37°40' E 138°55') in a cube of approximately 59×56×55 km^3. The bathymetry goes down to 995 m and the topography up to 920 m. On both examples, the mesh grading with depth, as well as the features of the topography and bathymetry can be clearly seen.

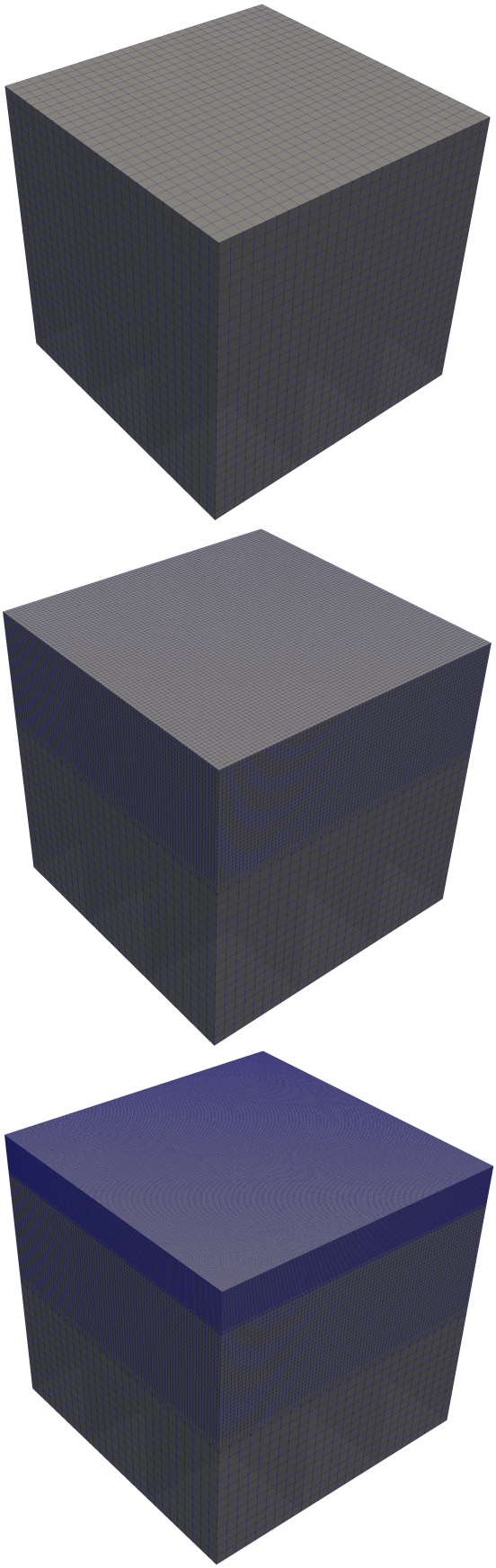

FIGURE A.1: Mesh refinement with the depth. From up to down: no refinement in the depth, one refinement level, and two refinement level

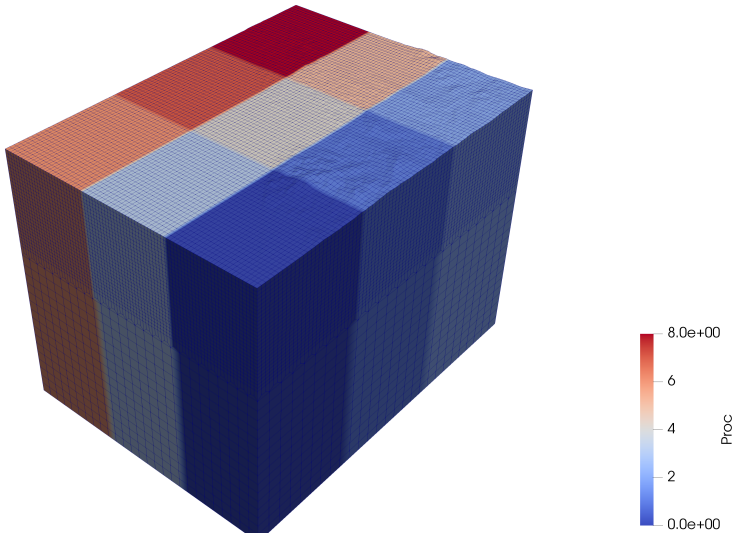

FIGURE A.2: Processors grid domain. The colour scale represents the processor associated to each element vertex.

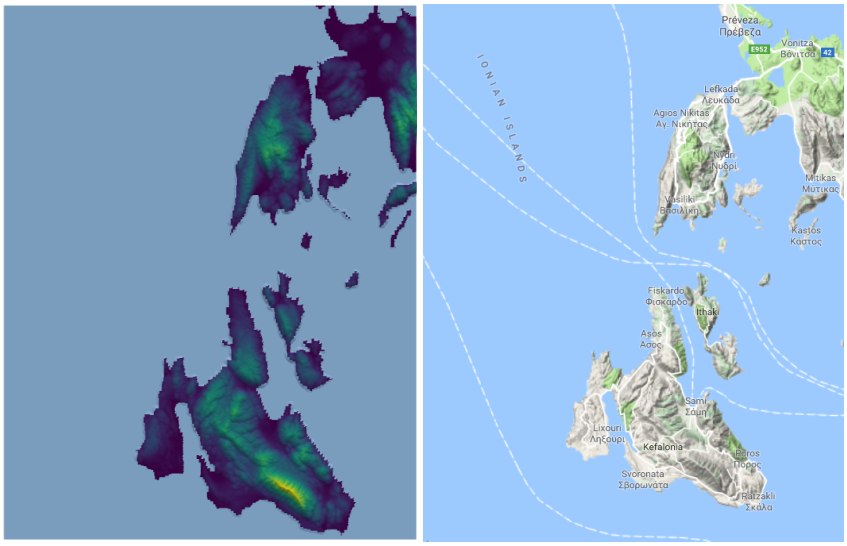

FIGURE A.3: Mesh of the Kefalonia region in Greece and a snapshot obtained from Google Maps of the same region

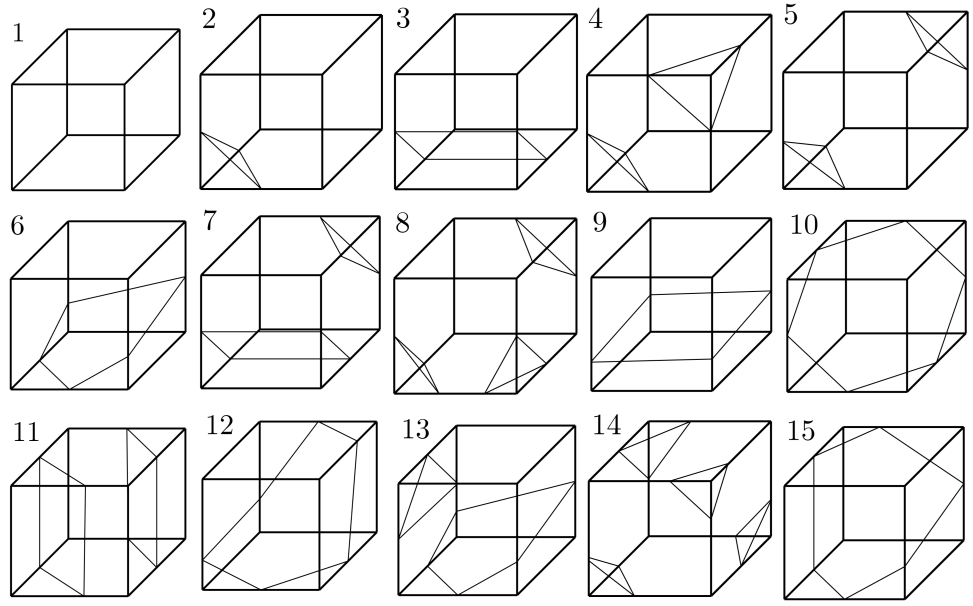

FIGURE A.4: Intersection of the cut surface in the hexahedra element, extracted from Kudela *et al.* [133]).

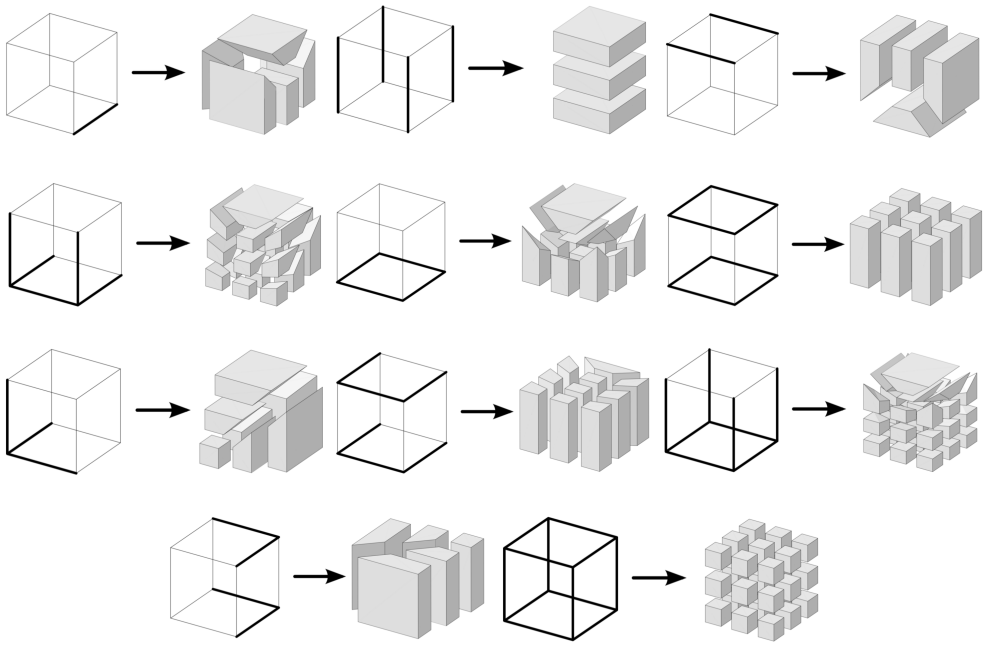

FIGURE A.5: Transition template for 27-trees, extracted from Ruiz [203].

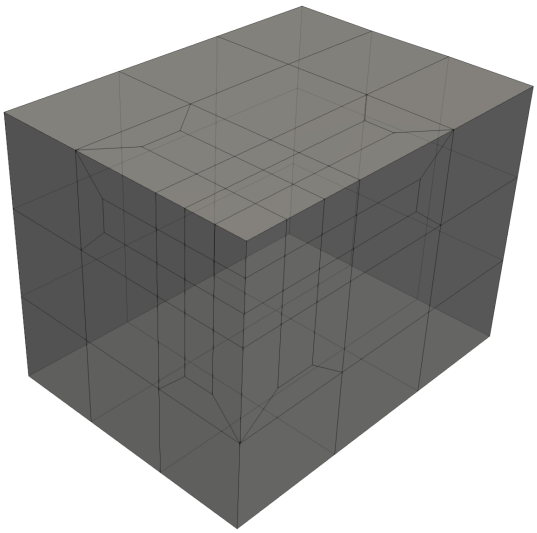

FIGURE A.6: Exemple of mesh refinement in a corner using 27-tree templates.

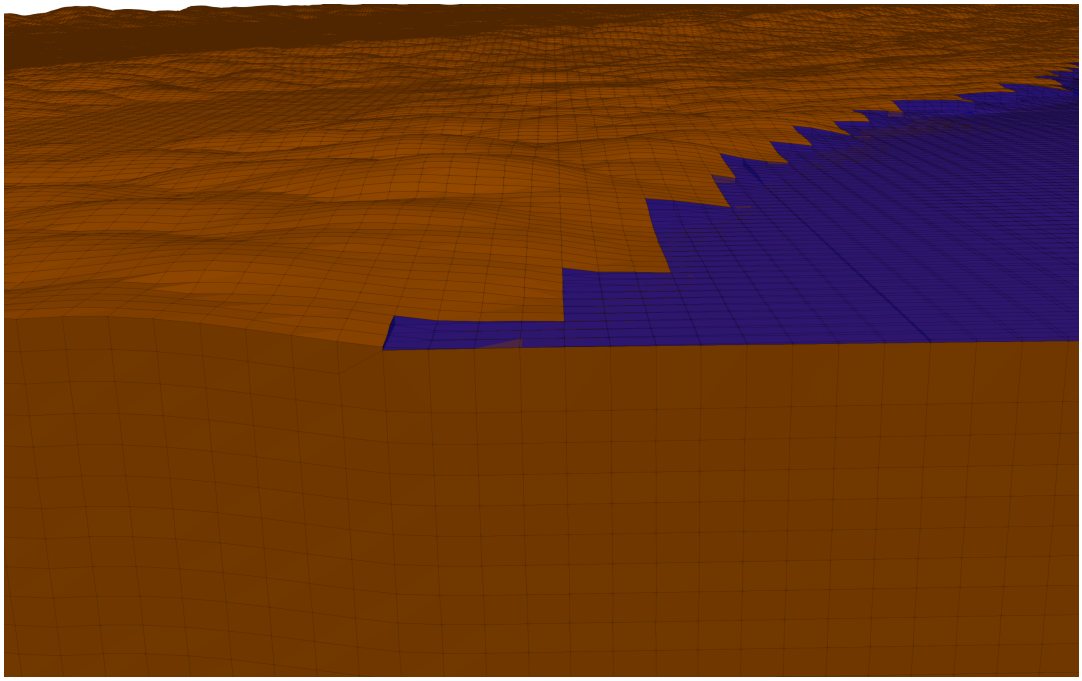

FIGURE A.7: Example of deformed mesh taking into account the bathymetry. In blue the elements that represent the water, the brown ones represent the soil.

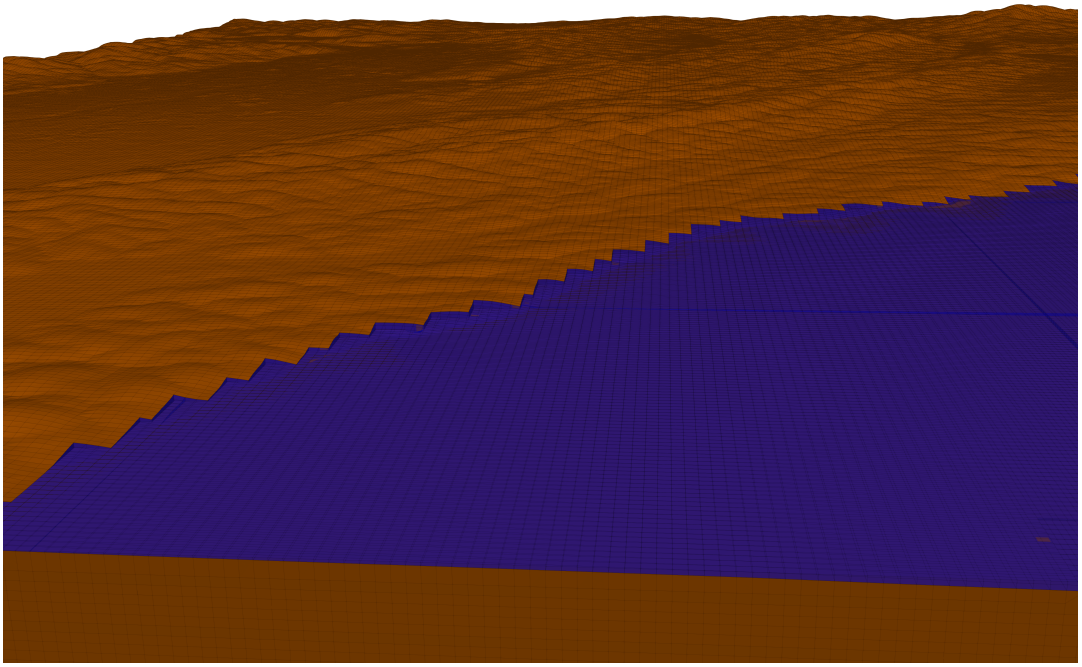

FIGURE A.8: Example of deformed mesh taking into account the bathymetry. In blue the elements that represent the water, the brown ones represent the soil.

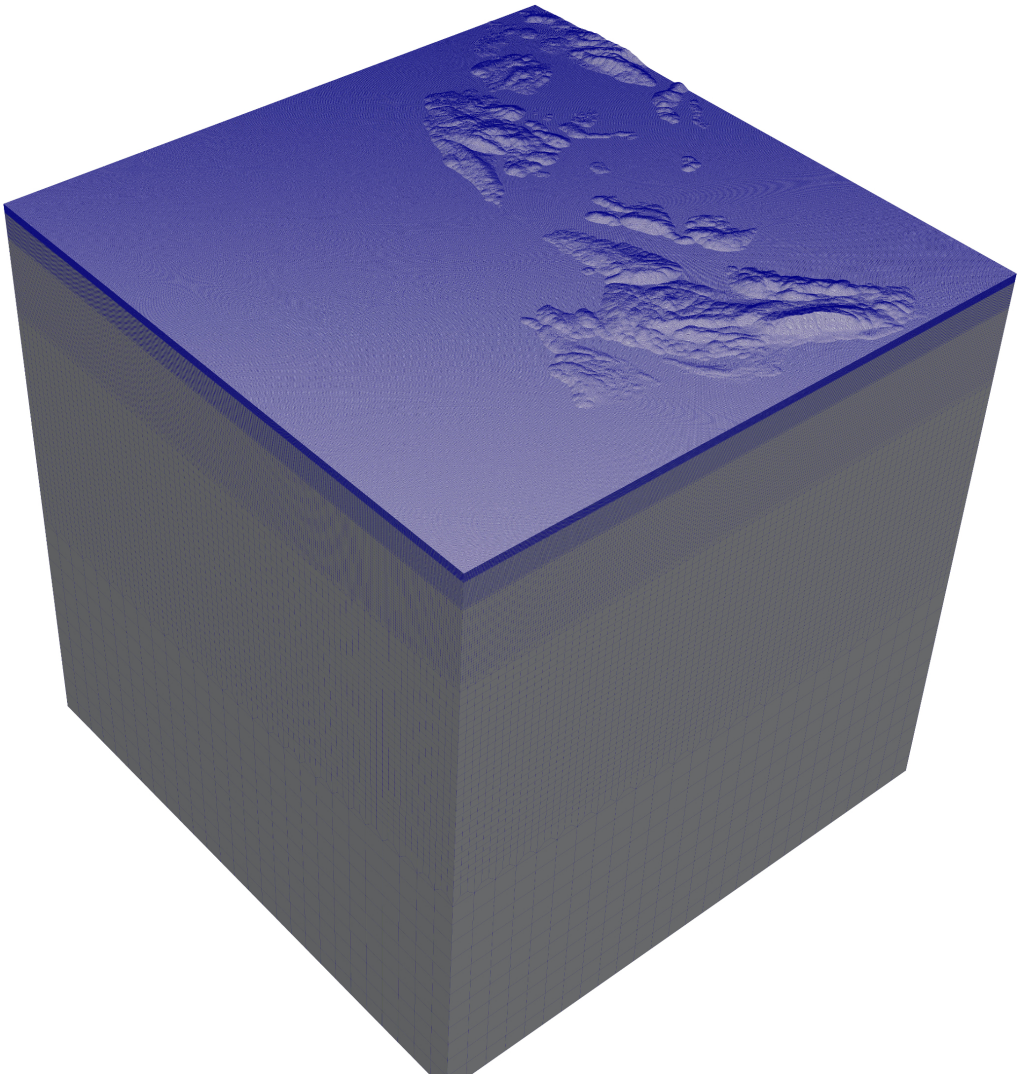

FIGURE A.9: Mesh of the Kefalonia region with 8 levels of refinement and 4 transition layers.

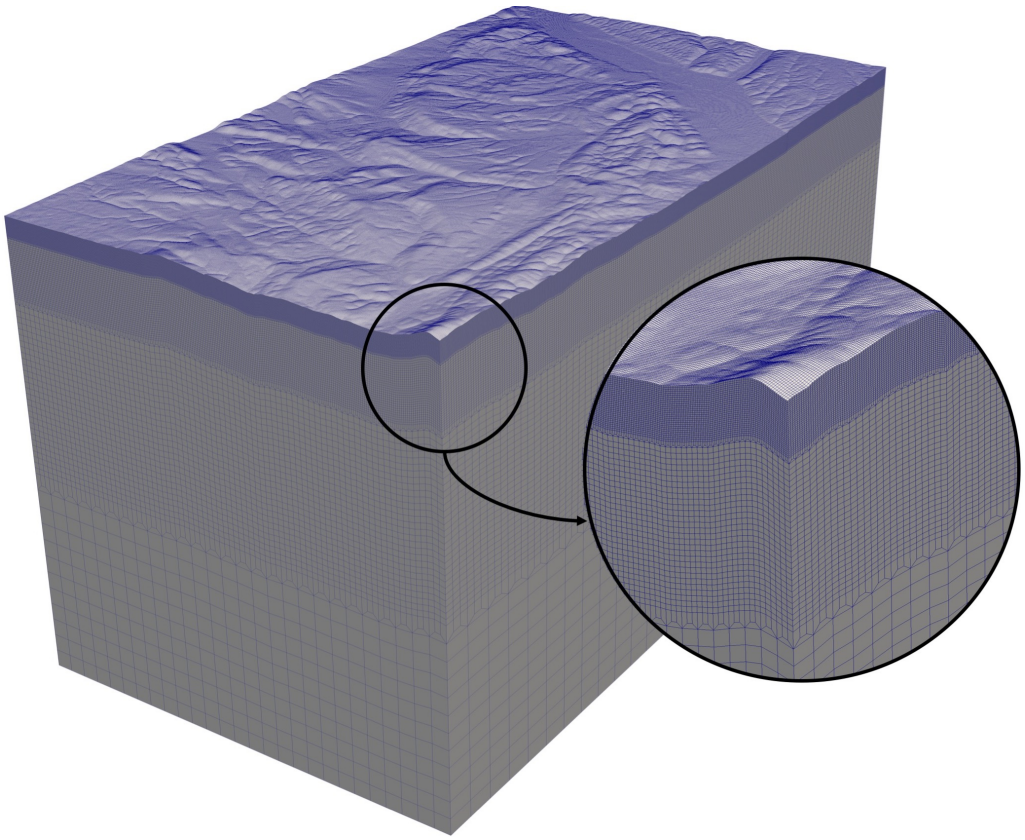

FIGURE A.10: Mesh of the Cadarache inland region in France.

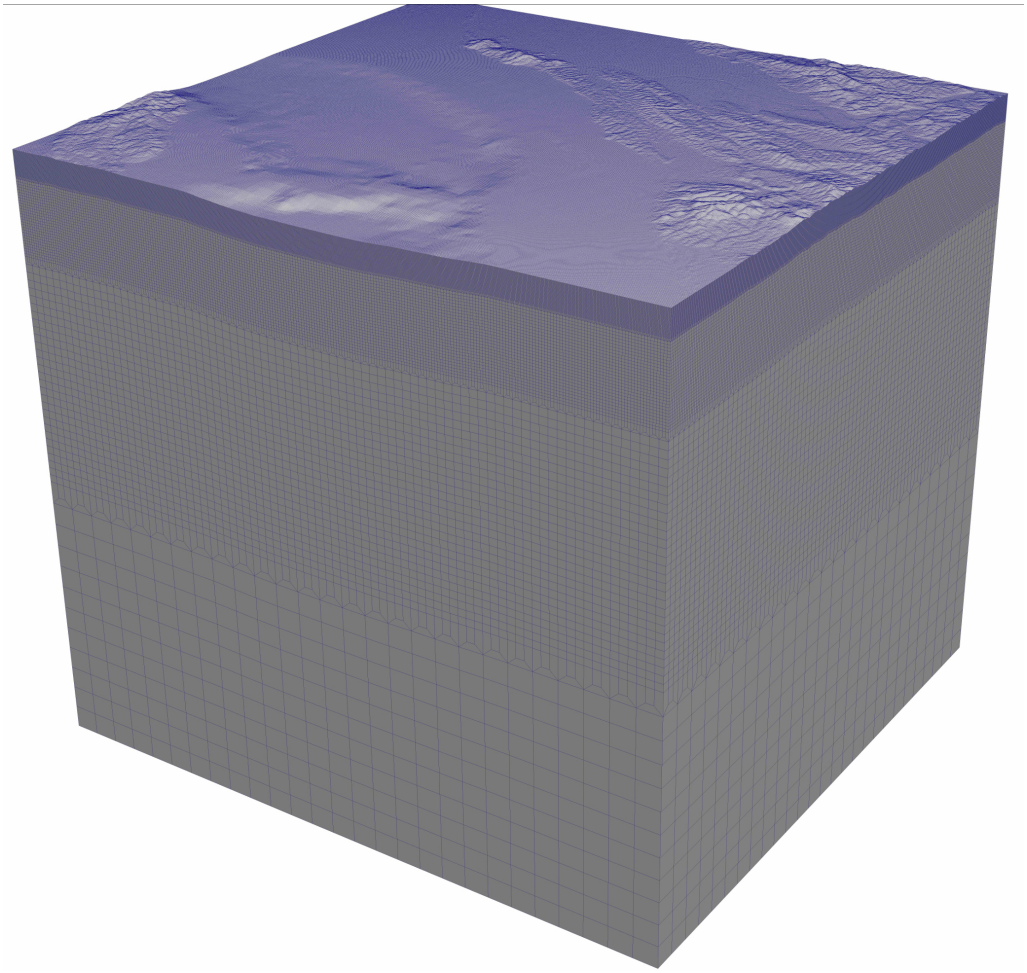

FIGURE A.11: Mesh of the Kashiwazaki coastal region in Japan.

Appendix B

Micromechanical Approach in Granular Materials

B.1 Equivalent stress in granular material

The Eq. (2.3) can be deduced using the contact forces and the Gauss theorem [52, 51, 132]. A "derivation" of this equation is repeated here. It consists in two steps: (i) the first step the average stress is evaluate on the contacts in the boundary that enclose the assembly of particles; (ii) the second step evaluate the average stress on the internal forces.

Considering an average stress, $\sigma^V_{\alpha\beta}$, in the volume, V, it can be written as:

$$\sigma^V_{\alpha\beta} = \frac{1}{V}\iiint_V \sigma_{\alpha\beta} dV, \tag{B.1}$$

using the Gauss theorem and consider the equilibrium equation: $\sigma_{\alpha\beta,\beta} = 0$, the average stress tensor is now expressed by:

$$\sigma^V_{\alpha\beta} = \frac{1}{V}\iint_S n_\iota \sigma_{\alpha\iota} x_\beta dS \tag{B.2}$$

where n_ι is the normal unit vector on the boundary, S, of the volume V, and the x_β is the vector that points to the contact between the particle (in the boundary).

Considering that this boundary does not cut any particle and passes only at contact points, the product $n_\iota \sigma_{\alpha\iota} dS$ represents all the forces applied at the contacts located on the boundary. The Eq. (B.2) is then rewrite as:

$$\sigma^V_{\alpha\beta} = \frac{1}{V}\sum_{c^*\in S} f^c_\alpha x^{c^*}_\beta, \tag{B.3}$$

this relation express the external contact forces acting in the surface S at $x^{c^*}_\beta$ on the boundary of V to the average value of $\sigma^V_{\alpha\beta}$ defined for the value V.

Performing a similar analysis of the Eq. (B.3) the equilibrium between the particle in the boundary S (particle A), and one particle inside of the surface (particle B) follows the relation:

$$\sum_B f^{AB}_\alpha = 0. \tag{B.4}$$

where f^{AB}_α represents the contact force exerted by the particle B on particle A, see Fig B.1.

Then:

$$\sum_A \sum_B f^{AB}_\alpha x^A_\beta = 0, \tag{B.5}$$

where x^A_β is the center of mass of the particle A.

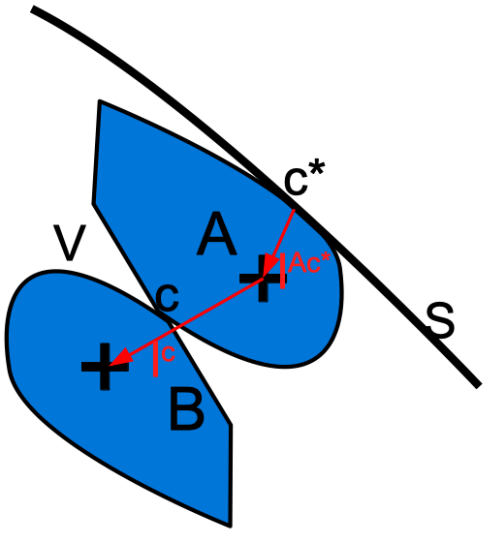

FIGURE B.1: Schematic representation used in the equivalent stress in discrete model.

For each boundary contact c^* with particle A:

$$x_\beta^A f_\alpha^{Ac^*} = \left(x_\beta^{Ac^*} - \ell_\beta^{Ac^*}\right) f_\alpha^{Ac^*}, \tag{B.6}$$

where $\ell_\beta^{Ac^*}$ vector that connect the center of mass of A to the boundary contact point located at $x_\beta^{Ac^*}$.

For each contact between the particles A and B two terms will appear in the summation Eq. (B.5):

$$x_\beta^A f_\alpha^{AB} + x_\beta^B f_\alpha^{BA} = f_\alpha^{c^*} \ell_\beta^{c^*} \tag{B.7}$$

with: $f_\alpha^{c^*} = f_\alpha^{AB} = -f_\alpha^{BA}$ and $\ell_\beta^c = \overrightarrow{AB}$

Considering the relation Eq. (B.7) on internal contacts and the relation Eq. (B.6) on external contacts, relation Eq. (B.5) can be written as:

$$\sum_{c^* \in S} f_\alpha^{c^*} x_\beta^{c^*} = \sum_{c \in V} f_\alpha^c \ell_\beta^c + \sum_{c^* \in S} f_\alpha^{c^*} l_\beta^{c^*} \tag{B.8}$$

Then, considering the relation Eq. (B.6):

$$\sigma_{\alpha\beta}^V = \frac{1}{V} \sum_{c \in S} f_\alpha^c x_\beta^c = \left[\sum_{c \in V} f_\alpha^{c^*} \ell_\beta^{c^*} + \sum_{c \in S} f_\alpha^c l_\beta^c \right] \tag{B.9}$$

Considering that branch vectors connected with boundary contact points l^{c^*} can be identified to the other branch vector ℓ^c, relation Eq. (B.9) can be written as:

$$\sigma_{\alpha\beta}^V = \frac{1}{V} \sum_{c \in (V,S)} f_\alpha^c \ell_\beta^c \tag{B.10}$$

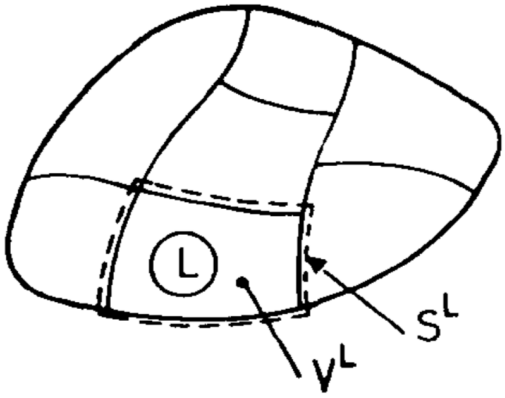

FIGURE B.2: Domain division in a continuum media, extracted from Bagi [32].

B.2 Equivalent strain in granular material

The equivalent strain prestented here is valid for 2D and 3D particles with arbitrary convex shape [32] (despite other propositions that only are valid in 2D grains [132, 50]). A similar procedure of the Section B.1 is made here. A "derivation" of the equivalent strain is repeated here. It consists in two steps: (i) the first step the average strain is evaluate on the contacts in the boundary that enclose the assembly of particles; (ii) the second step evaluate the average strain on the internal forces.

The strain tensor is taking from the symmetric part of the displacement gradient tensor. The average continuum strain tensor is defined by:

$$\varepsilon^V_{\alpha\beta} = \frac{1}{V} \iiint_V \frac{\partial u_\alpha}{\partial x_\beta} dV, \tag{B.11}$$

where u_α is the displacement vector. Using Gauss' theorem we can found:

$$\varepsilon^V_{\alpha\beta} = \frac{1}{V} \iint_S u_\alpha n_\beta dS, \tag{B.12}$$

The Eq. (B.12) stills valid by subdomains, Fig. B.2, it can be write as:

$$\varepsilon^{V^L}_{\alpha\beta} = \frac{1}{V^L} \iint_{S^L} u_\alpha n_\beta dS. \tag{B.13}$$

In order to evaluate this expression in a granular material Bagi [32] propose the discretization of the continuum media and after the discretization return to an expression of the displacement gradient tensor that contains the discrete micro-variables only. In this approach the application of the continuum mechanical formalism is a tool for the averaging of the micro-variables.

Eq. (B.12) can be applied in a "geometrical features" that can be divided into subdomains, V^L, and if a continuous displacement field is create on it.

Bagi creates an *space cell system* for the geometrical modelling. It is presented in compression and simple shear loads, Fig. B.3, the global deformation of the assembly is well represented by the deformations of the space cells since they characterise the distortions of the internal structure itself, instead of an individual grain or contact. Other interest point of this approach is that the deformation of the cells do not loose their meaning even if there are topological changes, for example, contacts lost or created in the assembly.

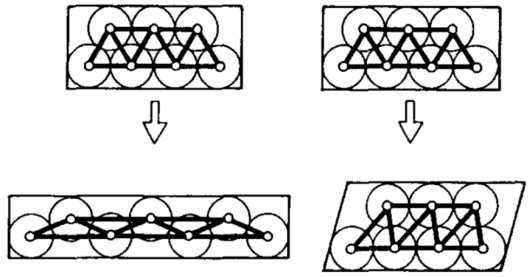

FIGURE B.3: Schematic representation of the geometrical model, extracted from Bagi [32].

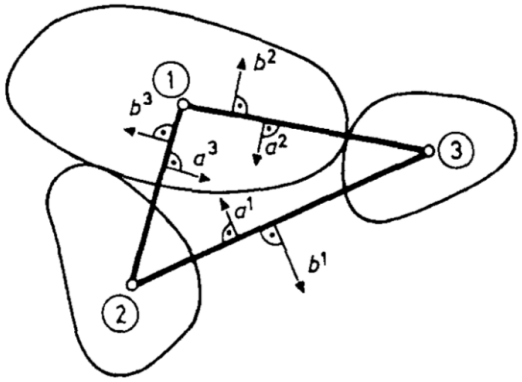

FIGURE B.4: Schematic representation of the vectors a_β and b_β, extracted from Bagi [32].

The geometrical model allows us the definition of a displacement field or any finite set of space cells in the following way. On the nodes of the simplexes let $u_\alpha(x_\beta)$ be equal to the translation of the grain centre while inside the simplex $u_\alpha(x_\beta)$ is defined as the linear interpolation of the node translations of that simplex. The $u_\alpha(x_\beta)$ field assigned to the assembly this way is piecewise linear inside the simplexes and along the faces and edges, and continuous throughout the whole system.

So consider now the L-th space cell whose average displacement gradient tensor is

$$\varepsilon^V_{\alpha\beta} = \frac{1}{V}\iint_S^L u_\alpha n_\beta dS^L \tag{B.14}$$

which, using the fact that $u_\alpha(x_\beta)$ is linear along the boundary, can be written in the following discrete form:

$$\varepsilon^{V^L}_{\alpha\beta} = \frac{1}{V^L}\sum_{k=1}^{D+1} u^k_\alpha a^k_\beta \tag{B.15}$$

where V^L and S^L are the volume and boundary of the L-th simplex, the index k runs over the nodes of this simplex, u^k_α is the translation of node k, and a^k_β was defined as:

$$a^k_\beta = -\frac{1}{D}b^k_\beta \tag{B.16}$$

where D is the total number of vertex in the geometrical model. These vector are ilustraded in 2D in the Fig. B.4. Since the sum of a^k_β vectors belonging to a simplex is zero, Eq. (B.16)

can be modified by distracting the same u_α^0 vector from each nodal displacement of the cell:

$$\varepsilon_{\alpha\beta}^V = \frac{1}{V^L}\sum_{k=1}^{D+1}(u_\alpha^k - u_\alpha^0)a_\beta^k \tag{B.17}$$

its means that the rigid-body translations do not change the deformation of the cell. Let u_α^0 be chosen as the average translation of the nodes:

$$u_\alpha^0 = \frac{1}{D+1}\sum_{k=1}^{D+1}u_\alpha^k, \tag{B.18}$$

which gives that the average deformation gradient tensor of the L-th cell is:

$$\varepsilon_{\alpha\beta}^{V^L} = \frac{1}{D+1}\frac{1}{V^L}\sum_{m<n}(u_\alpha^m - u_\alpha^n)(a_\beta^m - a_\beta^n), \tag{B.19}$$

so after introducing the notation $\Delta u_\alpha^{mn} = u_\alpha^m - u_\alpha^n$ over the whole system and $d_j^{mn} = a_\beta^m - a_\beta^n$, the average displacement gradient tensor is expressed by the relative displacements of the pairs of nodes forming the edges of the cells:

$$\varepsilon_{\alpha\beta}^V = \frac{1}{V}\sum_{m<n}\Delta u_\alpha^{mn}d_\beta^{mn}, \tag{B.20}$$

the summation runs over all edges of the space cell system. Eq. (B.20) contains discrete micro-variables only: relative displacements of neighbouring nodes and the corresponding complementary area vectors. The skew-symmetric part of this tensor reflects the average rigid-body rotation of the space cells. The symmetric part expresses the deformations of the cells, and it is suggested to be the strain tensor of granular assemblies.

Appendix C

Résumé

Une forte concurrence avec d'autres moyens de transport a poussé l'industrie ferroviaire à se réinventer et rechercher des performances toujours plus élevées. De nos jours, l'obtention de vitesses chaque fois plus élevées exige le développement de modèles numériques précis pour concevoir et prédire le comportement des voies ferrées sous les contraintes mécaniques imposées par le passage du convoi. Dans cette thèse, nous avons concentré l'étude sur la couche de ballast. Ce composant présente un comportement mécanique complexe, lié à la nature granulaire de ses composants, il peut être solide, liquide ou gazeux. Ce comportement dépend de l'état de contrainte et de l'historique de déformation du milieu.

Deux classes de modèles numériques sont couramment utilisées pour prédire le comportement de ces systèmes : (1) les approches discrètes et (2) les approches continues. Pour ces premières, chaque grain du ballast est représenté par un corps rigide et interagit avec ses voisins par le biais de forces de contact non linéaires en utilisant, par exemple, la méthode de dynamique non régulière des contacts. En raison des limites de calcul, ce type de méthode ne peut résoudre que quelques mètres de longueur de ballast. Le couplage avec le sol sous la couche de ballast et avec les traverses reste également un problème non résolu dans la littérature. Pour les approches continues, le ballast est remplacé par un milieu continu homogénéisé, de façon à permettre l'utilisation de la méthode par éléments finis classique (EF). Cependant, ces modèles sont normalement utilisés avec des paramètres mécaniques homogènes, de sorte qu'ils ne représentent pas complètement l'hétérogénéité des déformations et des contraintes dans la couche de ballast.

Nous étudions dans cette thèse une approche alternative, utilisant un modèle de continuum hétérogène stochastique, qui peut être résolu avec une méthode par éléments finis tout en conservant dans une large mesure l'hétérogénéité des champs de contrainte et de déformation. L'objectif de ce modèle continu est de représenter statistiquement l'hétérogénéité du champ de contraintes dans un modèle de milieu continu ainsi que dans un modèle granulaire discret. Pour ce faire, les propriétés mécaniques sont représentées à l'aide de champs aléatoires. La présente thèse est divisée en trois parties: (1) la construction du modèle et l'identification des paramètres du matériau continuum (densité marginale de premier ordre, moyenne, variance, modèle de corrélation) ; (2) la propagation des ondes dans une voie ferrée ballastée et (3) l'exploration préliminaire de deux ensembles de données expérimentales. La première partie définit le modèle du continuum à fluctuations aléatoires et identifie les paramètres de notre modèle de continuum sur de petits échantillons cylindriques de ballast discret. Des modèles continus équivalents aux échantillons discrets sont générés et résolus en utilisant la méthode EF, et le champ stochastique utilisé pour fournir les propriétés mécaniques. Un processus d'optimisation est utilisé pour trouver une variance normalisée pour le matériau hétérogène stochastique. La deuxième partie de ce travail se concentre sur la résolution des équations dynamiques sur un modèle à grande échelle d'une voie ferrée ballastée utilisant la méthode des éléments spectraux. L'influence de l'hétérogénéité est mise en évidence et étudiée. En conséquence, des courbes de dispersion sont obtenues. Enfin, la troisième partie présente deux jeux de données distincts de mesures expérimentales sur le matériau de ballast : (1)

une boîte de ballast ; (2) un passage de train dans un segment de voie ferrée ballastée. Les courbes de mobilité ont été extraites de l'expérience sur les ballasts. Un problème inverse a été résolu afin d'estimer la vitesse de l'onde homogénéisée et la vitesse de l'onde locale et global dans le milieu. Les passages de trains enregistrés pour l'analyse de la vibration à moyenne fréquences sont presentée de façon préliminaire.

Bibliography

[1] R. Abou-Chacra and D. J. Thouless. “Self-consistent theory of localization. II. localization near the band edges”. In: *Journal of Physics C: Solid State Physics* 7.1 (1974), p. 65.

[2] R. Abou-Chacra, D. J. Thouless, and P.W. Anderson. “A selfconsistent theory of localization”. In: *Journal of Physics C: Solid State Physics* 6.10 (1973), p. 1734.

[3] E. Abrahams et al. “Scaling theory of localization: Absence of quantum diffusion in two dimensions”. In: *Physical Review Letters* 42.10 (1979), p. 673. DOI: 10.1103/PhysRevLett.42.673.

[4] L. de Abreu Corrêa, R. Cottereau, and B. Faure. “Dispersion analysis in ballasted railway tracks and Anderson localization in granular media”. In: *Journal of Sound and Vibration* (2018). Submitted for publication.

[5] L. de Abreu Corrêa et al. “Randomly-fluctuating heterogeneous continuum model of a ballasted railway track”. In: *Computational Mechanics* 60.5 (2017), pp. 845–861. DOI: 10.1007/s00466-017-1446-8.

[6] C. M. Aegerter et al. “Observation of Anderson localization of light in three dimensions”. In: *Journal of the Optical Society of America A* 24.10 (2007), A23–A27. DOI: 10.1364/JOSAA.24.000A23.

[7] I. Agnolin and J.N. Roux. “On the elastic moduli of three-dimensional assemblies of spheres: characterization and modeling of fluctuations in the particle displacement and rotation”. In: *International Journal of Solids and Structures* 45.3-4 (2008), pp. 1101–1123. DOI: 10.1016/j.ijsolstr.2007.07.016.

[8] S. Ahmed et al. “Numerical modelling of railway ballast at the particle scale”. In: *International Journal for Numerical and Analytical Methods in Geomechanics* (2015). Accepted for publication. DOI: 10.1002/nag.2424.

[9] A. Al Shaer et al. “Experimental settlement and dynamic behavior of a portion of ballasted railway track under high speed trains”. In: *Journal of Sound and Vibration* 316.March (2008), pp. 211–233. DOI: 10.1016/j.jsv.2008.02.055.

[10] P. Alart, D. Iceta, and D. Dureisseix. “A nonlinear domain decomposition formulation with application to granular dynamics”. In: *Computer Methods in Applied Mechanics and Engineering* 205-208 (2012), pp. 59–67. DOI: 10.1016/j.cma.2011.04.024.

[11] D Alleyne and P. Cawley. “A two-dimensional Fourier transform method for the measurement of propagating multimode signals”. In: *The Journal of the Acoustical Society of America* 89.3 (1991), pp. 1159–1168. DOI: 10.1121/1.400530.

[12] V. Alves Fernandes. “Numerical analysis of nonlinear soil behavior and heterogeneity effects on railway track response”. Theses. Ecole Centrale Paris, Nov. 2014.

[13] G. M. Amdahl. “Validity of the single processor approach to achieving large scale computing capabilities”. In: *Proceedings of the April 18-20, 1967, Spring joint computer conference*. ACM. 1967, pp. 483–485. DOI: 10.1145/1465482.1465560.

[14] P. W. Anderson. “Absence of Diffusion in Certain Random Lattices”. In: *Physical Review* 109.5 (1958), pp. 1492–1505. DOI: 10.1103/PhysRev.109.1492.

[15] I. V. Andrianov, J. Awrejcewicz, and D. Weichert. “Improved continuous models for discrete media”. In: *Mathematical Problems in Engineering* (2010). DOI: 10.1155/2010/986242.

[16] S. J. Antony. “Evolution of force distribution in three-dimensional granular media”. In: *Physical Review E* 63.1 (2000), p. 011302. DOI: 10.1103/PhysRevE.63.011302.

[17] S. J. Antony and M. R. Kuhn. “Influence of particle shape on granular contact signatures and shear strength: new insights from simulations”. In: *International Journal of Solids and Structures* 41.21 (2004), pp. 5863–5870. DOI: 10.1016/j.ijsolstr.2004.05.067.

[18] M. Arnst and R. G. Ghanem. “Probabilistic equivalence and stochastic model reduction in multiscale analysis”. In: *Computer Methods in Applied Mechanics and Engineering* 197 (2008), pp. 3584–3592. DOI: 10.1016/j.cma.2008.03.016.

[19] H. Askes and E. C. Aifantis. “Gradient elasticity theories in statics and dynamics-a unification of approaches”. In: *International Journal of Fracture* 139.2 (2006), pp. 297–304. DOI: 10.1007/s10704-006-8375-4.

[20] B. A. Auld. *Acoustic fields and waves in solids, vol. 1*. John Wiley and Sons, 1973.

[21] B. A. Auld. *Acoustic fields and waves in solids, vol. 2*. John Wiley and Sons, 1973.

[22] E. Azéma and F. Radjaï. “Stress-strain behavior and geometrical properties of packings of elongated particles”. In: *Physical Review E* 81.5 (2010), p. 051304. DOI: 10.1103/PhysRevE.81.051304.

[23] E. Azéma, F. Radjaï, and F. Dubois. “Packings of irregular polyhedral particles: Strength, structure, and effects of angularity”. In: *Physical Review E* 87.6 (2013), p. 062203. DOI: 10.1103/PhysRevE.87.062203.

[24] E. Azéma, F. Radjaï, and R. Peyroux. “Dynamique d’un milieu granulaire soumis à des vibrations horizontales - Simulations numériques 3D”. In: *18ème Congrès Français de Mécanique (Grenoble 2007)* (2007).

[25] E. Azéma, F. Radjai, and G. Saussine. “Quasistatic rheology, force transmission and fabric properties of a packing of irregular polyhedral particles”. In: *Mechanics of Materials* 41 (2009), pp. 729–741. DOI: 10.1016/j.mechmat.2009.01.021.

[26] E. Azéma et al. “Vibrational dynamics of 3D granular media composed with polyhedral grains”. In: *IX Congreso de Geotecnia, Sociedad Colombiana de geotecnia*. 2008, p. 8.

[27] E. Azéma et al. “Vibrational dynamics of confined granular material”. In: *Physical Review E* 74 (Oct. 2006), p. 031302. DOI: 10.1103/PhysRevE.74.031302.

[28] H. Bachmann et al. *Vibration problems in structures: practical guidelines*. Birkhäuser, 2012.

[29] G. E. Backus. “Long-wave elastic anisotropy produced by horizontal layering”. In: *Journal of Geophysical Research* 67.11 (1962), pp. 4427–4440. DOI: 10.1029/JZ067i011p04427.

[30] K. Bagi. “Analysis of microstructural strain tensors for granular assemblies”. In: *International Journal of Solids and Structures* 43.10 (2006), pp. 31666–3184. DOI: 10.1016/j.ijsolstr.2005.07.016.

[31] K. Bagi. "Statistical analysis of contact force components in random granular assemblies". In: *Granular Matter* 5.1 (2003), pp. 45–54. DOI: 10.1007/s10035-002-0123-5.

[32] K. Bagi. "Stress and strain in granular assemblies". In: *Mechanics of Materials* 22.3 (1996), pp. 165–177. DOI: 10.1016/0167-6636(95)00044-5.

[33] H. Bao et al. "Large-scale simulation of elastic wave propagation in heterogeneous media on parallel computers". In: *Computer Methods in Applied Mechanics and Engineering* 152.1-2 (1998), pp. 85–102. DOI: 10.1016/S0045-7825(97)00183-7.

[34] J. P. Bardet and I. Vardoulakis. "The asymetry of stress in granular media". In: *International Journal of Solids and Structures* 38.2 (2001), pp. 353–367. DOI: 10.1016/S0020-7683(00)00021-4.

[35] U. Basu and A. K. Chopra. "Perfectly matched layers for transient elastodynamics of unbounded domains". In: *International Journal for Numerical Methods in Engineering* 59.8 (2004), pp. 1039–1074. DOI: 10.1002/nme.896.

[36] J. V. Beck and K. J. Arnold. *Parameter estimation in engineering and science*. 1st ed. New York, USA: Wiley and Sons, 1977.

[37] J. J. Becker et al. "Global Bathymetry and Elevation Data at 30 Arc Seconds Resolution: SRTM30 PLUS". In: *Marine Geodesy* 32.4 (2009), pp. 355–371. DOI: 10.1080/01490410903297766.

[38] C. Bernardi and Y. Maday. *Approximations spectrales de problemes aux limites elliptiques*. Vol. 10. Springer, 1992.

[39] R. K. Bhattacharyya. "A note on wave propagation in granular medium". In: *Pure and Applied Geophysics* 114.4 (1976), pp. 639–646. DOI: 10.1007/BF00875657.

[40] L Blum and G. Stell. "Erratum: Polydisperse systems. I. Scattering function for polydisperse fluids of hard or permeable spheres". In: *Journal of Chemical Physics* 72.3 (1980), p. 2212. DOI: 10.1063/1.439328.

[41] L. Blum and G. Stell. "Polydisperse systems. I. Scattering function for polydisperse fluids of hard or permeable spheres". In: *Journal of Chemical Physics* 71.1 (1979), pp. 42–46. DOI: 10.1063/1.438088.

[42] C. Boutin. "Acoustics of porous media with inner resonators". In: *The Journal of the Acoustical Society of America* 134.6 (2013), pp. 4717–4729. DOI: 10.1121/1.4824965.

[43] H. Brandt. "A study of the speed of sound in porous granular media". In: *Journal of Applied Mechanics* 22 (1955), pp. 479–186.

[44] M. Brewer et al. "The mesquite mesh quality improvement toolkit". In: *Proceedings of the 12th International Meshing Roundtable*. Santa Fe, New Mexico, USA, 2003, pp. 239–250.

[45] I. E. Burovoi. "Fast measurement of group delay in long electric networks". In: *Measurement Techniques* 32.5 (1989), pp. 457–459.

[46] C. Burstedde, Wilcox L. C., and O. Ghattas. "`p4est`: Scalable Algorithms for Parallel Adaptive Mesh Refinement on Forests of Octrees". In: *SIAM Journal on Scientific Computing* 33.3 (2011), pp. 1103–1133. DOI: 10.1137/100791634.

[47] S. Butterworth. "On the theory of filter amplifiers". In: *Wireless Engineer* 7.6 (1930), pp. 536–541.

[48] Pierre C. "Weak and strong vibration localization in disordered structures: a statistical investigation". In: *Journal of Sound and Vibration* 139.1 (1990), pp. 111–132. DOI: 10.1016/0022-460X(90)90779-Y.

[49] J. J. Camata and A. L. G. A. Coutinho. "Parallel Implementation and Performance Analysis of a Linear Octree Finite Element Mesh Generation Scheme". In: *Concurrency and Computation: Practice and Experience* 25 (2013), pp. 826–842. DOI: 10.1002/cpe.2869.

[50] B. Cambou, M. Chaze, and F. Dedecker. "Change of scale in granular materials". In: *European Journal of Mechanics - A/Solids* 19.6 (2000), pp. 999–1014. DOI: 10.1016/S0997-7538(00)01114-1.

[51] B. Cambou, M. Jean, and Farhang R. *Micromechanics of granular materials*. John Wiley & Sons, 2013.

[52] Bernard Cambou. *Behaviour of Granular Materials*. Vol. 385. Springer, 1998.

[53] R. J. Cameron, C. M. Kudsia, and R. Mansour. *Microwave filters for communication systems*. John Wiley & Sons, 2015.

[54] J. Campos and G. De Rus. "Some stylized facts about high-speed rail: A review of HSR experiences around the world". In: *Transport Policy* 16.1 (2009), pp. 19–28. DOI: 10.1016/j.tranpol.2009.02.008.

[55] L. de Carvalho Paludo, V. Bouvier, and R. Cottereau. "Scalable parallel scheme for sampling of Gaussian random fields over very large domains". In: *International Journal for Numerical Methods in Engineering* 117.8 (2019), pp. 845–859. DOI: 10.1002/nme.5981.

[56] E. Casarotti et al. "CUBIT and seismic wave propagation based upon the spectral-element method: an advanced unstructured mesher for complex 3D geological media". In: *Proceedings of the 16th International Meshing Roundtable*. Ed. by M. L. Brewer and D. Marcum. 5B. Springer, 2008, pp. 579–597. DOI: 10.1007/978-3-540-75103-8_32.

[57] A. A. Chabanov, M. Stoytchev, and A. Z. Genack. "Statistical signatures of photon localization". In: *Nature* 404.6780 (2000), p. 850. DOI: 10.1038/35009055.

[58] C. S. Chang, S. J. Chao, and Y. Chang. "Estimates of elastic moduli for granular material with anisotropic random packing structure". In: *International Journal of Solids and Structures* 32.14 (1995), pp. 1989–2008. DOI: 10.1016/0020-7683(94)00225-L.

[59] C. S. Chang and M. Lun. "Elastic material constants for isotropic granular solids with particle rotation". In: *International Journal of Solids and Structures* 29.8 (1992), pp. 1001–1018. DOI: 10.1016/0020-7683(92)90071-Z.

[60] N. Cherroret and S. E. Skipetrov. "Microscopic derivation of self-consistent equations of Anderson localization in a disordered medium of finite size". In: *Physical Review E* 77.4 (2008), p. 046608. DOI: 10.1103/PhysRevE.77.046608.

[61] C. Cholet et al. "Granular Media and Ballasted Railway Tracks Milieux Granulaires Et Voies Ballastées". In: *Nonsmooth Mechanics and Analysis*. Springer, 2006, pp. 221–232. DOI: 10.1007/0-387-29195-4_19.

[62] G. Cohen. *Higher-order numerical methods for transient wave equations*. Scientific Computation. Springer, 2001.

[63] D. P. Connolly et al. "Benchmarking railway vibrations – track, vehicle, ground and building effects". In: *Construction and Building Materials* (2014). In press. DOI: 10.1016/j.conbuildmat.2014.07.042.

[64] S. N. Coopersmith et al. “Model for force fluctuations in bead packs”. In: *Physical Review E* 53.5 (1996), pp. 4673–4685. DOI: 10.1103/PhysRevE.53.4673.

[65] R. Cottereau and R. Sevilla. “Stability of an explicit high-order spectral element method for acoustics in heterogeneous media based on local element stability criteria”. In: *International Journal for Numerical Methods in Engineering* 116.4 (2018), pp. 223–245. DOI: 10.1002/nme.5922.

[66] P. A. Cundall and O. D. L. Strack. “A discrete numerical model for granular assemblies”. In: *Geotechnique* 29.1 (1979), pp. 47–65. DOI: 10.1680/geot.1979.29.1.47.

[67] B. d’Aguanno and R. Klein. “Integral-equation theory of polydisperse Yukawa systems”. In: *Physical Review A* 46.12 (1992), pp. 7652–7656. DOI: 10.1103/PhysRevA.46.7652.

[68] R. Dalichaouch et al. “Microwave localization by two-dimensional random scattering”. In: *Nature* 354.6348 (1991), p. 53. DOI: 10.1038/354053a0.

[69] L. de Abreu Corrêa et al. “Impact of the heterogeneity of the ballast on the dynamical behavior of the ballast-soil system”. In: *Proceedings of the CM3 Conference on Computational Transport*. Springer, 2016, pp. 185–205. DOI: 10.1007/978-3-319-54490-8_12.

[70] I. Deiros et al. “Quantifying Degradation of Railway Ballast Using Numerical Simulations of Micro-deval Test and In-situ Conditions”. In: *Procedia Engineering* 143 (2016), pp. 1016–1023. DOI: 10.1016/j.proeng.2016.06.096.

[71] H. B. Dhia. “Multiscale mechanical problems: the Arlequin method”. In: *Comptes Rendus de l’Academie des Sciences Series IIB Mechanics Physics Astronomy* 12.326 (1998), pp. 899–904.

[72] H. B. Dhia and G. Rateau. “The Arlequin method as a flexible engineering design tool”. In: *International Journal for Numerical Methods in Engineering* 62.11 (2005), pp. 1442–1462. DOI: 10.1002/nme.1229.

[73] P. J. Digby. “The effective elastic moduli of porous granular rocks”. In: *Journal of Applied Mechanics* 48.4 (1981), pp. 803–808. DOI: 10.1115/1.3157738.

[74] A. Drescher and G. de Josselin de Jong. “Photoelastic verification of a mechanical model for the flow of a granular material”. In: *Journal of the Mechanics and Physics of Solids* 20.5 (1972), pp. 337–340. DOI: 10.1016/0022-5096(72)90029-4.

[75] M.B. Drozdz. “Efficient Finite Element Modelling Of Ultrasound Waves In Elastic Media”. PhD thesis. Londres: Imperial College of Science Technology and Medicine, 2008.

[76] X. Du and M. Ostoja-Starzewski. “On the scaling from statistical to representative volume element in thermoelasticity of random materials”. In: *Networks and Heterogeneous Media* 1.2 (2006), p. 259.

[77] O. Durán, N. P. Kruyt, and S. Luding. “Analysis of three-dimensional micro-mechanical strain formulations for granular materials: evaluation of accuracy”. In: *International Journal of Solids and Structures* 47.2 (2010), pp. 251–260. DOI: 10.1016/j.ijsolstr.2009.09.035.

[78] C. Eloy and E. Clément. “Stochastic aspects of the force network in a regular granular piling”. In: *Journal de Physique I* 7.12 (1997), pp. 1541–1558. DOI: 10.1051/jp1:1997155.

[79] J. Engelbrecht et al. “Waves in microstructured materials and dispersion”. In: *Philosophical Magazine* 85.33-35 (2005), pp. 4127–4141. DOI: 10.1080/14786430500362769.

[80] C. Esveld. *Modern railway track*. MRT-productions Zaltbommel, The Netherlands, 2001.

[81] P. Evesque. "Distribution of contact forces in a homogeneous granular material of identical spheres under triaxial compression". In: *Poudres & Grains* 14.4 (2004), pp. 82–95.

[82] D. J. Ewins. *Modal testing: theory and practice*. Vol. 15. Research studies press Letchworth, 1984.

[83] Radjai F. et al. "Force distributions in dense two-dimensional granular systems". In: *Physical Review Letters* 77.2 (1996), pp. 274–277. DOI: 10.1103/PhysRevLett.77.274.

[84] T. G. Farr et al. "The shuttle radar topography mission". In: *Reviews of Geophysics* 45.2 (2007), 2005RG000183. DOI: 10.1029/2005RG000183View.

[85] G. Feher. "Electron spin resonance experiments on donors in silicon. I. Electronic structure of donors by the electron nuclear double resonance technique". In: *Physical Review* 114.5 (1959), p. 1219. DOI: 10.1103/PhysRev.114.1219.

[86] J. F. Ferellec et al. "Analysis of compaction of railway ballast by different maintenance methods using DEM". In: *EPJ Web of Conferences*. Vol. 140. 2017, p. 15032. DOI: 10.1051/epjconf/201714015032.

[87] G. Festa and S. Nielsen. "PML absorbing boundaries". In: *Bulletin of the Seismological Society of America* 93.2 (2003), pp. 891–903. DOI: 10.1785/0120020098.

[88] G. Festa and J. P. Vilotte. "The Newmark scheme as velocity-stress time-staggering: An efficient PML implementation for spectral element simulations of elastodynamics". In: *Geophysical Journal International* 161.3 (June 2005), pp. 789–812. DOI: 10.1111/j.1365-246X.2005.02601.x.

[89] Message P Forum. *MPI: A Message-Passing Interface Standard*. Tech. rep. Knoxville, TN, USA, 1994.

[90] GDR MiDi. "On dense granular flows". In: *European Physical Journal E: Soft Matter* 14.4 (2004), pp. 341–65. DOI: 10.1140/epje/i2003-10153-0.

[91] J. Geng et al. "Footprints in sand: the response of a granular material to local perturbations". In: *Physical Review Letters* 87.3 (2001), p. 035506. DOI: 10.1103/PhysRevLett.87.035506.

[92] H. G. Georgiadis, P. A. Gourgiotis, and D. S. Anagnostou. "The Boussinesq problem in dipolar gradient elasticity". In: *Archive of Applied Mechanics* 84.9-11 (2014), pp. 1373–1391. DOI: 10.1007/s00419-014-0854-x.

[93] H. G. Georgiadis, I. Vardoulakis, and E. G. Velgaki. "Dispersive Rayleigh-wave propagation in microstructured solids characterized by dipolar gradient elasticity". In: *Journal of Elasticity* 74.1 (2004), pp. 17–45. DOI: 10.1023/B:ELAS.0000026094.95688.c5.

[94] H. G. Georgiadis and E. G. Velgaki. "High-frequency Rayleigh waves in materials with micro-structure and couple-stress effects". In: *International Journal of Solids and Structures* 40.10 (2003), pp. 2501–2520. DOI: 10.1016/S0020-7683(03)00054-4.

[95] I. T. Ghisi, J. J. Camata, and A. L. G. A. Coutinho. "Impact of tetrahedralization on parallel conforming octree mesh generation". In: *International Journal for Numerical Methods in Fluids* 75 (2014), pp. 800–814. DOI: 10.1002/fld.3918.

[96] B. Gilles and C. Coste. "Low-frequency behavior of beads constrained on a lattice". In: *Physical Review Letters* 90.17 (2003), p. 174302. DOI: 10.1103/PhysRevLett.90.174302.

[97] J. D. Goddard. "Nonlinear elasticity and pressure-dependent wave speeds in granular media". In: *Proceedings of the Royal Society A* 430.1878 (1990), pp. 105–131. DOI: 10.1098/rspa.1990.0083.

[98] I. Goldhirsch and C. Goldenberg. "On the microscopic foundations of elasticity". In: *European Physical Journal E* 9.3 (2002), pp. 245–251. DOI: 10.1140/epje/i2002-10073-5. eprint: 0203360.

[99] M. Grigoriu. "Simulation of stationary non-gaussian translation processes". In: *Journal of Engineering Mechanics* 124.2 (1998), pp. 121–126. DOI: 10.1061/(ASCE)0733-9399(1998)124:2(121).

[100] N. Guerin. "Approche expérimentale et numérique du comportement du ballast des voies ferrées". in French. PhD thesis. École nationale des ponts et chaussées, 1996.

[101] L. Guillot et al. "Numerical simulation of seismic wave propagation: site effects". In: *Chocs* 45 (2014), pp. 29–36.

[102] J. L Gustafson. "Reevaluating Amdahl's law". In: *Communications of the ACM* 31.5 (1988), pp. 532–533.

[103] S. A. Hall et al. "Discrete and continuum analysis of localised deformation in sand using X-ray μCT and volumetric digital image correlation". In: *Géotechnique* 60.5 (2010), pp. 315–322.

[104] F. Han, J. Cui, and Y. Yu. "The statistical second-order two-scale method for mechanical properties of statistically inhomogeneous materials". In: *International Journal for Numerical Methods in Engineering* 84 (2010), pp. 972–988. DOI: 10.1002/nme.2928.

[105] F. J. Harris. "On the use of windows for harmonic analysis with the discrete Fourier transform". In: *Proceedings of the IEEE* 66.1 (1978), pp. 51–83. DOI: 10.1109/PROC.1978.10837.

[106] M. Heckl, G. Hauck, and R. Wettschureck. "Structure-borne sound and vibration from rail traffic". In: *Journal of Sound and Vibration* 193.1 (1996), pp. 175–184. DOI: 10.1006/jsvi.1996.0257.

[107] D. Hertz and M. Azaria. "Time delay estimation between two phase shifted signals via generalized cross-correlation methods". In: *Signal Processing* 8.2 (1985), pp. 235–257. DOI: 10.1016/0165-1684(85)90076-3.

[108] T. M. P. Hoang et al. "A domain decomposition method for granular dynamics using discrete elements and application to railway ballast". In: *Annals of Solid and Structural Mechanics* 2.2-4 (2011), pp. 87–98. DOI: 10.1007/s12356-011-0020-x.

[109] D. W. Howell, R. P. Behringer, and C. T. Veje. "Fluctuations in granular media". In: *Chaos* 9.3 (1999), pp. 559–572. DOI: 10.1063/1.166430.

[110] H. Hu et al. "Localization of ultrasound in a three-dimensional elastic network". In: *Nature Physics* 4.12 (2008), pp. 945–948. DOI: 10.1038/nphys1101.

[111] C. Huet. "Remarques sur l'assimilation d'un matériau hétérogéne á un milieu continu équivalent". In: *Rheological Behaviour and Structure of Materials. Presses ENPC, Paris* (1981), pp. 231–245.

[112] C. Huet. "Universal conditions for assimilation of a heterogeneous material to an effective continuum". In: *Mechanics Research Communications* 9.3 (1982), pp. 165–170. DOI: 10.1016/0093-6413(82)90048-9.

[113] K. Hutter and K. R. Rajagopal. "On flows of granular materials". In: *Continuum Mechanics and Thermodynamics* 6 (1994), pp. 81–139. DOI: 10.1007/BF01140894.

[114] C. L. Hwang et al. "The material and mechanical property of heavy-duty prestressed concrete sleeper". In: *Applied Mechanics and Materials*. Vol. 97. 2011, pp. 408–413. DOI: 10.4028/www.scientific.net/AMM.97-98.408.

[115] T. Ichimura et al. "Implicit nonlinear wave simulation with 1.08T DOF and 0.270T unstructured finite elements to enhance comprehensive earthquake simulation". In: *Proceedings of the International Conference for High Performance Computing, Networking, Storage and Analysis (SuperComputing)*. 2015. DOI: 10.1145/2807591.2807674.

[116] B. Indraratna, W. Salim, and C. Rujikiatkamjorn. *Advanced rail geotechnology. Ballasted track*. CRC Press, 2011.

[117] INNOTRACK D2.1.3. *First phase on the modelling of poor quality sites*. Tech. rep. Project no. tip5 ct-2006-031415. European commission - sixth framework program, 2009.

[118] T. Isaac et al. "Recursive algorithms for distributed forests of octrees". In: *SIAM Journal on Scientific Computing* (2015). DOI: 10.1137/140970963.

[119] Y. Ito, A. M. Shih, and B. K. Soni. "Octree-based reasonable-quality hexahedral mesh generation using a new set of refinement templates". In: *International Journal for Numerical Methods in Engineering* 77.13 (2009), pp. 1809–1833. DOI: 10.1002/nme.2470.

[120] X. Jacob et al. "Acoustic probing of the jamming transition in an unconsolidated granular medium". In: *Physical Review Letters* 100.15 (2008), p. 158003. DOI: 10.1103/PhysRevLett.100.158003.

[121] P. Jehel and R. Cottereau. "On damping created by heterogeneous yielding in the numerical analysis of nonlinear RC frame elements". In: *Computers & Structures.* 154 (2015), pp. 192–203. DOI: 10.1016/j.compstruc.2015.03.001.

[122] J. Jenkins et al. "Fluctuations and the effective moduli of an isotropic, random aggregate of identical, frictionless spheres". In: *Journal of the Mechanics and Physics of Solids* 53.1 (2005), pp. 197–225. DOI: 10.1016/j.jmps.2004.06.002.

[123] X. Jia, C. Caroli, and B. Velicky. "Ultrasound propagation in externally stressed granular media". In: *Physical Review Letters* 82.9 (1999), p. 1863. DOI: 10.1103/PhysRevLett.82.1863.

[124] P. Jop, Y. Forterre, and O. P Pouliquen. "A constitutive law for dense granular flows". In: *Nature* 441.7094 (2006), pp. 727–30. DOI: 10.1038/nature04801.

[125] S. Kaewunruen and A. Remennikov. *Dynamic properties of railway track and its components: a state-of-the-art review*. 2008.

[126] T. Kanit et al. "Determination of the size of the representative volume element for random composites: statistical and numerical approach". In: *International Journal of Solids and Structures* 40.13-14 (2003), pp. 3647–3679. DOI: 10.1016/S0020-7683(03)00143-4.

[127] Y. Khidas and X. Jia. "Anisotropic nonlinear elasticity in a spherical-bead pack: Influence of the fabric anisotropy". In: *Physical Review E* 81.2 (2010), p. 021303. DOI: 10.1103/PhysRevE.81.021303.

[128] J. M. Kincaid and J. J. Weis. "Radial distribution function of a hard-sphere solid". In: *Molecular Physics* 34.4 (1977), pp. 931–938. DOI: 10.1080/00268977700102241.

[129] L. Knopoff. "A matrix method for elastic wave problems". In: *Bulletin of the Seismological Society of America* 54.1 (1964), p. 431.

[130] D. Komatitsch. "The spectral-element method in seismology". In: *Geophysical Monograph Series* 157.55 (2005), pp. 205–227. DOI: 10.1029/157GM13.

[131] D. Komatitsch, J. Ritsema, and J. Tromp. "The spectral-element method, Beowulf computing, and global seismology." In: *Science* 298.5599 (Nov. 2002), pp. 1737–42. ISSN: 1095-9203. DOI: 10.1126/science.1076024.

[132] N. P. Kruyt and L. Rothenburg. "Micromechanical definition of the strain tensor for granular materials". In: *Journal of Applied Mechanics* 63.3 (1996), pp. 706–711. DOI: 10.1115/1.2823353.

[133] L. Kudela et al. "Smart octrees: Accurately integrating discontinuous functions in 3D". In: *Computer Methods in Applied Mechanics and Engineering* 306 (2016), pp. 406–426. DOI: 10.1016/j.cma.2016.04.006.

[134] M. R. Kuhn. "Structured deformation in granular materials". In: *Mechanics of Materials* 31.6 (1999), pp. 407–429. DOI: 10.1016/S0167-6636(99)00010-1.

[135] F. Lado. "Integral equation theory of polydisperse colloidal suspensions using orthogonal polynomial expansions". In: *Physical Review E* 54.4 (1996), pp. 4411–4419. DOI: 10.1103/PhysRevE.54.4411.

[136] J. C. Lagarias et al. "Convergence properties of the Nelder–Mead simplex method in low dimensions". In: *SIAM Journal on Optimization* 9.1 (1998), pp. 112–147. DOI: 10.1137/S1052623496303470.

[137] P E Lagasse. "Higher order finite element analysis of topographic guides supporting elastic surface waves". In: *The Journal of the Acoustical Society of America* 53.4 (1973), pp. 1116–1122. DOI: 10.1121/1.1913432.

[138] A. Lagendijk, B. Van Tiggelen, and D. S. Wiersma. "Fifty years of Anderson localization". In: *Physical Today* 62.8 (2009), pp. 24–29.

[139] H. Lamb. "On waves in an elastic plate". In: *Proceedings of the Royal Society of London A: Mathematical, Physical and Engineering Sciences* 93.648 (1917), pp. 114–128. ISSN: 0950-1207. DOI: 10.1098/rspa.1917.0008.

[140] B. P. Lawney and S. Luding. "Frequency filtering in disordered granular chains". In: *Acta mechanica* 225.8 (2014), p. 2385. DOI: 10.1007/s00707-014-1130-4.

[141] M. Leibig. "Model for the propagation of sound in granular materials". In: *Physical Review E* 49.2 (1994), pp. 1647–1656. DOI: 10.1103/PhysRevE.49.1647.

[142] W. L. Lim and G. R. McDowell. "Discrete element modelling of railway ballast". In: *Granular Matter* 7.1 (2005), pp. 19–29. DOI: 10.1007/s10035-004-0189-3.

[143] C. H. Liu and S. R. Nagel. "Sound in sand". In: *Physical Review Letters* 68.15 (1992), p. 2301. DOI: 10.1103/PhysRevLett.68.2301.

[144] C. H. Liu et al. "Force fluctuations in bead packs". In: *Science* 269.5223 (1995), pp. 513–515. DOI: 10.1126/science.269.5223.513.

[145] O. I. Lobkis and R. L. Weaver. "Anderson localization of ultrasound in plates: Further experimental results". In: *The Journal of the Acoustical Society of America* 124.6 (2008), pp. 3528–3533. DOI: 10.1121/1.2999345.

[146] *Logiciel de Mécanique gérant les contacts*. https://git-xen.lmgc.univ-montp2.fr/lmgc90/lmgc90_user/wikis/home. Accessed: 05/08/2016.

[147] A. E. H. Love. *A Treatise on the Mathematical Theory of Elasticity*. A Treatise on the Mathematical Theory of Elasticity v. 4. Cambridge University Press, 1927. ISBN: 9781107618091.

[148] M. Lu and G. R. McDowell. "The importance of modelling ballast particle shape in the discrete element method". In: *Granular Matter* 9 (2007), pp. 69–80. DOI: 10.1007/s10035-006-0021-3.

[149] Y. Maday and A. T. Patera. "Spectral element methods for the incompressible Navier-Stokes equations". In: *State-of-the-art surveys on computational mechanics (A90-47176 21-64). New York, American Society of Mechanical Engineers, 1989, p. 71-143. Research supported by DARPA*. 1989, pp. 71–143.

[150] T. S. Majmudar and R. P. Behringer. "Contact force measurements and stress-induced anisotropy in granular materials". In: *Nature* 435.7045 (2005), p. 1079. DOI: 10.1038/nature03805.

[151] H. A. Makse et al. "Granular packings: nonlinear elasticity, sound propagation, and collective relaxation dynamics". In: *Physical Review E* 70.6 (2004), p. 061302. DOI: 10.1103/PhysRevE.70.061302.

[152] H. A Makse et al. "Why effective medium theory fails in granular materials". In: *Physical Review Letters* 83.24 (1999), p. 5070. DOI: 10.1103/PhysRevLett.83.5070.

[153] *MATLAB version 8.5.0.197613 (R2015a)*. The Mathworks, Inc. Natick, Massachusetts, 2015.

[154] S. McNamara, E. G. Flekkøy, and K. J. Måløy. "Grains and gas flow: molecular dynamics with hydrodynamic interactions". In: *Physical Review E* 61.4 (2000), pp. 4054–4059. DOI: 10.1103/PhysRevE.61.4054.

[155] B. Miller, C. O'Hern, and R. P. Behringer. "Stress fluctuations for continuously sheared granular materials". In: *Physical Review Letters* 77.15 (1996), pp. 3110–3113. DOI: 10.1103/PhysRevLett.77.3110.

[156] G. W. Milton. "The theory of composites". In: *The Theory of Composites, by Graeme W. Milton, pp. 748. ISBN 0521781256. Cambridge, UK: Cambridge University Press, May 2002.* (2002), p. 748.

[157] A. Misra and P. Poorsolhjouy. "Granular micromechanics based micromorphic model predicts frequency band gaps". In: *Continuum Mechanics and Thermodynamics* 28.1-2 (2016), p. 215. DOI: 10.1007/s00161-015-0420-y.

[158] J. K. Mitchell and K. Soga. *Fundamentals of soil behavior*. Vol. 3. John Wiley & Sons New York, 2005.

[159] A. Modaressi, S. Boufellouh, and P. Evesque. "Modeling of stress distribution in granular piles: Comparison with centrifuge experiments". In: *Chaos* 9.3 (1999), pp. 523–543. DOI: 10.1063/1.166427.

[160] G. Moreau and D. Caillerie. "Continuum modeling of lattice structures in large displacement applications to buckling analysis". In: *Computers & Structures*. 68 (1998), pp. 181–189. DOI: 10.1016/S0045-7949(98)00041-8.

[161] J. J. Moreau. "Numerical investigation of shear zones in granular materials". In: *Proceedings of HLRZ-workshop on friction, arching, contact dynamics*. World Scientific, 1997, pp. 233–247.

[162] J. J. Moreau. "The stress tensor in granular media and in other mechanical collections". In: *Micromechanics of granular materials*. Ed. by B. Cambou, M. Jean, and F. Radjaï. Wiley, 2001.

[163] J. J. Moreau. "Unilateral contact and dry friction in finite freedom dynamics". In: *Nonsmooth mechanics and applications*. Ed. by J. J. Moreau and P. D. Panagiotopoulos. Vol. 302. CISM Courses and Lectures. 1989, pp. 1–81.

[164] D. M. Mueth, H. M. Jaeger, and S. R. Nagel. "Force distribution in a granular medium". In: *Physical Review E* 57.3 (1998), pp. 3164–3169. DOI: 10.1103/PhysRevE.57.3164.

[165] J. A. Nelder and R. Mead. "A simplex method for function minimization". In: *The Computer Journal* 7.4 (1965), pp. 308–313. DOI: 10.1093/comjnl/7.4.308.

[166] N.-S. Nguyen, H. Magoariec, and B. Cambou. "Local stress analysis in granular materials at a mesoscale". In: *International Journal for Numerical and Analytical Methods in Geomechanics* 36 (2012), pp. 1609–1635. DOI: 10.1002/nag.1063.

[167] M. Nicodemi. "Force correlations and arch formation in granular assemblies". In: *Physical Review Letters* 80.6 (1998), pp. 1340–1343. DOI: 10.1103/PhysRevLett.80.1340.

[168] F. Nicot, N. Hadda, and F. Darve. "Second-order work analysis for granular materials using a multiscale approach". In: *International Journal for Numerical and Analytical Methods in Geomechanics* 37.17 (2013), pp. 2987–3007. DOI: 10.1002/nag.2175.

[169] A. N. Norris and D. L. Johnson. "Nonlinear elasticity of granular media". In: *Journal of Applied Mechanics* 64.1 (1997), pp. 39–49. DOI: 10.1115/1.2787292.

[170] A. Nuttall. "Some windows with very good sidelobe behavior". In: *IEEE Transactions on Acoustics, Speech, and Signal Processing* 29.1 (1981), pp. 84–91. DOI: 10.1109/TASSP.1981.1163506.

[171] John O'Donovan. "Micromechanics of wave propagation through granular material". PhD thesis. Imperial College London, 2013.

[172] A. V. Oppenheim. *Sinais e sistemas*. Prentice-Hall, 2010.

[173] M. Ostoja-Starzewski. "Lattice models in micromechanics". In: *Applied Mechanics Reviews* 55.1 (2002), pp. 35–60. DOI: 10.1115/1.1432990.

[174] M. Ostoja-Starzewski. "Material spatial randomness: From statistical to representative volume element". In: *Probabilistic Engineering Mechanics* 21.2 (2006), pp. 112–132. DOI: 10.1016/j.probengmech.2005.07.007.

[175] S. J. Owen and R. M. Shih. "A template-based approach for parallel hexahedral two-refinement". In: *Procedia Engineering* 124 (2015), pp. 31–43. DOI: 10.1016/j.proeng.2015.10.120.

[176] S. J. Owen, R. M. Shih, and C. D. Ernst. "A template-based approach for parallel hexahedral two-refinement". In: *Computer-Aided Design* 85 (2017), pp. 34–52. DOI: 10.1016/j.proeng.2015.10.120.

[177] E. T. Owens and K. E Daniels. "Sound propagation and force chains in granular materials". In: *EPL (Europhysics Letters)* 94.5 (2011), p. 54005.

[178] L. Paludo et al. "Efficient Parallel Generation of Random Field of Mechanical Properties for Geophysical Application". In: *6th International Conference on Earthquake Geotechnical Engineering*. Christchurch, New Zealand, 2015.

[179] A. M. Panunzio et al. "Sensitivity of the wheel–rail contact interactions and Dang Van Fatigue Index in the rail with respect to irregularities of the track geometry". In: *Vehicle System Dynamics* (2018), pp. 1–28. DOI: 10.1080/00423114.2018.1436717.

[180] R. Paolucci et al. “Numerical prediction of low-frequency ground vibrations induced by high-speed trains at Ledsgaard, Sweden”. In: *Soil Dynamics and Earthquake Engineering* 23.6 (2003), pp. 425–433. DOI: 10.1016/S0267-7261(03)00061-7.

[181] S. Papargyri-Beskou, D. Polyzos, and D. E. Beskos. “Wave dispersion in gradient elastic solids and structures: a unified treatment”. In: *International Journal of Solids and Structures* 46.21 (2009), pp. 3751–3759. DOI: 10.1016/j.ijsolstr.2009.05.002.

[182] M. Parrish et al. “A selective approach to conformal refinement of unstructured hexahedral finite element meshes”. In: *Proceedings of the 16th International Meshing Roundtable*. Ed. by M. L. Brewer and D. Marcum. Springer, 2007, pp. 251–268. DOI: 10.1007/978-3-540-75103-8_15.

[183] E. Pasternak and H. B. Mühlhaus. “Generalised homogenisation procedures for granular materials”. In: *Mathematics and Mechanics of Granular Materials* 52.1 (2005), pp. 199–229. DOI: 10.1007/1-4020-4183-7_12.

[184] J. K. Percus and G. J. Yevick. “Analysis of classical statistical mechanics by means of colletive coordinates”. In: *Physical Review* 110.1 (1958), pp. 1–13. DOI: 10.1103/PhysRev.110.1.

[185] P. Pradhan and S. Sridhar. “Correlations due to localization in quantum eigenfunctions of disordered microwave cavities”. In: *Physical Review Letters* 85.11 (2000), p. 2360. DOI: 10.1103/PhysRevLett.85.2360.

[186] B. Puig and J. L. Akian. “Non-gaussian simulation using Hermite polynomials expansion and maximum entropy principle”. In: *Probabilistic Engineering Mechanics* 19.4 (2004), pp. 293–305. DOI: 10.1016/j.probengmech.2003.09.002.

[187] J. C. Quezada et al. “Penetration test in coarse granular material using Contact Dynamics Method”. In: *Computers and Geotechnics* 55 (2014), pp. 248–253. DOI: 10.1016/j.compgeo.2013.09.006.

[188] J. C. Quezada et al. “Settlement statistics of a granular layer composed of polyhedral particles”. In: *AIP Conference Proceedings*. Vol. 1542. 1. AIP. 2013, pp. 333–336.

[189] J. C. Quezada et al. “Stability, deformation, and variability of granular fills composed of polyhedral particles”. In: *Physical Review E* 86.3 (2012), p. 031308. DOI: 10.1063/1.4811935.

[190] J. Quintanilla. “Microstucture functions for random media with impenetrable particles”. In: *Physical Review E* 60 (1999), pp. 5788–5794. DOI: 10.1103/PhysRevE.60.5788.

[191] F. Radjai, S. Roux, and J. J. Moreau. “Contact Forces in a granular packing”. In: *Chaos* 9.3 (1999), pp. 544–550. DOI: 10.1063/1.166428.

[192] F. Radjai et al. “Bimodal Character of Stress Transmission in Granular Packings”. In: *Physical Review Letters* 80 (1998), pp. 61–64. DOI: 10.1103/PhysRevLett.80.61.

[193] F. Radjaï et al. “Fabric evolution and accessible geometrical states in granular materials”. In: *Granular Matter* 14.2 (2012), pp. 259–264. DOI: 10.1007/s10035-012-0321-8.

[194] F. Radjaï et al. “Force transmission in cohesive granular media”. In: *Mathematical Modeling and Physical Instances of granular Flows* (2010), pp. 240–260. DOI: 10.1063/1.3435395.

[195] *Random Field Library*. https://github.com/cottereau/randomField. Accessed: 27-01-2018.

[196] L. Rayleigh. "On waves propagated along the plane surface of an elastic solid". In: *Proceedings of the London Mathematical Society* 1.1 (1885), pp. 4–11. DOI: 10.1112/plms/s1-17.1.4.

[197] M. Renouf, F. Dubois, and P. Alart. "A parallel version of the non smooth contact dynamics algorithm applied to the simulation of granular media". In: *Journal of Computational and Applied Mathematics* 168.1-2 (2004), pp. 375–382. DOI: 10.1016/j.cam.2003.05.019.

[198] O. Reynolds. "LVII. On the dilatancy of media composed of rigid particles in contact. With experimental illustrations". In: *The London, Edinburgh, and Dublin Philosophical Magazine and Journal of Science* 20.127 (1885), pp. 469–481. DOI: 10.1080/14786448508627791.

[199] M. Rosenblatt. "Remarks on a multivariate transformation". In: *The Annals of Mathematical Statistics* (1952), pp. 470–472.

[200] L. Rothenburg and R. J. Bathurst. "Analytical study of induced anisotropy in idealized granular materials". In: *Geotechnique* 39 (1989), pp. 601–614.

[201] L. Rothenburg and N. P. Kruyt. "Micromechanical definition of an entropy for quasi-static deformation of granular materials". In: *Journal of the Mechanics and Physics of Solids* 57.3 (2009), pp. 634–655. DOI: 10.1016/j.jmps.2008.09.018.

[202] M Rouaud. *Probability, Statistics and Estimation. Propagation of Uncertainties in Experimental Measurement (Short Edition)*. Tech. rep. 2013.

[203] E. Ruiz-Girones. "Automatic hexahedral meshing algorithms: from structured to unstructured meshes". PhD thesis. Doctoral Thesis, 2011.

[204] B. Saint-Cyr et al. "Rheology of granular materials composed of nonconvex particles". In: *Physical Review E* 84.4 (2011), p. 041302. DOI: 10.1103/PhysRevE.84.041302.

[205] C. Salot, P. Gotteland, and P. Villard. "Influence of relative density on granular materials behavior: DEM simulations of triaxial tests". In: *Granular matter* 11.4 (2009), pp. 221–236. DOI: 10.1007/s10035-009-0138-2.

[206] A. Saltelli et al. *Global Sensitivity Analysis. The Primer*. John Wiley & Sons, 2008.

[207] A. Saltelli et al. *Sensitivity Analysis In Practice A Guide To Assessing Scientific Models*. John Wiley & Sons, 2004.

[208] H. Samet. *Applications of spatial data structures: computer graphics, image processing and GIS*. Addison-Wesley Publications, 1989.

[209] M. Satake. "Some considerations on the mechanics of granular materials". In: *Proceedings of the IUTAM Symposium on the Generalized Cosserat Continuum and the Continuum Theory of Dislocations with Applications*. Ed. by E. Kröner. 1968, pp. 156–159. DOI: 10.1007/978-3-662-30257-6_19.

[210] G. Saussine. "Contribution à la modélisation de granulats tridimensionnels: application au ballast." PhD thesis. Université Montpellier II-Sciences et Techniques du Languedoc, 2004.

[211] G. Saussine et al. "Compaction of Railway Ballast During Tamping Process: a Parametric Study". In: *AIP Conference Proceedings*. Vol. 1145. 1. AIP. 2009, pp. 469–472. DOI: 10.1063/1.3179964.

[212] G. Saussine et al. "Modelling ballast behaviour under dynamic loading. Part 1: A 2D polygonal discrete element method approach". In: *Computer methods in Applied Mechanics and Engineering* 195.19-22 (2006), pp. 2841–2859. DOI: 10.1016/j.cma.2005.07.006.

[213] G. Saussine et al. “Modelling ballast behaviour using a three-dimensional polyhedral discrete element method.” In: *XXI International Congress of Theoretical and Applied Mechanics, Warsaw, Poland*. 2004.

[214] G. Saussine et al. “Numerical modeling of the tamping operation by Discrete Element Approach”. In: *World Congress Rail Research*. 2008, pp. 1–9.

[215] G. Saussine et al. “Railway Ballast Settlement: A New Predictive Model”. In: *Proceedings of the Second International Conference on Railway Technology: Research, Development and Maintenance, Civil-Comp Press, Stirlingshire, UK, Paper*. Vol. 121. 2014.

[216] G. de Saxcé, J. Fortin, and O. Millet. “About the numerical simulation of the dynamics of granular media and the definition of the mean stress tensor”. In: *Mechanics of Materials* 36 (2004), pp. 1175–1184. DOI: 10.1016/j.mechmat.2003.01.002.

[217] F. Scheffold et al. “Localization or classical diffusion of light?” In: *Nature* 398.6724 (1999), p. 206.

[218] T. M. Schlittler and R. Cottereau. “Fully scalable implementation of a volume coupling scheme for the modeling of multiscale materials”. In: *Computational Mechanics* 60.5 (Nov. 2017), pp. 827 –844. DOI: 10.1007/s00466-017-1445-9.

[219] L. Schmitt et al. “New aspects of the dynamical effects on ballast fatigue and track settlement”. In: *WCRR*. Vol. 3. 2008.

[220] R. Schneiders. *Algorithms for quadrilateral and hexahedral mesh generation*. Lectures on Computational Fluid Dynamics. Von Karman Institute, 2000.

[221] R. Schneiders and R. Bünten. “Automatic generation of hexahedral finite element meshes”. In: *Computer Aided Geometric Design* 12.7 (1995). Grid Generation, Finite Elements, and Geometric Design, pp. 693 –707. DOI: 10.1016/0167-8396(95)00013-V.

[222] T. Schwartz et al. “Transport and Anderson localization in disordered two-dimensional photonic lattices”. In: *Nature* 446.7131 (2007), p. 52.

[223] E. T. Selig and J. M. Waters. *Track geotechnology and substructure management*. Thomas Telford Publishing, 1994. DOI: 10.1680/tgasm.20139.

[224] D. Serero et al. “Stress response function of a granular layer: quantitative comparison between experiments and isotropic elasticity”. In: *European Physical Journal E* 6.2 (2001), pp. 169–179. DOI: 10.1007/s101890170019.

[225] R. Sevilla and R. Cottereau. “Influence of periodically fluctuating material parameters on the stability of explicit high-order spectral element methods”. In: *Journal of Computational Physics* 373 (2018), pp. 304–323. DOI: 10.1016/j.jcp.2018.07.002.

[226] S. Shende and A. D. Malony. “The TAU parallel performance system”. In: *International Journal of High Performance Computing Applications* 20.2 (2006), pp. 287–311.

[227] J. F. Shepherd. “Topologic and geometric constraint-based hexahedral mesh generation”. PhD thesis. University of Utah, 2007.

[228] H. Shin and J. Santamarina. “Role of particle angularity on the mechanical behavior of granular mixtures”. In: *Journal of Geotechnical and Geoenvironmental Engineering* 139.2 (2013), pp. 353–355. DOI: 10.1061/(ASCE)GT.1943-5606.0000768.

[229] M. Shinozuka and G. Deodatis. “Simulation of multi-dimensional Gaussian stochastic fields by spectral representation”. In: *Applied Mechanics Reviews* 49 (1996), pp. 29–53. DOI: 10.1115/1.3101883.

[230] M. Shinozuka and G. Deodatis. "Simulation of stochastic processes by spectral representation". In: *Applied Mechanics Reviews* 44.4 (1991), pp. 191–204. DOI: 10.1115/1.3119501.

[231] A. Shukla. "Dynamic photoelastic studies of wave propagation in granular media". In: *Optics and Lasers in Engineering* 14.3 (1991), pp. 165–184. DOI: 10.1016/0143-8166(91)90047-W.

[232] *Shuttle Radar Topography Mission*. http://dds.cr.usgs.gov/srtm/version2_1/. Accessed: 12-10-2015.

[233] *Shuttle Radar Topography Mission*. ftp://topec.ucsd.edu/pub/srtm30_plus/srtm30. Accessed: 12-10-2015.

[234] S. E. Skipetrov and B. A. Van Tiggelen. "Dynamics of Anderson localization in open 3D media". In: *Physical Review Letters* 96.4 (2006), p. 043902. DOI: 10.1103/PhysRevLett.96.043902.

[235] S. E. Skipetrov and B. A. Van Tiggelen. "Dynamics of weakly localized waves". In: *Physical Review Letters* 92.11 (2004). DOI: 10.1103/PhysRevLett.92.113901.

[236] S. I. Skurativskyi and I. A. Skurativska. "Dynamics of traveling waves in fluctuating nonlocal media". In: *Communications in Nonlinear Science and Numerical Simulation* 49 (2017), pp. 9–16. DOI: 10.1016/j.cnsns.2017.01.030.

[237] J. H. Snoeijer et al. "Force network ensemble: a new approach to static granular matter". In: *Physical Review Letters* 92.5 (2004), p. 054302. DOI: 10.1103/PhysRevLett.92.054302.

[238] C. Soize. "Non-Gaussian positive-definite matrix-valued random fields for elliptic stochastic partial differential operators". In: *Computer Methods in Applied Mechanics and Engineering* 195.1-3 (2006), pp. 26–64. DOI: 10.1016/j.cma.2004.12.014.

[239] B. Solomon. *Railway Maintenance Equipment*. Voyageur Press, 2001.

[240] *SRTM Water Body Database*. https://dds.cr.usgs.gov/srtm/version2_1/SWBD/. Accessed: 19-09-2015.

[241] D. Stiebel et al. "Definition of reference cases typical for hot-spots in Europe with existing vibration problems". In: *Rivas Project SCP0-GA-2010-265754 (deliverable D1. 5) ed. Report to the EC* (2012).

[242] M. Störzer et al. "Observation of the critical regime near Anderson localization of light". In: *Physical Review Letters* 96.6 (2006), p. 063904. DOI: 10.1103/PhysRevLett.96.063904.

[243] A. S. J. Suiker, R. De Borst, and C. S. Chang. "Micro-mechanical modelling of granular material. Part 1: Derivation of a second-gradient micro-polar constitutive theory". In: *Acta Mechanica* 149 (2001), pp. 161–180. DOI: 10.1007/BF01261670.

[244] H. Sundar et al. "Low-constant parallel algorithms for finite element simulations using linear octrees". In: *Proceedings of the 2007 ACM/IEEE Conference on Supercomputing*. Vol. 25. 2007, pp. 1–12. DOI: 10.1145/1362622.1362656.

[245] Q.-A. Ta, D. Clouteau, and R. Cottereau. "Modeling of random anisotropic elastic media and impact on wave propagation". In: *European Journal of Computational Mechanics* 19.1-3 (2010), pp. 241–253. DOI: 10.3166/ejcm.19.241-253.

[246] *TAU - Tuning and Analysis Utilities*. http://tau.uoregon.edu. Accessed: 19-10-2015.

[247] T. J. Tautges. “The generation of hexahedral meshes for assembly geometry: survey and progress”. In: *International Journal for Numerical Methods in Engineering* 50.12 (2001), pp. 2617–2642. DOI: 10.1002/nme.139.

[248] *TGV*. http://jactiv.ouest-france.fr/actualites/france/sncf-ne-fait-pas-cadeaux-ses-jeunes-abonnes-tgv-max-81829. Accessed: 09/06/2018.

[249] H. Tollenaere and D. Caillerie. “Continuous modeling of lattice structures by homogenization”. In: *Advances in Engineering Software* 29.7-9 (1998), pp. 699–705. DOI: 10.1016/S0965-9978(98)00034-9.

[250] S. Torquato. *Random heterogeneous materials. Microstructure and macroscopic properties*. Springer, 2001. ISBN: 978-1-4757-6355-3.

[251] S. Torquato and G. Stell. “Microstructure of two-phase random media. V. The n-point matrix probability functions for impenetrable spheres”. In: *Journal of Chemical Physics* 82 (1985), pp. 980–987. DOI: 10.1063/1.448475.

[252] O. Tsoungui, D. Vallet, and J.C. Charmet. “Use of contact area trace to study the force distributions insisde 2D granular systems”. In: *Granular Matter* 1.2 (1998), pp. 65–69. DOI: 10.1007/s100350050010.

[253] T. Tsuchikura and M. Satake. “Statistical measure tensors and their application to computer simulation analysis of biaxial compression text”. In: *Engineering Mechanics: a Force for 21st Century*. Ed. by H. Murakami and J. E. Luco. ASCE. 1998, pp. 1732–1735.

[254] T. Tu, D. R. O’Hallaron, and O. Ghattas. “Scalable parallel octree meshing for terascale applications”. In: *Proceedings of the 2005 ACM/IEEE Conference on Supercomputing*. 2005, pp. 1–4. DOI: 10.1109/SC.2005.61.

[255] B. A. Van Tiggelen, A. Lagendijk, and D. S. Wiersma. “Reflection and transmission of waves near the localization threshold”. In: *Physical review letters* 84.19 (2000).

[256] L. Verlet and J. J. Weis. “Equilibrium theory of simple liquids”. In: *Physical Review A* 5.2 (1972), pp. 939–952. DOI: 10.1103/PhysRevA.5.939.

[257] C. Voivret. “Texture et comportement des matériaux granulaires à grande polydispersité”. PhD thesis. Université Montpellier 2, 2008.

[258] D. Vollhardt and P. Wölfle. “Diagrammatic, self-consistent treatment of the Anderson localization problem in 2 dimensions”. In: *Physical Review B* 22.10 (1980), p. 4666. DOI: 10.1103/PhysRevB.22.4666.

[259] A. Vrij. “Mixtures of hard spheres in the Percus-Yevick approximation. Light scattering at finite angles”. In: *Journal of Chemical Physics* 71.8 (1979), pp. 3267–3270. DOI: 10.1063/1.438756.

[260] K. Walton. “The effective elastic moduli of a random packing of spheres”. In: *Journal of the Mechanics and Physics of Solids* 35.2 (1987), pp. 213–226. DOI: 10.1016/0022-5096(87)90036-6.

[261] R. L. Weaver. “Anderson localization of ultrasound”. In: *Wave Motion* 12.2 (1990), pp. 129–142. DOI: 10.1016/0165-2125(90)90034-2.

[262] J. Weber. “Recherches concernant les contraintes intergranulaires dans les milieux pulvérulents”. In: *Bulletin de liaison des Ponts et Chaussées* 20 (1966), pp. 1–20.

[263] C. Wellmann and P. Wriggers. “A two-scale model of granular materials”. In: *Computer Methods in Applied Mechanics and Engineering* 205 (2012), pp. 46–58. DOI: 10.1016/j.cma.2010.12.023.

[264] C. M. Wensrich et al. “Measurement and analysis of the stress distribution during die compaction using neutron diffraction”. In: *Granular Matter* 14.6 (2012), pp. 671–680. DOI: 10.1007/s10035-012-0366-8.

[265] D. S. Wiersma et al. “Localization of light in a disordered medium”. In: *Nature* 390.6661 (1997), p. 671. DOI: 10.1038/37757.

[266] L. G. William, R. Triolo, and A. L. Tampere. “Analytical structure function of a polydisperse Percus-Yevick fluid with Schulz (gamma) distributed diameters”. In: *Physical Review A* 33.3 (1986), pp. 2197–2200. DOI: 10.1103/PhysRevA.33.2197.

[267] *World bank indicator*. https://data.worldbank.org/indicator/IS.RRS.TOTL.KM. Accessed: 07/06/2018.

[268] J. Zhang et al. “Statistical properties of a 2D granular material subjected to cyclic shear”. In: *Granular Matter* 12.2 (2010), pp. 159–172. DOI: 10.1007/s10035-010-0170-2.

[269] Y. Zhang, T. J. R. Hughes, and C. L. Bajaj. “An automated 3D mesh generation method for domains with multiple materials”. In: *Computer Methods in Applied Mechanics and Engineering* 199.5-8 (2010), pp. 405–415. DOI: 10.1016/j.cma.2009.06.007.

[270] Y. Zhang, X. Liang, and G. Xu. “A robust 2-refinement algorithm in octree and rhombic dodecahedral tree based all-hexahedral mesh generation”. In: *Proceedings of the 21st International Meshing Roundtable, IMR 2012* 256 (2013), pp. 155–172. DOI: 10.1007/978-3-642-33573-0-10.

[271] T. I. Zohdi. “Computational modeling and design of new random microheterogeneous materials”. In: *CISM Course Notes* (2002).